

REPORT DOCUMENTATION PAGE			Form Approved OMB No. 0704-0188	
Public reporting burden for this collection of information is estimated to average 1 hour per response, including the time for reviewing instructions, searching existing data sources, gathering and maintaining the data needed, and completing and reviewing the collection of information. Send comments regarding this burden estimate or any other aspect of this collection of information, including suggestions for reducing this burden to Washington Headquarters Services, Directorate for Information Operations and Reports, 1215 Jefferson Davis Highway, Suite 1204, Arlington, VA 22202-4302, and to the Office of Management and Budget, Paperwork Reduction Project (0704-0188), Washington, DC 20503.				
1. AGENCY USE ONLY (Leave blank)		2. REPORT DATE August 2000		3. REPORT TYPE AND DATES COVERED Final Report
4. TITLE AND SUBTITLE Broadly Tunable, Narrow Line Color Center Laser Oscillation For Molecular Gas Spectroscopy And Excitation			5. FUNDING NUMBERS F61775-99-WE	
6. AUTHOR(S) Prof Tasoltan Tazretovich Basiev				
7. PERFORMING ORGANIZATION NAME(S) AND ADDRESS(ES) Laser Materials and Technology Research Center of the General Physics Institute 38 Vavilov St Moscow 117942 Russia			8. PERFORMING ORGANIZATION REPORT NUMBER N/A	
9. SPONSORING/MONITORING AGENCY NAME(S) AND ADDRESS(ES) EOARD PSC 802 BOX 14 FPO 09499-0200			10. SPONSORING/MONITORING AGENCY REPORT NUMBER SPC 99-4019	
11. SUPPLEMENTARY NOTES Four .PDF files. <i>Original charts in color</i>				
12a. DISTRIBUTION/AVAILABILITY STATEMENT Approved for public release; distribution is unlimited.			12b. DISTRIBUTION CODE A	
13. ABSTRACT (Maximum 200 words) This report results from a contract tasking Laser Materials and Technology Research Center of the General Physics Institute as follows: The contractor will investigate color center laser crystals operating at room temperature in the 1 - 1.5 micron spectral range with nanosecond neodymium laser pumping, and especially addressing narrow line operation and power amplification, including study of different optical laser schemes and optimization of spectral width, stability, tunability, and output energy for application to molecular gas spectroscopy and excitation.				
14. SUBJECT TERMS EOARD, Solid state lasers, lasers and laser engineering, Color center lasers, Tunable lasers			15. NUMBER OF PAGES	
			16. PRICE CODE N/A	
17. SECURITY CLASSIFICATION OF REPORT UNCLASSIFIED	18. SECURITY CLASSIFICATION OF THIS PAGE UNCLASSIFIED	19. SECURITY CLASSIFICATION OF ABSTRACT UNCLASSIFIED	20. LIMITATION OF ABSTRACT UL	

NSN 7540-01-280-5500

Standard Form 298 (Rev. 2-89)
Prescribed by ANSI Std. Z39-18
298-102

DTIC QUALITY INSPECTED 4

**LASER MATERIALS AND TECHNOLOGY RESEARCH CENTER
OF GENERAL PHYSICS INSTITUTE**

**Final report
on the project**

**Broadly Tunable Narrow Line Color Center Laser
Oscillation for Molecular Gas Spectroscopy and
Excitation**

(№ F61775-99-WE019)

(SPC-99-4019)

**Moscow
August 2000**

20000907 100

**AQF00-11-3791
DTIC QUALITY INSPECTED 4**

Content

1. *Introduction.*
 - 1.1. *Color center laser.*
 - 1.2. *Spectral selectivity of tunable laser cavity.*
 - 1.2.1. *Cavity with prism.*
 - 1.2.2. *Cavity with diffraction grating.*

2. *Theoretical and Experimental Study of the Narrowband Color Center Laser with Grazing Incidence Grating Cavity.*
 - 2.1. *Introduction.*
 - 2.2. *The Mathematical Model of Narrowband Pulse Laser with Littman-Metcalf Cavity.*
 - 2.2.1. *Mathematical model of pulsed GIG laser.*
 - 2.2.2. *Propagation of the radiation through the cavity.*
 - 2.2.3. *Behavior of the beam parameters at the laser active region pass.*
 - 2.2.4. *Discretization of the laser radiation.*
 - 2.2.5. *Interaction of the radiation with the active medium.*
 - 2.3. *Numerical modeling of color center laser with GIG cavity.*
 - 2.4. *Color center GIG laser with intracavity beam expander.*
 - 2.4.1. *Introduction.*
 - 2.4.2. *Optimization of the color center GIG laser with intracavity beam expander.*

3. *Experimental realization of color center GIG laser.*
 - 3.1. *Intracavity beam expander.*
 - 3.2. *Gratings and mirrors.*
 - 3.3. *Crystal preparation.*
 - 3.4. *Pump laser.*
 - 3.5. *The Measurements of the linewidth of the laser oscillation.*
 - 3.6. *Experimental results.*

- 3.7. *Experimental realization of color center GIG laser with combined diffraction grating.*

- 4. *Mathematical modeling of color center laser amplifier.*
 - 4.1. *Interaction of the radiation with the active medium.*
 - 4.2. *Mathematical model of the color center laser amplifier.*
 - 4.3. *The amplifier cell simulation results.*

- 5. *Development of LiF:F_2^- amplifier for tunable laser.*
 - 5.1. *The single-pass amplification in LiF:F_2^- color center crystal.*
 - 5.2. *Two-pass amplification in LiF:F_2^- color center crystal.*

1. Introduction

1.1. Color center laser.

Great progress has been made during last decade on solid state color center laser development. Laser active F_2^- and F_3^- color centers are known to be aggregate quasi-molecular vacancies capturing 3 or 4 electrons. LiF crystal with F_2^- color centers (CC) has become the most popular active element for CC lasers. Luminescence spectrum of F_2^- color centers in LiF crystal at room temperature covers a very wide spectral range from 0.95 to 1.35 μm with maximum at $\lambda=1.135 \mu\text{m}$. Its absorption band extends from 0.8 to 1.13 μm with maximum at $\lambda=0.96 \mu\text{m}$ and overlaps well with radiation of well developed Nd laser sources. These CC have quantum yield close to unity and high value of absorption and luminescence cross sections $\sim 8 \times 10^{-17} \text{ cm}^2$. The radiative lifetime of F_2^- CC in LiF crystals at room temperature is 55 ns. LiF crystal has high thermo and physical properties, good moisture resistance (see Table 1.1). The F_2^- CC possess high thermo and photo stability which allows them to operate with high energy and pump densities up to 100 J and 2 J/cm².

Table 1.1. Properties of LiF crystals with F_2^- color centers

Physical	
Thermal stability	> 10 years at 300K temperature
Thermal conductivity coefficient	$\alpha=14 \text{ Wm}^{-1}\text{K}^{-1}$
Moisture resistant	High
Mechanically durable	long
Optical	
Emission cross section (σ)	$6.8 \times 10^{-17} \text{ cm}^2$
Fluorescent lifetime (τ)	55 ns
Bandwidth ($\Delta\nu$)	1500 cm^{-1}
Contrast ($\beta=K_{\alpha}/K_{\text{loss}}$)	15-30
High optical damage threshold	5-6 J/cm ² (for nanosecond pulses)

1.2. Spectral selectivity of tunable laser cavity.

The development of different cavities of tunable laser has been an important task of laser physics for more than last 30 years. At the beginning the main activity was concentrated on developing cavities for dye lasers. There are two main parameters which characterize dispersive cavity: spectral selectivity and losses. By introducing the dispersive element inside the cavity the angular dispersion D_c as

$$D_c = d\phi/d\nu \quad (1.1)$$

introduces the dispersive losses that are the losses which depend on the oscillating frequency ν . If a single mode oscillation with Gaussian beam distribution is considered it is possible to estimate the maximum spectral selectivity of the cavity (low aperture case) as:

$$d\nu = \lambda / D_c d \quad (1.2)$$

Here d is the characteristic intracavity aperture and it has parabolic dependence of the losses on frequency as:

$$\delta\nu_c = \left(\gamma_0 / \ln 2 \right)^{1/2} \lambda / D_c d \quad (1.3)$$

and the limited spectral width of the cavity is

$$d\nu = 2 \lambda / D_c d \quad (1.4)$$

In the practical lasers the role of intracavity aperture can play not only a real intracavity aperture but also the pumped region of the optical medium. The most important parameter of disperse cavity is the angular selectivity D_c , which will be considered below for different cavities.

It is necessary to note that there is a physical limitation on the linewidth of the oscillating radiation due to limited duration of oscillation. For pulsed laser the value of the linewidth and pulse duration are connected by the principle of uncertainty:

$$\tau \cdot \delta\nu = 1 \quad (1.5)$$

This means that for $\tau = 10$ ns laser pulse the linewidth $\delta\nu$ can not be less than 100 MHz. Special laser cavity design can only approach to this value. For longer pulses this limit is reduced appropriately.

Below we will consider various elements of the dispersive cavities and summarize data about different cavity designs. The main element in such cavity is dispersive element. It can be any optical element with spectral selectivity like prism, diffraction grating, Fabry Perrot etalon, accousto optic filter or something else.

1.2.1. Cavity with prism

Dispersive cavities with prisms is the most common type of cavities used for tunable lasers. The angular dispersion of the prism D_c depends on the incident and refractive beam angles (α_1 and α_2) as (Fig. 1.1, b):

$$D_c = d\alpha_1/d\lambda + d\alpha_2/d\lambda \quad (1.6)$$

where

$$d\alpha_1/d\lambda = (dn/d\lambda) \sin A / \cos \alpha_2 \cos \beta_1 \quad (1.7)$$

is angular dispersion for the incident beam and

$$d\alpha_2/d\lambda = (dn/d\lambda) \sin A / \cos \alpha_1 \cos \beta_2 \quad (1.8)$$

is angular dispersion for the refracted beam. Here A is the prism angle. When the prism is installed so that the refraction angle is minimal ($\alpha_1 = \alpha_2 = \alpha$ and $\beta_1 = \beta_2 = \beta$) equation (1.4) can be transformed to the following:

$$D_c = 4n^{-1} (dn/d\lambda) \tan \alpha \quad (1.9)$$

And the prism is a Brewster prism that is at both prism planes the beam passes at Brewster angle ($\tan \alpha = n$), in this case the equation can be simplified as

$$D_c = 4 (dn/d\lambda) \quad (1.10)$$

here $dn/d\lambda$ is dispersion of the refraction index of prism material. But usually prisms have rather low dispersion in the IR region. Dispersion of the refraction index of some materials at $\lambda = 1 \mu\text{m}$ is presented in Table 1.2.

The qualitative explanation of dispersion cavity with one prism is shown in Fig. 1.1,a. The spectral band of the cavity $\gamma(\lambda_c)$ can be determined as dependence of cavity losses due to disperse element. It is determined by D_c and can be approximated by parabolic equation as

$$\gamma(\lambda) = \gamma_0 \left\{ 1 + 4 \left[\frac{(\lambda - \lambda_c)}{\delta\lambda_c} \right]^2 \right\} \quad (1.11)$$

here γ_0 is non-selective losses, λ_c is the central wavelength of the cavity and the spectral selectivity of the cavity $\delta\lambda_c$ is determined as $\delta\lambda_c = \gamma_0^{1/2} \Theta_c D_c^{-1}$, where Θ_c is the angular divergence of the cavity. For typical values of the divergence $\Theta_c \sim 2$ mRad and non-selective losses $\gamma_0 \sim 0.4$, the spectral selectivity of the glass prism can be estimated as $\delta\lambda_c \sim 0.3$ nm. The use

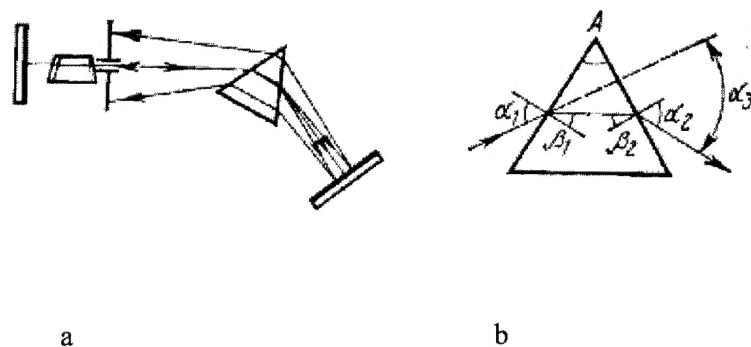


Fig. 1.1. Optical scheme which demonstrates the principle of operation of the tunable laser cavity with dispersion prism inside.

Table 1.2. Dispersion of some optical materials at 1 μm wavelength.

Material	$Dn/d\lambda \cdot 10^5 (\text{nm}^{-1})$
Glass K-8	1.3
Crystal Quartz	1.4
Fused Quartz	1.3
Flint TF-2	2.3
Flint TF-10	3.3
Hard Flint STF-1	5.2
SrTiO_3	8.8
TiO_2	12.5

of other optical materials can reduce the spectral selectivity of the cavity up to 5-10 times but they can exhibit higher optical losses.

To conclude it is possible to outline that the advantages of prism resonators is their simplicity, cheap elements and low losses while the main drawback is their low spectral selectivity.

1.2.2. Cavity with diffraction grating

Narrow linewidth tunable lasers usually utilize diffraction gratings as dispersive elements in their cavities. Diffraction gratings exhibit unique quality to have high spectral selectivity, large free spectral region between different maxima, simple linear tuning with sine mechanism and the possibility to control absolute wavelength with high accuracy. As a result tunable laser with diffraction grating can provide wide tuning range with narrow linewidth ($\Delta\nu < 0.01 \text{ nm}$).

The incidence (φ) and diffraction angles (ψ), radiation wavelength (λ) and grating spacing (t) (see Fig. 1.2) depends are connected by the following equation:

$$t(\sin \alpha + \sin \beta) = m\lambda \quad (1.13)$$

here m - is diffraction order (integer number). For autocollimation regime when the incidence and diffracted angles are similar ($\alpha = \beta$) equation (1.2) becomes as:

$$2t \sin \alpha = m\lambda \quad (1.14)$$

The angular dispersion of the grating equals as

$$D = \frac{d\beta}{d\lambda} = \frac{m}{\lambda \cos \beta} = \frac{\sin \alpha + \sin \beta}{\lambda \cos \beta} \quad (1.15)$$

For autocollimation scheme dispersion equals as:

$$D = \frac{2tg\alpha}{\lambda} \quad (1.16)$$

The dispersion of the grating is increased with reducing its spacing t . Meanwhile the spacing (t) is limited and cannot be smaller than $\lambda/2$, for smaller spacing the diffraction becomes impossible. For diffraction grating the important values of spacing are

$$\lambda/2 \leq t \leq \lambda \quad \text{or} \quad t \leq \lambda \leq 2t \quad (1.17)$$

It corresponds to the situation when there is only two reflected beams: the first and zero diffraction orders. For autocollimation scheme this condition becomes as follows:

$$\lambda/2 \leq t \leq 3\lambda/2 \quad \text{or} \quad 2t/3 \leq \lambda \leq 2t \quad (1.18)$$

The theoretical angular resolution of diffraction grating $\delta\Theta$ equals

$$\delta\Theta = \frac{\lambda}{zd \cos \beta} \quad (1.19)$$

Here z is the number of the grating lines in the illuminated area. For the most part of the tunable lasers $\delta\Theta$ is much less than the divergence of the incident radiation and doesn't determine the oscillating linewidth. The exception is the cavities with strong telescopes in front of the grating.

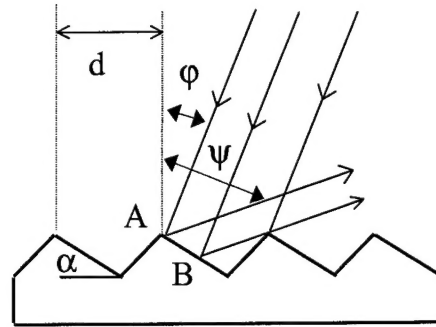


Fig. 1.2. Diffraction at the grating grooves.

The maximal theoretical resolution of the cavity equals to the maximal difference in the optical paths of interference beams and is determined by the following equation:

$$R = \frac{\delta\lambda}{\lambda} = Nt \quad (1.20)$$

here N is the total number of the grating grooves. For example for $1 \mu\text{m}$, and spacing $t=0.83 \mu\text{m}$ and diffraction width 40 mm the maximal spectral resolution for one pass diffraction equals to $\delta\nu \approx 0.2 \text{ cm}^{-1}$. It is necessary to note that in the cavity during the development of the oscillation the multiple passes can sufficiently reduce the oscillating linewidth till single mode oscillation.

The simplest tunable laser cavity with diffraction grating is shown in Fig.1.3. It includes the mirror (M) and diffraction grating (G) which work in the autocollimation scheme (incident and diffracted angles are the same, $\varphi=\psi$). In this cavity diffracted radiation in the first order is used for feedback. The laser output is through the zero order of diffraction or mirror (M).

The autocollimation condition is easily obtained from equation (1.1) for $\varphi=\psi$ as:

$$2t \sin(\varphi) = m\lambda \quad (1.21)$$

From equation (1.21) follows that the oscillation wavelength depends on the incident angle as a *sin* law. Such dependence can be easily realized by *sin* mechanism. This mechanism can realize the linear dependence of the oscillating wavelength and can easily control it. Lets consider in more details the disperse properties of this cavity. To find the angular dispersion we need to differentiate equation (1.21) with respect to λ at constant φ :

$$\frac{d\varphi}{d\lambda} = \frac{2tg(\varphi)}{\lambda} \quad (1.22)$$

From equation (1.22) follows that the angular dispersion is determined only by autocollimation angle (φ) and is increased with rotating the grating to the grazing incidence angle. So in order to

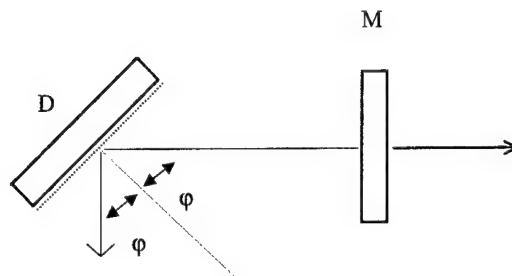


Fig. 1.3. Disperse laser cavity with diffraction grating.

realize the narrow line oscillation it is necessary to select the grating with the maximal autocollimation angle for the certain spectral region. Fig. 1.4 presents the autocollimation angles and the wavelength dependence of angular dispersion for gratings with 1200 lines per mm (1), 1500 (2) and 1660 (3). From Fig. 1.4 follows that to tune the wavelength from 1.1 to 1.2 μm with these gratings (1)-(3) it is necessary to change the incident angle from 41 to 46 degrees, from 55 to 64 and from 66 to 85 correspondingly. Thus, the use of the grating with smaller spacing (1500 and 1660) results in the necessity to increase the change of the incidence angle with tuning the wavelength. Fig. 1.5,b presents the angular dependence of the same gratings. As one can see the use of 1660 and 1500 gratings instead of 1200 results in the strong increase of the angular dispersion, especially at about 1.2 μm region. But it is obvious that the further reduction can result in the limitation of the tuning range for longer wavelengths. To estimate the angular dispersion of the one pass of the cavity one can use the following equation:

$$\delta\lambda = \left(\frac{d\varphi}{d\lambda} \right)^{-1} \delta\varphi = \frac{\lambda(\delta\varphi)}{2tg\varphi} \quad (1.23)$$

To estimate for $(\delta\varphi)$ it is possible to take the typical divergence of the laser beam as 1 mRad. In this case for the central wavelength of LiF:F₂⁻ CC laser ($\lambda=1.14 \mu\text{m}$) one can get $\delta\nu \approx 6 \text{ cm}^{-1}$, $\delta\nu \approx 3 \text{ cm}^{-1}$, and $\delta\nu \approx 2 \text{ cm}^{-1}$ for 1200, 1500 and 1660 l/mm. Thus the use of the grating with 30% larger number of grooves per mm results in the spectral selectivity improvements at least for three times. (It is necessary to note that these values are only for single pass through the cavity. In real cavity the number of passes are much larger.

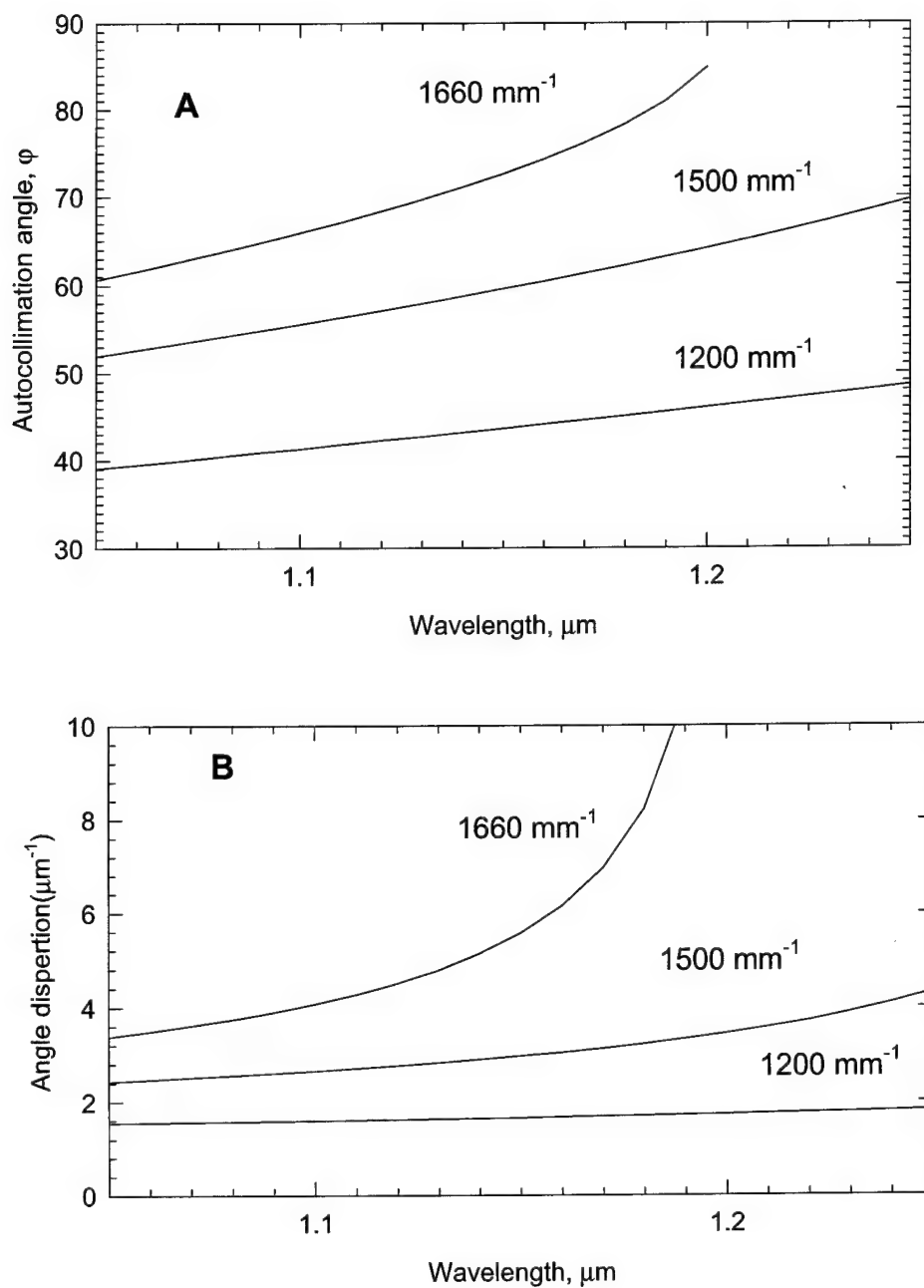


Fig. 1.4. The dependence of the autocollimation angle and angular dispersion for three gratings 1200, 1500 and 1660 lines per mm.

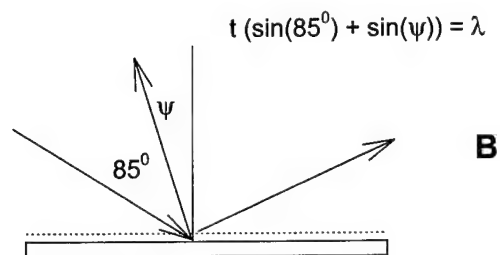
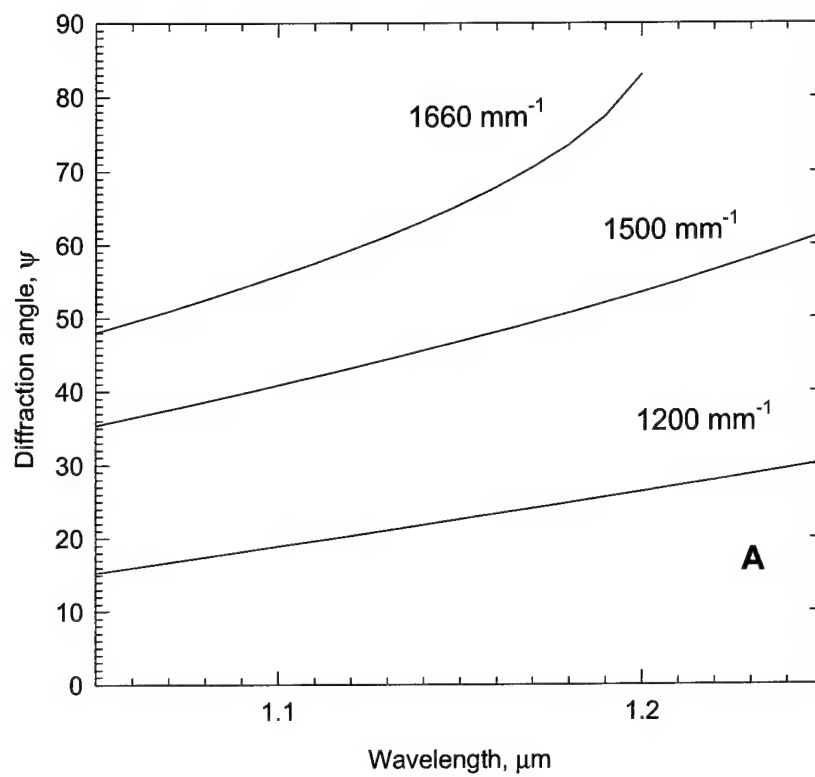


Fig. 1.5. The angular dependence for three gratings 1200, 1500 and 1660 lines per mm.

Meanwhile it is not easy to select or order the grating with high autocollimation angle in the required spectral region. At the same time the slight change of the incidence angle can result in the strong change of the angular dispersion (Fig. 1.5b). That's why wide practical use has been found grazing incidence schemes (Fig. 1.4). Lets consider this scheme in more details. The cavity consists of the two mirrors M1 and M2 and diffraction grating G1. The correlation between the incident and diffracted angles is described by equation (1.1). One cavity round trip includes diffraction at the grating two times. The first time when the radiation passes from mirror M1 to the grating G1. Angular dispersion in this case is described as following:

$$\frac{d\varphi}{d\lambda} = \frac{1}{\lambda} \frac{\sin(\varphi) + \sin(\psi)}{\cos(\varphi)} \quad (1.24)$$

The second diffraction occurs when beam goes from mirror M2 to grating G1:

$$\frac{d\psi}{d\lambda} = \frac{1}{\lambda} \frac{\sin(\varphi) + \sin(\psi)}{\cos(\psi)} \quad (1.25)$$

The zero order of diffraction is the cavity output coupling. The tuning of the wavelength is usually made by rotation of the mirror M2. In this case the grazing incidence angle is not changed. Total dispersion for one round trip is obtained by summation of equations (1.24) and (1.25). In the grazing incidence ($\varphi, \psi \sim 90^\circ$) the dispersion will be determined by the first term (1.24).

$$\frac{d\psi}{d\lambda} = \frac{1}{\lambda} \frac{(1 + \sin(\varphi))}{(\pi/2 - \psi)} \quad (1.26)$$

As follows from equations (1.24)-(1.26) to obtain maximal dispersion in the scheme with grazing incidence it is necessary to work with larger ψ angles. In the optimal case when ψ is close to the grazing incidence the dispersion will be determined as:

$$\frac{d\psi}{d\lambda} = \frac{1}{\lambda} \frac{4}{(\pi/2 - \psi)} \quad (1.27)$$

Twice bigger value in the ratio in (1.27) in comparison with autocollimation scheme (1.16) is due to the fact that in the last case the radiation is diffracted only once during the round trip while for grazing incidence - twice.

The dependencies of diffraction angles at 85° incidence angle are presented in Fig. 1.6. The angular dispersion for all $\psi < 90^\circ$ will be determined by the term (1.24) and that's why for all gratings it will be similar. Only for 1660 grating at the long wavelength region with $\psi \sim \varphi \sim 90^\circ$ angular dispersion will be increased twice.

Another reason to use large diffraction angle φ is the shadowing of the grooves. This phenomena occurs by shadowing the grooves one by another for the beam reflected by mirror

M2. From Fig. 1.2 follows that the input into the radiation at φ angle is by the AB region. As easily can be obtained the intensity of the diffracted radiation is proportional to:

$$k = \left(\frac{\cos(\varphi) \cos(\psi - \alpha)}{\cos(\psi) \cos(\varphi - \alpha)} \right)^2 \quad (1.28)$$

The shadowing effect will be diminished for $\alpha=0$ grating without profile and for $\varphi=\psi$. The last equation cannot be practically realized, but it is possible to work at close angles. This results in the reducing of this shadowing effect, while it is necessary to note the strong dependence of the angle on the oscillating wavelength. That's why it is impossible to remove this effect completely.

2. Theoretical and Experimental Study of the Narrowband Color Center Laser with Grazing Incidence Grating Cavity

2.1. Introduction

The dispersive laser cavity with the diffraction grating in grazing incidence configuration was proposed by Littman and Metcalf [i, ii]. Initially Littman-Metcalf or GIG scheme was proposed as cavity for narrowband pulse dye lasers. At the present moment the different modifications of GIG cavities are in widely use in dye lasers, Ti:sapphire lasers, diode lasers and other types of tunable lasers techniques. The main advantages of Littman-Metcalf cavity are high selectivity, very simple construction and ease of control. Therefore the use of GIG cavity for realization of narrowband pulse color center laser looks enough prospective.

The typical scheme of GIG laser is shown in Fig. 2.1. The cavity is formed by a back mirror m , a tuning mirror M and a diffraction grating G . The laser wavelength is determined by the well-known formula for diffraction grating:

$$\lambda = \Lambda(\sin \theta + \sin \varphi), \quad (2.1.)$$

where λ is the laser wavelength; Λ is the grating period; θ is the angle of incidence of the radiation at the grating (the angle between the grating G and the back mirror m); φ is the angle of diffraction (the angle between the grating G and the tuning mirror M). The laser frequency scanning is carried out by the tuning mirror M rotation. The laser radiation outputs the cavity through the zero grating diffraction order or through the semitransparent mirror m .

From eq. (2.1) is easy to obtain the expression for the angular dispersion of diffraction grating D :

$$D = d\psi/d\lambda = 1/(\Lambda \cos \psi), \quad (2.2.)$$

where ψ – is the angle of diffraction.

At the GIG cavity roundtrip, the radiation twice diffracts on the grating. At the first pass, the diffraction angle is equal φ , at the second – θ . Thus, we can approximate the total roundtrip GIG cavity dispersion by the

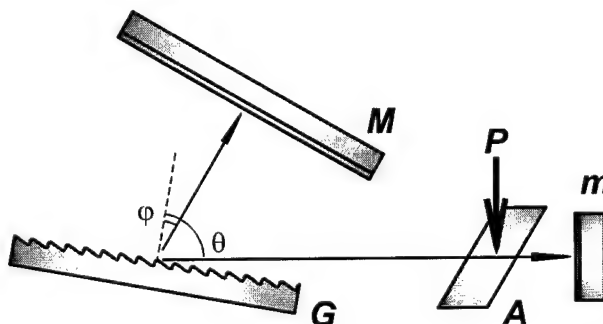


Fig. 2.1

expression:

$$D^{(GIG)} \approx \frac{1}{\Lambda} \left(\frac{1}{\cos \varphi} + \frac{1}{\cos \theta} \right). \quad (2.3.)$$

If the angle θ is tend to the right angle limit the $\cos \theta \rightarrow 0$ and, according to eq. (2.3), the dispersion of GIG cavity significantly increases. The high dispersion of the diffraction grating, in the grazing incidence mounting, allows to reach the narrowband and even the single-frequency laser operation without using additional intra-cavity selectors (etalons) and beam expanders. Thus, the main advantages of the lasers with GIG cavity are the extremely simple design and the ease of control.

2.2. The Mathematical Model of Narrowband Pulse Laser with Littman-Metcalf Cavity

2.2.1. Brief description of the mathematical model of pulsed GIG laser

During the pump pulse development, in the laser cavity takes place the spontaneous emission and amplification of the radiation in a wide spectral range. If we will consider the radiation as a set of beams with various frequencies, intensities and geometrical parameters, than the process of origination of the narrowband laser pulse from broadband spontaneous background can be described on a basis of the following model:

- *Due to the diffraction on the grating, the beams with different frequencies gets different angular deviations from the cavity axis.*
- *At the cavity trip the angular dispersion of the radiation turns to spatial dispersion, thus, the beams with frequency detuning push away from the cavity and their amplification in the active region falls*
- *The divergence of the beams causes their overlap and decreases the cavity selectivity.*
- *Simultaneously in the cavity takes place the spontaneous origination of the new beams with various frequencies.*

Because the abovementioned processes in the cavity go on continuously, the direct numerical modeling of the laser is enough difficult. Therefore, the second part of the model was the scheme of discretization. It was built on the basis of the following assumptions:

- *The spontaneous emission and the amplification of the radiation in the laser active region takes place not continuously, but in discrete moments of a time $t = n\tau$, $n = 0, 1, 2, \dots$*

- The spontaneous emission of the active region is distributed like a discrete set of beams.
- The frequencies of the new beams are occupying the finite spectral region.

We can determine the distribution of the radiation in the cavity in a time moment $t = n\tau$ inductively if we express the parameters of each beam at any count of a time through the beams parameters at the previous count. Therefore, the mathematical model should include:

- The relations between the beams parameters before and after the cavity roundtrip.
- The relations between the beams parameters before and after they pass through the laser active region.
- The initial parameters of each beam.

2.2.2. Propagation of the radiation through the cavity

The scheme of the GIG cavity is shown in Fig. 2.2. The cavity includes the mirrors m and M and the grating G . Let designate the grating period as Λ , the angle between grating G and mirror m (the incidence angle) as θ , the angle between grating G and mirror M as ϕ . The diffraction angle ϕ determine the laser wavelength λ_0 : $\lambda_0 = \Lambda(\sin\theta + \sin\phi)$. On the figure are also shown the coordinates axis. Let the cavity propagate the beam with the following parameters:

ν - frequency

u - power

$\omega_{y,z}$ - beam transverse sizes

α - angular deviation from the cavity axis

A - spatial deviation from the cavity axis

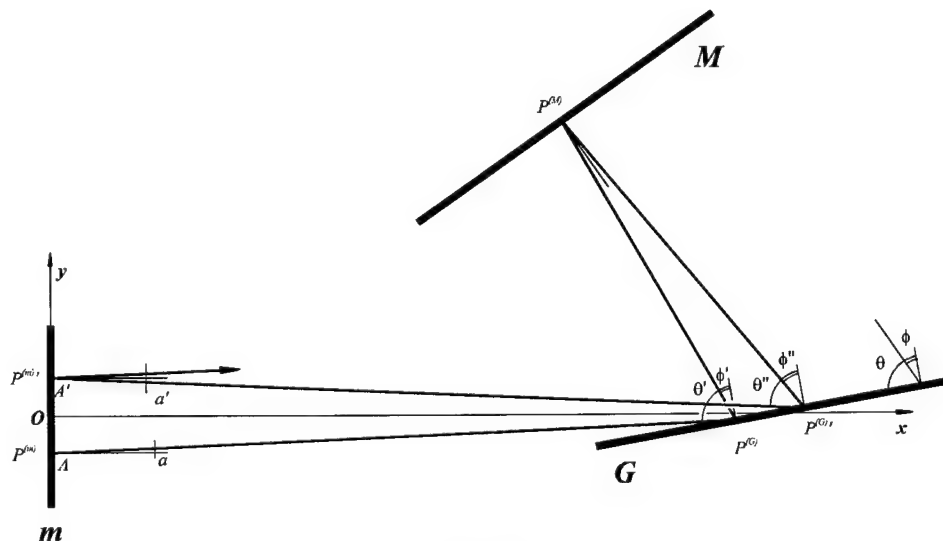


Fig. 2.2

Where the geometrical parameters of the beam (ω_y, ω_z, a, A) are measured at the mirror m plane. On the figure is also shown the path of one of the beams. $P^{(m)}, P'^{(m)}, P^{(M)}, P^{(G)}, P'^{(G)}$ are the cross-points of the path with the cavity elements, a, A are the angular and the spatial deviations of the beam from the cavity axis before and a', A' – after cavity roundtrip, φ', θ' and θ'', φ'' are the incidence and the diffraction angles at the first and the second grating pass respectively. We introduce also the following designations:

$$\begin{aligned} s &= \sin \varphi & \bar{s} &= \sin \theta & \ell_0 &= \lambda_0 / \Lambda \\ c &= \cos \varphi & \bar{c} &= \cos \theta & \ell &= \lambda / \Lambda \end{aligned} \quad (2.4.)$$

where λ is the wavelength of the beam.

Let's consider the behavior of the geometrical beam parameters at the cavity roundtrip. From the formula for diffraction grating

$$\lambda = \Lambda(\sin \theta + \sin \varphi) \quad (2.5.)$$

and obvious relations

$$\begin{aligned} \theta' &= a + \theta \\ \theta'' &= a' + \theta \\ \varphi' + \varphi'' &= 2\varphi \end{aligned} \quad (2.6.)$$

we obtain the expression connecting the angular deviations of the beam from the cavity axis before and after the roundtrip:

$$\arcsin(\ell - \sin(a' + \theta)) + \arcsin(\ell - \sin(a + \theta)) = 2\varphi \quad (2.7.)$$

The expression, connecting spatial deviations of the beam A and A' is rather unwieldy and it is not presented here. At the computer modeling the coordinates of the beam cross-points with cavity elements are calculated one after the other.

The diameter ω of the free propagating beam is changed because to its geometrical and natural divergence.

$$\omega(x) = \omega_0 + \alpha x \quad (2.8.)$$

where α is an angle of divergence and x is a passed length. If the reflection on the mirrors not affects the beam transverse size, the diffraction grating could changes it essentially. It is easy to show that the ratio of diffracted and incident beams sizes is equal to the ratio of the diffraction and the incident angles cosines.

$$\frac{\omega^{(d)}}{\omega^{(i)}} = \frac{\cos \varphi}{\cos \theta} \quad (2.9.)$$

The angle of incidence θ in the GIG cavity is close to the right angle ($\cos \theta \rightarrow 0$), therefore at the first grating pass (point $P^{(G)}$ in Fig. 2.2) takes place a significant beam size expansion and at the second (point $P'^{(G)}$) its compression. Thus, the total cavity-trip beam size variation due to the grating diffraction is the following:

$$K = \frac{\cos \varphi' \cos \theta''}{\cos \theta' \cos \varphi''} \quad (2.10.)$$

The behavior of the coefficient K , as a function of the angular beam deviation a and its frequency, is shown in Fig. 2.3. As it is obvious from the picture, the system of grating G and mirror M can noticeably change the beam size even for a small angle deviations and a frequency detuning.

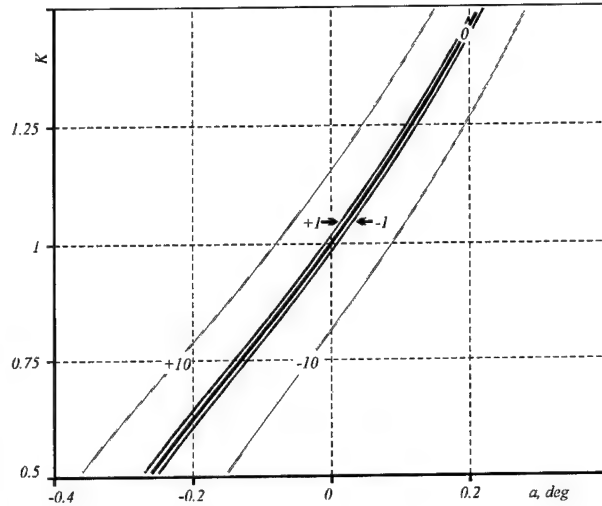


Fig. 2.3 The digits above the curves are frequency detuning of radiation from the cavity central frequency (in GGz).

2.2.3. Behavior of the beam parameters at the laser active region pass

Let suppose that the laser active medium is transparent for the laser radiation. The pump radiation pulse forms in the active medium an amplifying region. Let the intensity of the pump beam has the Gaussian transverse distribution and the length of the active region is much less than the cavity length. This assumptions allows us to consider the active region as a thin amplifying Gaussian aperture and characterize its transmission by the expression

$$t(y, z) = 1 + k \exp\left(-\frac{y^2 + z^2}{\omega^{(t)2}}\right) \quad (2.11.)$$

where k is the factor of amplification [1], and $\omega^{(t)}$ is the transverse size of the active region. Let the distribution of laser beam intensity is also Gaussian:

1 Here the amplification factor k we determine by expression $k = (I^{(out)} - I^{(in)}) / I^{(in)}$, where $I^{(in)}$ is input and $I^{(out)}$ is output signal intensities

$$u(y, z) = \frac{u_0}{\pi \omega_y \omega_z} \exp \left[-\frac{(y-A)^2}{\omega_y^2} - \frac{z^2}{\omega_z^2} \right] \quad (2.12.)$$

where u_0 is the beam power, ω_y and ω_z are beam transverse sizes in Oy and Oz directions, A is the spatial deviation of the beam from the center of the active region (cavity axis). From eq. (2.11) and (2.12) we obtain the distribution of the intensity of the passed through the active region beam:

$$u'(y, z) = u(y, z) \chi(y, z) \quad (2.13.)$$

Let's approximate (2.13) by the Gaussian distribution. After some simple calculations we came to the expressions for the integral intensity (power) of the passed beam:

$$u'_0 = \iint \tilde{u}(y, z) dy dz = u_0 (1 + K), \quad (2.14.)$$

where

$$K = k \Omega_y \Omega_z \exp \left(-\frac{A^2}{\omega^{(t)2} + \omega_y^2} \right) \quad (2.15.)$$

$$\Omega_{y,z}^2 = \frac{I}{I + \omega_{y,z}^2 / \omega^{(t)2}}$$

and spatial deviation of the passed beam (centroid of distribution (2.13))

$$A' = \frac{\iint \tilde{u}(y, z) y dy dz}{\iint \tilde{u}(y, z) dy dz} = A \frac{1 + \Omega_y^2 K}{1 + K} \quad (2.16.)$$

Let's determine the transverse sizes of the passed beam by analogy with the Gaussian distribution. Using the expression

$$\int_{-\omega}^{+\omega} \exp \left(-\frac{t^2}{\omega^2} \right) dt = \text{erf}(1) \int_{-\infty}^{+\infty} \exp \left(-\frac{t^2}{\omega^2} \right) dt$$

we came to transcendental equations for ω'_y and ω'_z

$$\begin{cases} \int_{A'-\omega'_y}^{A'+\omega'_y} \left[\int_{-\omega'_z}^{+\omega'_z} u'(y, z) dz \right] dy = \text{erf}(1) \iint u'(y, z) dy dz \\ \int_{-\omega'_z}^{+\omega'_z} \left[\int_{A'-\omega'_y}^{A'+\omega'_y} u'(y, z) dy \right] dz = \text{erf}(1) \iint u'(y, z) dy dz \end{cases} \quad (2.17.)$$

which can be dissolved analytically.

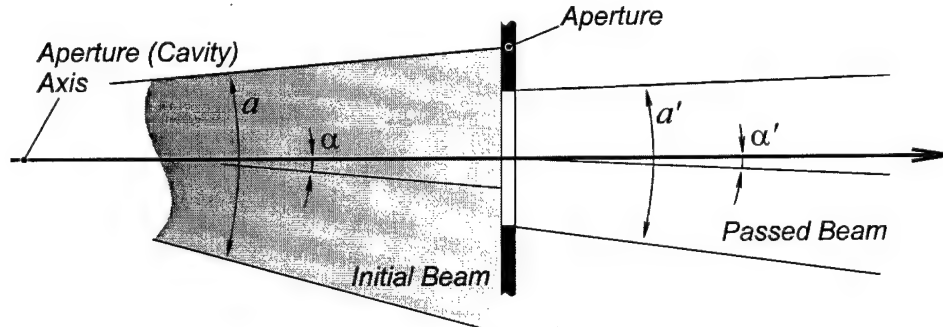


Fig. 2.4

The interaction with the active region also changes the direction of the transient beam a and its geometrical divergence $\alpha^{(G)}$ (see Fig. 2.4).

$$\operatorname{tg} a' = \operatorname{tg} a - \frac{A - A'}{\omega \cos a} \operatorname{tg} \alpha \quad (2.18.)$$

$$\operatorname{tg} \alpha'^{(G)} = \frac{\omega' \cos a'}{\omega \cos a} \operatorname{tg} \alpha^{(G)} \quad (2.19.)$$

or, in approximation of a small angles

$$a' = a - \frac{A - A'}{\omega} \alpha \quad (2.20.)$$

$$\alpha'^{(G)} = \frac{\omega'}{\omega} \alpha^{(G)} \quad (2.21.)$$

i.e. the inclination of the beam to the active region (cavity) axis a decreases on the value of its initial divergence and the geometrical divergence of the beam $\alpha^{(G)}$ decreases proportionally to its transverse size. The total beam divergence is added from its geometrical and natural divergence

$$\alpha = \alpha^{(G)} + \alpha^{(N)} \approx \alpha^{(G)} + \lambda/\omega \quad (2.22.)$$

The amplification factor k depends on the pump pulse intensity $P(t)$ and the total intensity of the laser radiation passing through the active region I .

$$I = \frac{I}{\pi \omega^{(t)2}} \sum_n \tilde{u}^{(n)} \quad (2.23.)$$

Where $\tilde{u}^{(n)}$ is the power contribution of the beam number n . The value of $\tilde{u}^{(n)}$ was defined as convolution of the transverse distribution of the beam intensity $u(y, z)$ (see. eq. (2.12.)) and the Gaussian distribution with the transverse size is equal to the size of the active region:

$$\tilde{u}^{(n)} = \iint u \exp\left(-\frac{y^2 + z^2}{\omega^{(r)2}}\right) dy dz = u_0^{(n)} \Omega_y^{(n)} \Omega_z^{(n)} \exp\left(-\frac{A^{(n)2}}{\omega^{(r)2} + \omega_y^{(n)2}}\right) \quad (2.24.)$$

The interaction of the beam with the amplifying active region is illustrated in Fig. 2.5. On the picture are shown the distribution of the active region amplification, the distribution of the initial and the passed beams intensities and the result of the gaussian approximation of the result beam. Thus the active region "attracts" the beam to the cavity axis, compensating the angular and the spatial beam drift caused by grating dispersion and its enlargement caused by divergence. These processes strongly depend on the amplification factor k .

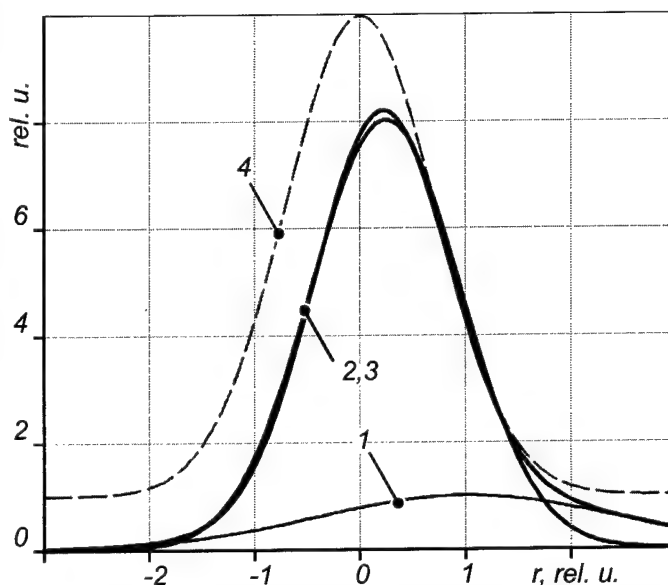


Fig.2.5 Variation of transversal intensity distribution of the beam passing through the aperture 1 – transversal intensity distribution of the initial beam (width 4, deviation +1), 2 – transversal intensity distribution of the passed beam, 3 – Gaussian approximation of the result beam distribution (width 1.4, deviation +0.24), 4 – active region amplification distribution (width 1, deviation 0.,

2.2.4. Discretization of the laser radiation

In our laser model the radiation is considered as a set of beams. As was mentioned above, the discretization of the model was carried out on the basis of the following assumptions:

- The spontaneous emission and the amplification of the radiation in the laser active region takes place in separated moments of a time $t = n\tau$, $n = 0, 1, 2, \dots$
- The spontaneous emission of the active region is distributed like a discrete set of beams.
- The frequencies of the new beams occupy the finite spectral region.

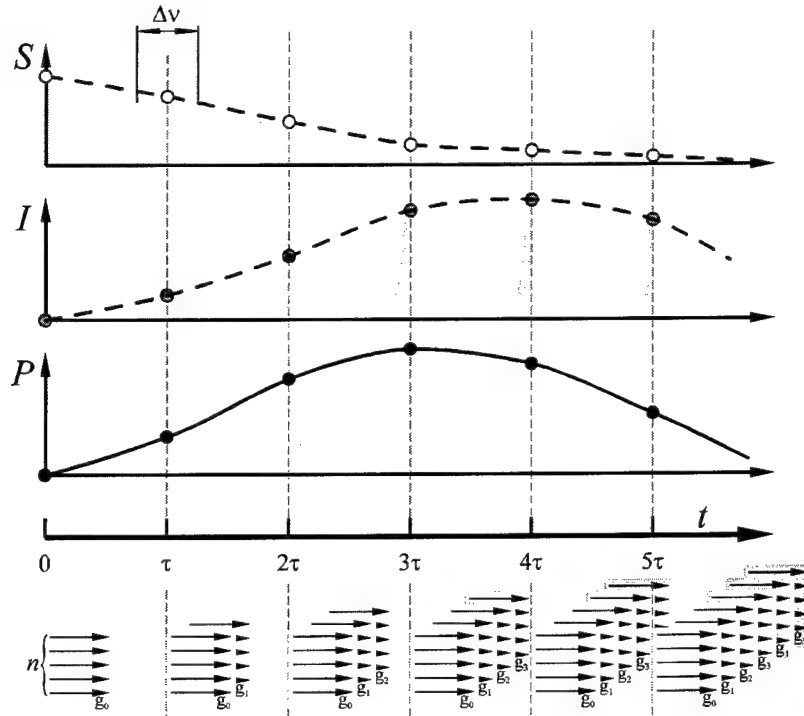


Fig. 2.6 **Descretization in GIG laser model.** t – time scale, τ – interval between discrete time counts P – pump power level, I – laser power level, S – spontaneous emission power level, Δv – width of spontaneous emission spectrum, n – number of beams in generation.

Thus, in moments of the time separated by the interval τ in the active region takes place the origination of n new beams (Fig. 2.6). The total power of the radiation S in the new generation of beams depends on the pump power level P and the laser radiation level I that already exists in the cavity.

$$\begin{aligned} S^{(N+1)} &= S[P(N\tau), I^{(N+1)}] \\ I^{(N+1)} &= \sum_{k=0}^N \sum_{i=0}^n \tilde{u}^{(k,i)} \end{aligned} \quad (2.25.)$$

Where N is the number of the generations, n is the number of the beams in the generation, $\tilde{u}^{(k,i)}$ is the power of the i -th beam in the k -th generation (it can be obtained from eq. (2.24)). Let's suppose that:

- ❖ The spontaneously emitted radiation is divided between beams in the new generation equally:

$$u_0^{(N+1,i)} = \frac{S^{(N+1)}}{n} \quad (2.26.)$$

- ❖ The frequencies of the new beams are distributed in the given spectral region equidistantly:

$$\nu^{(N+1,i)} = \nu_0 - \frac{\Delta\nu}{2} + i \frac{\Delta\nu}{n} \quad (2.27.)$$

where ν_0 is the central frequency of the laser generation.

- ❖ The initial transverse sizes of the beams are equal to the active region diameter:

$$\omega_y^{(N+1,i)} = \omega_z^{(N+1,i)} = \omega^{(i)} \quad (2.28.)$$

The spatial and the angular deviations of the beams from the cavity axis are equal to zero:

$$A^{(N+1,i)} = a^{(N+1,i)} = 0 \quad (2.29.)$$

- ❖ The divergence of the new beams is defined by geometrical parameters of the active region

$$\text{tg}(\alpha_y^{(N+1,i)}) = \text{tg}(\alpha_z^{(N+1,i)}) = \omega^{(i)} / l \quad (2.30.)$$

where l is the active region length.

The output power of the laser at the time moment $t = N\tau$ is determined by the expression:

$$I^{(out)}(N\tau) = T \sum_{k=0}^N \sum_{i=0}^n u_0^{(k,i)} \quad (2.31.)$$

where T is the zero order grating reflection or the output mirror transmission. If the intensities of each beam are determined, it is easy to determine the spectral distribution of the laser output.

$$I^{(out)}(\nu^{(i)}, N\tau) = T \sum_{k=0}^N u_0^{(k,i)} \quad (2.32.)$$

Thus, we can characterize the radiation propagated in the cavity by three parameters: the discrete time interval τ , the spectral interval $\Delta\nu$ and the number of the spectral components in the initial spectral interval n . The rigorous mathematical proof of convergence and stability of the presented scheme was not carried out. However, the test computer calculations has shown that with the increase of the discretization level (decrease of τ and increase of $\Delta\nu$ and n) the output parameters of the model (power and spectral structure of the radiation) tends to the constant rapidly. This result allows us to assume that the model was built correctly. Some tests results are shown in Fig. 2.7.

The values of parameters τ , $\Delta\nu$ and n should provide from one hand a good enough accuracy and from other hand an acceptable computation time. For 100 – 200 mm cavity length and 10 – 20 ns pump pulse duration the satisfactory test results was achieved if the value τ was equal to the cavity roundtrip time, the initial spectral width $\Delta\nu$ was 2 – 3 times greater than the limit and 40 – 50 frequency components were taken into account.

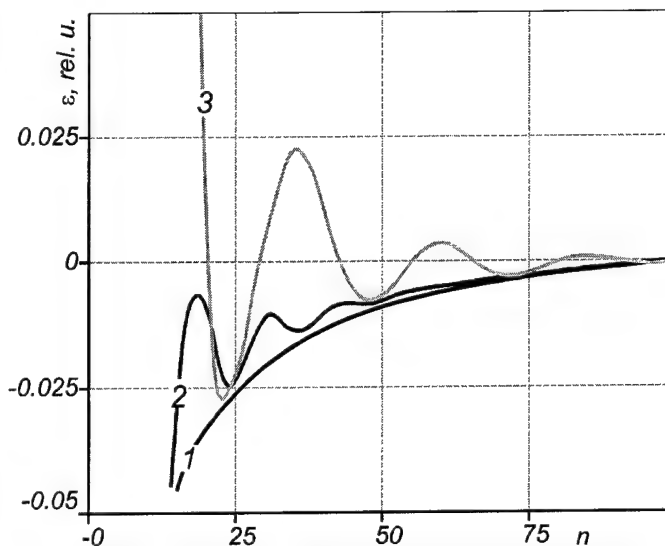


Fig. 2.7 Relative deviation $\varepsilon(n)$ of the laser-line-width from the limit as a function of number of beams in generation n

2.2.5. Interaction of the radiation with the active medium

Let the laser active medium is located near the cavity mirror m (see Fig. 2.1). The pump radiation (P) inputs into the active medium through the dichroic mirror m . The laser radiation (L) came into the active medium from the opposite side, it amplifies and returns to the cavity after the mirror reflection. Simultaneously in the active medium takes place the emission and the amplification of the spontaneous radiation (S). I.e. five types of radiation propagate the active medium: pump radiation, two laser waves in opposite directions and two amplified spontaneous emission waves (see Fig. 2.8). To describe the radiation and the active medium interaction we will use the standard techniques of kinetic equations for levels populations and transfer

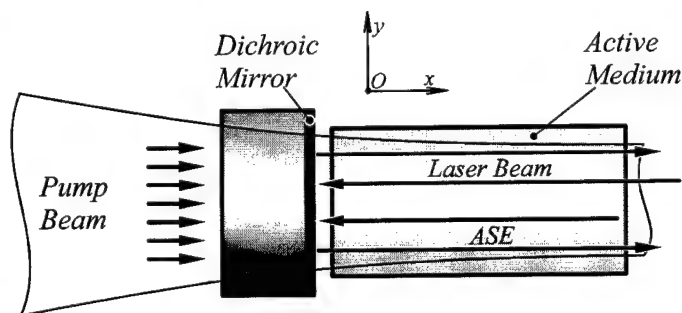


Fig.2. 8

equations for radiation. For the color centers crystal as an active medium and the considering levels of pump and laser radiation we can use the quasistationary approximation and write out equations in the following form [2]:

$$\begin{cases}
n_l = \tilde{n}(\sigma_p^{0l} i_p + \sigma_L^{0l} i_L + \sigma_S^{0l} i_S) \\
n_0 = \tilde{n} \left(\sigma_p^{l0} i_p + \sigma_L^{l0} i_L + \sigma_S^{l0} i_S + \frac{l}{\tau} \right) \\
\tilde{n} = n / \left[(\sigma_p^{l0} + \sigma_p^{0l}) i_p + (\sigma_L^{l0} + \sigma_L^{0l}) i_L + (\sigma_S^{l0} + \sigma_S^{0l}) i_S + \frac{l}{\tau} \right] \\
i_L = i_L^+ + i_L^- \\
i_S = i_S^+ + i_S^-
\end{cases} \quad (2.33.)$$

$$\begin{cases}
\frac{d}{dx} i_p = (\sigma_p^{l0} n_l - \sigma_p^{0l} n_0) i_p \\
\frac{d}{dx} i_L^\pm = \pm (\sigma_L^{l0} n_l - \sigma_L^{0l} n_0) i_L^\pm \\
\frac{d}{dx} i_S^\pm = \pm (\sigma_S^{l0} n_l - \sigma_S^{0l} n_0) i_S^\pm \pm \frac{\Omega}{4\pi} \frac{n_l}{\tau}
\end{cases} \quad (2.34.)$$

The boundary conditions are followed from the active medium geometry (fig. 2.8).

$$\begin{aligned}
i_L^+ \Big|_{x=0} &= i_L^- \Big|_{x=0} \\
i_S^+ \Big|_{x=0} &= i_S^- \Big|_{x=0} \\
i_p \Big|_{x=0} &= i_p^0
\end{aligned} \quad (2.35.)$$

In eq. (2.33 – 2.35) are used the following designations:

n_0, n_l, n the populations of down and up laser levels and total concentration of the color centers [cm^{-3}]

σ_α^{l0} and σ_α^{0l} the cross-sections of the transitions from up to down and from down to up laser levels [cm^2]. By subscripts is labeled the type of photons (P – pump, L – laser, S – ASE)

τ the characteristic time of the spontaneous transitions [sec]

i_α^\pm the intensity of the radiation (photons flow density) [$\text{cm}^{-2}\text{sec}^{-1}$]. By subscripts is labeled the type of photons, by superscripts the direction of propagation.

Ω the solid angle in which the amplification of spontaneous emission is taking place.

The problem (2.33 – 2.35) was solved numerically. For the calculations was used the following values of color center crystal parameters:

active medium length	l	8	cm
----------------------	-----	---	----

<i>active medium cross section</i>	<i>s</i>	<i>0.1</i>	<i>cm²</i>
<i>characteristic time of spontaneous emission</i>	τ	<i>55</i>	<i>nsec</i>
<i>color centers concentration</i>	<i>n</i>	3.0×10^{16}	<i>cm⁻³</i>

The behavior of the absorption and emission effective cross-sections as a function of the wavelength of radiation are shown in Fig. 2.9.

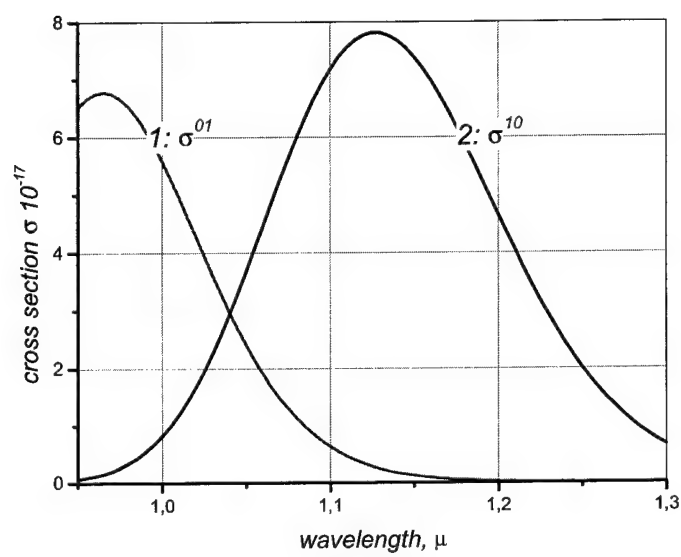


Fig.2. 9

2.3. Numerical modeling of color center laser with GIG cavity

The mathematical model was built allows to compute the spectral and energetic characteristics of GIG laser with color center crystal as an active medium. The object of numerical experiments were carried out was to determine the optimal parameters of the laser ensuring the single-longitudinal-mode laser operation with maximum efficiency. The parameters of the laser are presented in the Table 2.1.

At an introductory step of the investigation were determined the GIG laser characteristics as a function of diffraction grating efficiency (Fig. 2.10). The energy loss on the grating was not taken into account.

At the figure are shown the

behavior of the laser efficiency (left vertical axis, black curve) and the number of the lasing modes (right axis, color curves) as a function of the diffraction grating efficiency. The parameters of the laser are written out in the table above. The calculations were carried out for different grating incidence angles (87, 88, and 89 degrees). As it follows from the figure, for given laser

PARAMETER	VALUE	UNIT
cavity optical length	13	cm
active medium length	4	cm
active region diameter	0.1	cm
grating grooves frequency	1200	mm ⁻¹
grating incidence angle	89 – 80	deg
pump pulse duration	20	ns
pump pulse energy	10×10^{-3}	J
pump radiation wavelength	1060	nm
laser radiation wavelength	1150	nm

Table 2.1

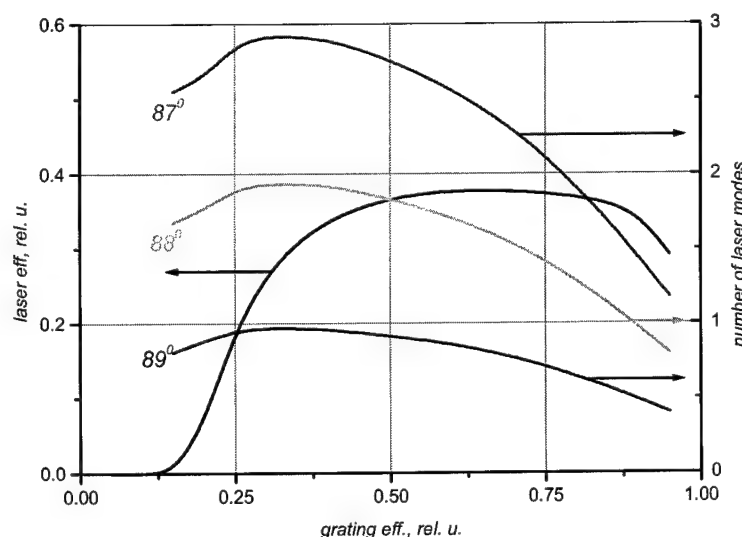


Fig. 2.10

parameters the optimal grating efficiency is equal approximately 50 % and angle of grating mounting required for SLM laser operation is 89° .

At the present moment the commercially available diffraction gratings for laser applications have a metal coating. The diffraction efficiency of the metallic gratings falls rapidly with increase of the radiation incidence angle. The energy loss of the grating due to the

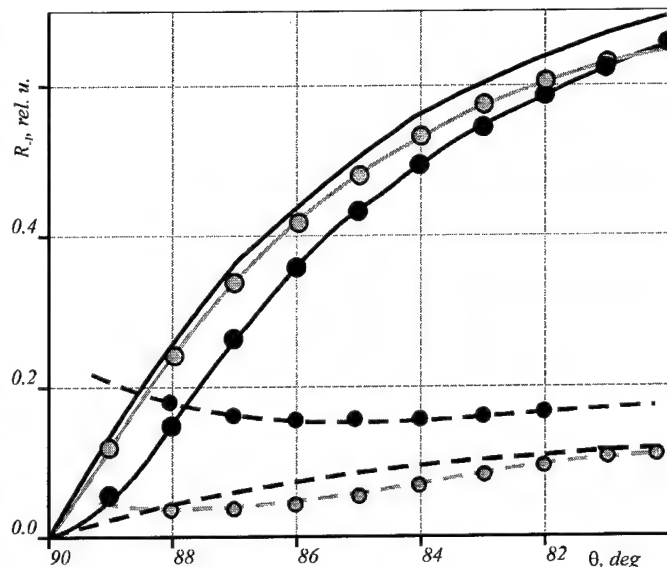
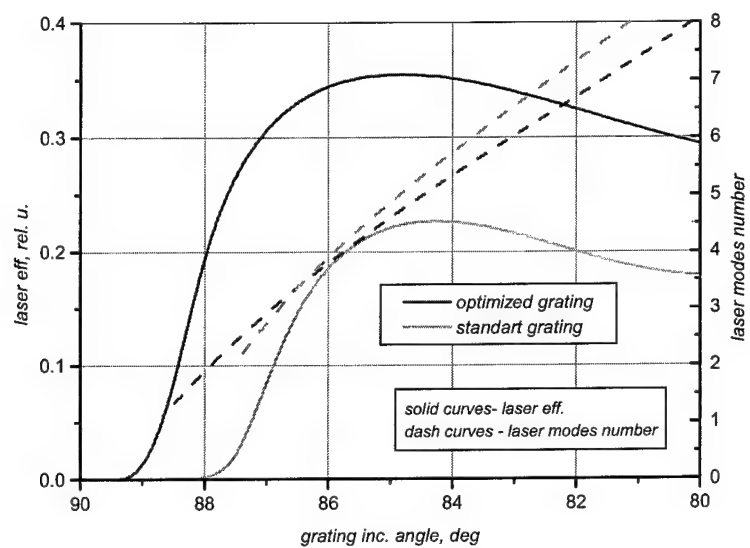


Fig. 2.11

absorption of the metal and scattering can amount some tens of percents. In Fig. 2.11 some results of the experimental measurements of diffraction grating efficiency in grazing incidence mounting are shown. The theoretical limit for sinusoidal aluminum grating is shown on the plot by black solid line without symbols. The efficiency of the gratings specially designed for the grazing mounting is enough close to the limit and its absorption is low. The general purpose gratings efficiency is smaller and its losses are enough high. For further calculations we will use two models of diffraction grating: "optimized" grating model (green curves in Fig. 2.11) and "standard" grating model (blue curves).

In Fig. 2.12 are shown the dependency of the laser efficiency (solid curves) and the number of lasing modes (dash curves) from the grating incidence angle. For the calculations were used the parameters of standard commercial grating (green curves) and parameters of the grating optimized for grazing incidence mounting (red curves). Is easy to see from the figure that efficiency of the standard grating is not enough to reach the SLM laser operation. The use of the grating with close-to-limit efficiency is allows to achieve the single-frequency lasing but the laser efficiency seems not high especially at the bounds of the active medium luminescence band. Thus our analysis shows that the basic obstacle for realization of the SLM color center laser with GIG cavity is low diffraction efficiency of the available gratings in grazing incidence mounting.

To resolve this problem the two approaches was considered. First – use of GIG scheme with intracavity beam expander. Second – use of novel types of diffraction gratings with improved grazing incidence mounting efficiency.

*Fig. 2.12*

2.4. Color center GIG laser with intracavity beam expander

2.4.1. Introduction

The one of the common ways to improve characteristics of dispersive laser cavities with diffraction grating is employ of intracavity beam expander [iii, iv]. The scheme of the laser cavity with beam expander is shown in Fig. 2.13. Let initially the radiation beam with frequency detuning $\delta\nu$ and diameter w propagates cavity along its axis from the back mirror to the grating (see Fig. 2.13). After the expansion the beam diameter increases K times there K is expansion factor. Due to the grating diffraction the beam obtains the angular deviation $\delta\varphi = \delta\varphi(\delta\nu)$ at the reverse cavity trip. After second pass through the expander the beam diameter restores to the initial value w , but the angular deviation takes the K times raise³. Thus the use of intracavity beam expander causes the increase of cavity dispersion proportional to the expansion factor.

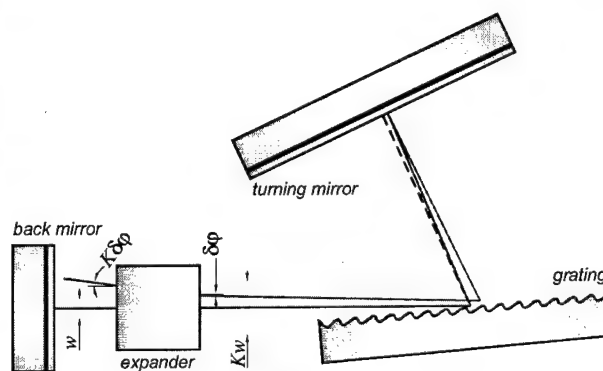


Fig. 2.13

Mounting of the beam expander into the laser cavity have, of course, the negative consequences like additional losses and increase of the cavity length. Moreover the use of the expander causes complication of the laser design and adjustment and deteriorate the laser beam quality.

At the moment the half-prism-beam-expander is most often used scheme for intracavity applications. This type of expander allows to reach required magnification with minimum negative effects. Usually such expander consists of even number of half-prisms⁴. The scheme of two prism beam expander is

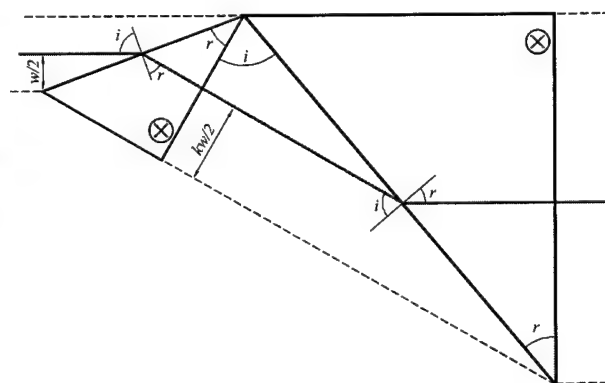


Fig. 2.14

³ In small angles approximation.

⁴ In the half prism radiation falls at right angle to one of its faces.

given in Fig. 2.14. Refraction angles of the prisms are set in inverse directions therefore such expander not change the beam direction and not have dispersion. The back face of the each prism have an AR coating and lose of the radiation is occurs due to reflection at the refract face of the prism. Let's determine the characteristics of the expander with number of prisms N and magnification factor K .

From given total magnification and prism number we can find the magnification of each prism

$$k = \sqrt[N]{K}, \quad (2.36.)$$

incidence and refraction angles of the prism

$$\begin{cases} \frac{\cos r}{\cos i} = k \\ \frac{\sin i}{\sin r} = n \end{cases} \Rightarrow \begin{cases} \sin r = \sqrt{\frac{k^2 - 1}{k^2 n^2 - 1}} \\ \sin i = n \sin r \end{cases} \quad (2.37.)$$

and transmission factor of the prism⁵

$$t = 1 - \frac{\operatorname{tg}^2(i - r)}{\operatorname{tg}^2(i + r)} = 1 - \frac{(n - k)^2}{(n + k)^2} = \frac{4nk}{(n + k)^2}. \quad (2.38.)$$

If w is the diameter of the initial beam, then the optical length for the prism pass l is determined by the following expression:

$$l = \frac{w}{2}(\operatorname{tgi} + nk \operatorname{tgr}) = wn \sqrt{\frac{k^2 - 1}{n^2 - 1}}. \quad (2.39.)$$

From the parameters of each prism we can find the total expander transmission T and optical length L :

$$\begin{aligned} T &= t^N = \left[\frac{4nk}{(n + k)^2} \right]^N, \\ L &= l \sum_{\alpha=0}^N k^\alpha = w \frac{n}{\sqrt{n^2 - 1}} \sqrt{\frac{(k + 1)}{(k - 1)}} (K - 1) \end{aligned} \quad (2.40.)$$

there K is the total expansion factor N – the total number of prisms, k – expansion factor of the single prism, n – prism material refraction index, w – expander entrance aperture.

The analysis of expressions (2.40) shows that the expander optical length groves proportionally with increase of the magnification factor and prism number. The behavior of the expander

transmission factor is more complex. It easy to show that under condition $k = n$ the prism incidence angle become equal to the Brewster angle and lose at the expander is vanish.

For the intracavity beam expander it compact design plays the major role. The magnification factor of the expander for GIG cavity usually not exceeds value $\times 10$. Therefore the expander prism number should be minimal and prism material refraction index – maximal to decrease lose of radiation. Thus we decided to use the two-prism-beam-expander and optical glass TF-46 as a prism material was chosen.

2.4.2. Optimization of the color center GIG laser with intracavity beam expander

The use of intracavity beam expander in GIG laser allows to increase grating incidence angle and improve it efficiency to an acceptable value without lose of the cavity dispersion. Undesirable influence of the loses at the expander and of the cavity lengthen is increase with enlarge of magnification factor. Therefore the optimization of the cavity and the expander parameters is required to reach the high laser efficiency.

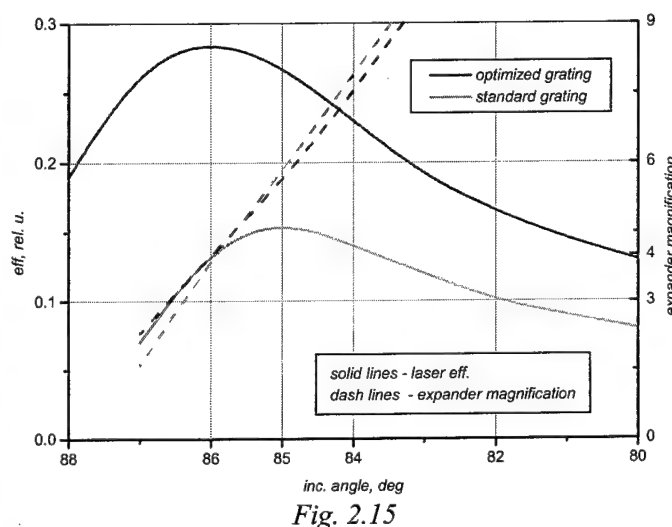


Fig. 2.15

Results of such optimization are presented in Fig. 2.15. On the picture the behavior of the laser efficiency (left axis) and the expander magnification factor required for SLM laser operation (right axis) as a function of the grating incidence angle are shown. The calculations was performed both for standard and optimized diffraction gratings (green and red curves respectively). With the help of the figure we can determine the optimal pair of the grating incidence angle and expander magnification (85 – 86 degrees and $4\times - 5\times$ magnification).

In Fig. 2.16 is presented the behavior of the laser characteristics as a function of lasing wavelength. The curves for standard grating are shown by green color and for optimized grating by red. Thus we can make the conclusion that use of the prism beam expander allows to provide effective SLM laser operation in a wide spectral region.

-
- i **Shoshan, I., Danon, N.N., and Oppenheim, U.P.** "*Narrow-band operation of pulsed dye laser without intracavity beam expansio.*" J. Appl.Phys. 48, 4495-4497. (1977).
 - ii **Littman, M.G., and Metcalf, H.J.** "*Spectrally narrow pulsed dye laser without beam expander*" Appl. Opt. 17, 2224-2227. (1978).
 - iii **Duarte, F.J., and Piper, J.A.** "A double prism beam expander for pulsed due lasers." Opt. Commun. 35 100-104. (1980)
 - iv **Racz, B., Bor, Z., Szatmari, S., and Szabo, G.** "Comparative study of beam expanders used in nitrogen laser pumped dye lasers." Opt. Commun. 36, 399-402. (1981).

3. Experimental realization of color center GIG laser

3.1 Intracavity beam expander

The carried out experiments have allowed to determine the required expander magnification and other expander parameters. To prevent the origin of the laser oscillations from the back faces of the prisms the angular parameters of the expander for experimental studies were slightly modified. The radiation incidence angle at the back faces of the prisms in expander were fabricated equal to 3° so that the transmission and magnification factors of the expander have not practically changed comparatively to theoretical values. To make the expander compact and easy to use it was designed as an integrated nonadjustable unit. The scheme of the expander is presented in Fig. 3.1 and its main parameters are written out in the Table 3.1.

PARAMETER		VALUE	
		THEORY	REAL
Prisms refraction index	n	1,71	1,71
first prism angle	α	$31^\circ 56'$	$33^\circ 45'$
Second prism angle	β	$31^\circ 56'$	$33^\circ 45'$
Angle between prisms	γ	$64^\circ 53'$	$62^\circ 00'$
Magnification factor	K	$\times 4.00$	$\times 4.1$
Optical length	L	0.64 cm	1.3 cm
Transmission factor	T	98.8%	98%
Deviation angle	a	0°	0°

Table 3.1

3.2 Gratings and mirrors

In our experiments the standard metal-coated holographic gratings and multi-layer dielectric coated mirrors were used. The gratings with 830, 1200 and 1600 grooves/mm with gold and aluminum coatings were tested. The Littrow mounting diffraction efficiency of the gratings was 96 % for gold-coated grating and 70 % for aluminum coated ones. The behavior of gold-coated grating efficiency depending on the grating incidence angle is presented in Fig. 3.2. The results of the experimental measurements are shown by circles. Theoretical results for grazing-angles-optimized gold-coated grating are shown by solid lines at the plot. The

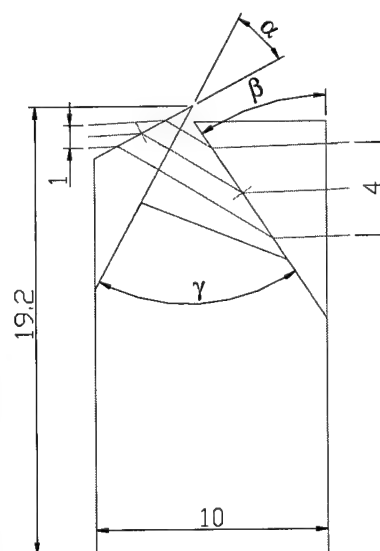


Fig. 3.1

diffraction efficiency of the gratings used is approximately 5 % lower and its absorption is 5 % higher than the theoretical prediction. The grating efficiency measurements were carried out for 1047 nm wavelength but the efficiency of metal coated gratings does not depend strongly on the wavelength (see Fig. 3.3). Therefore the efficiency of the grating within the color center laser operation region is practically the same.

The coating of the mirrors used provides reflection close to 100 % within the whole tuning range of the LiF:F_2^- laser. For the coupling of the pump laser radiation into the color center laser cavity the mirror with dichroic multi-layer coating was used. The transmission spectrum of the coupling mirror is presented in Fig.3.4. The coupler provides high transmission of the pump laser radiation and high reflection within the LiF:F_2^- laser oscillation wavelength region.

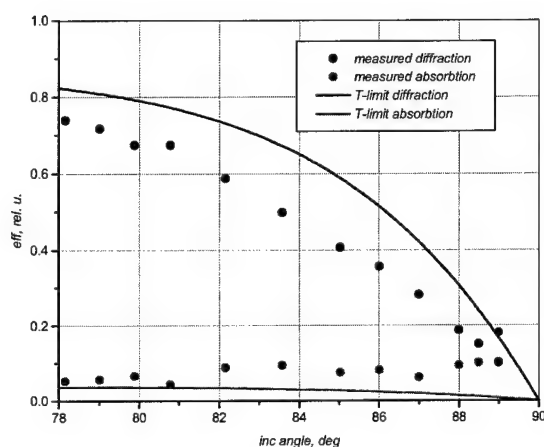


Fig. 3.2

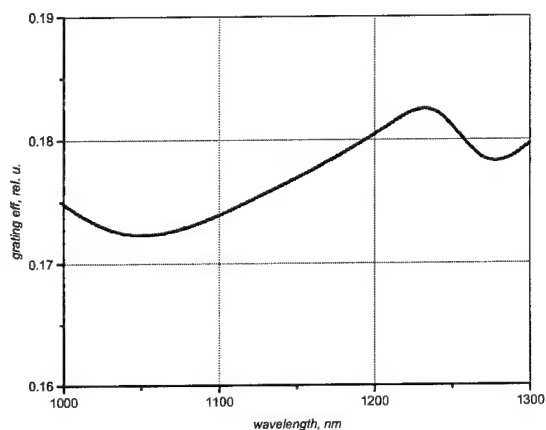


Fig. 3.3

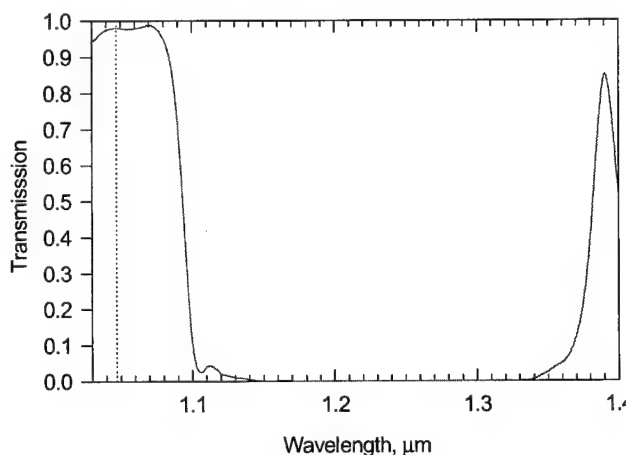


Fig. 3.4

Combined diffraction grating

The diffraction grating is the key element of GIG laser which determine its spectral characteristics and efficiency of the laser operation. As was revealed during the experiments the realization of the effective SLM color center laser with GIG cavity requires to use gratings with 40 – 50 % diffraction efficiency at the incidence angle about 89° . In the case of the tunable laser the grating should also keep high efficiency in the broad spectral region. Besides the grating should be resistant to high-peak-power radiation of the pulse laser.

The traditional holographic technology of the grating fabrication imply the metal coating of the periodically grooved surface formed in photoresist. The diffraction efficiency of the metal-coated grating falls rapidly with increase of the radiation incidence angle. The typical behaviors of the

metal-coated grating efficiency on the incidence angle are shown at the Fig. 3.5.

It should be noted that theoretical curves are presented on the graph. The efficiency of the best available metal-coated gratings is a few percents lower.

Our experience in the field of grating diffraction problem study allows to conclude that the main factor limiting the efficiency of the metal grating is the radiation absorption caused by of the finite conductivity of the metal. The

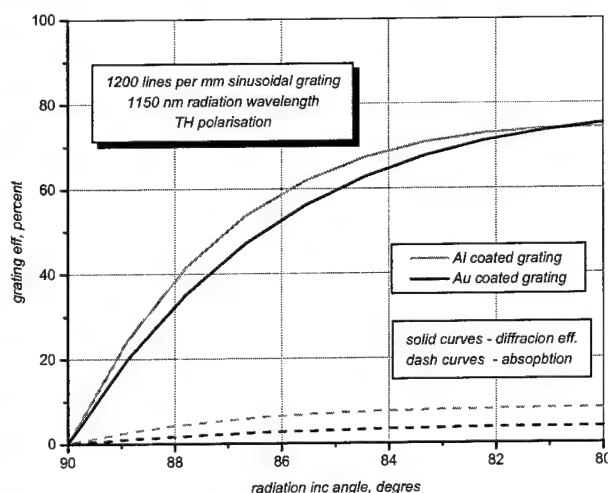


Fig. 3.5

absorption of the metal grating grows significantly when the direction of one of the diffraction orders approaches quasi-parallel to the grating surface (so called Woods anomalies). Such situation particularly takes place in the case of the grazing incidence grating mounting. Thus the value 15 – 20 % seems a reasonable estimation for diffraction efficiency of the metal-coated gratings in the spectral region of interest. This is rather low value to realize the effective color center GIG laser oscillations. Moreover due to absorption of the metal-coated grating the problem of its damage under pulse irradiation arises. As follows from the previous results the problem of the metal-coated gratings low efficiency can be solved by applying of the intracavity beam expander. However from our point of view the improvement of the grating efficiency in grazing incidence mounting has a great practical importance.

Combined diffraction gratings and it properties in the grazing incidence mounting

To prevent anomalous absorption at the resonant interaction of radiation with the grating it should be formed in non-absorbing dielectric material.

At the moment the so-called combined diffraction grating scheme is one of the most prospective ways to realize effective dielectric diffraction gratings. The scheme of combined diffraction grating is shown in Fig. 3.6. It was shown previously that efficiency of the combined grating at grazing incidence angles can exceed significantly the efficiency of traditional metal-coated gratings.

The behavior of the combined grating efficiency in grazing incidence mounting is illustrated by Fig. 3.7. If the under-grating mirror is formed by metal layer than grating efficiency in near IR spectral region can reach 50% at 2% absorption. Such dielectric-metal grating keep high diffraction efficiency in broad spectral range and this scheme is probably ideal for tunable laser applications. If multi-layer dielectric mirror is placed under the grating than the grating efficiency can reach 100 % limit but the spectral range of the pure dielectric grating is rather small if compared with the dielectric-metal grating. At the same picture the curve for metal-coated grating is also shown. It can be easily seen that its characteristics are worse.

Next figure (Fig. 3.8) allows to compare the characteristics of the color center GIG laser with traditional metal-coated grating and intracavity beam expander and characteristics of the laser with combined dielectric-metal grating (without expander). As follows from the figure application of combined grating allows to avoid the usage of the intracavity beam expander and obtain higher laser efficiency and broader tuning range. Laser design is also simplified significantly.

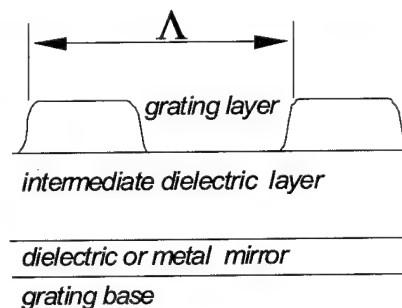


Fig. 3.6

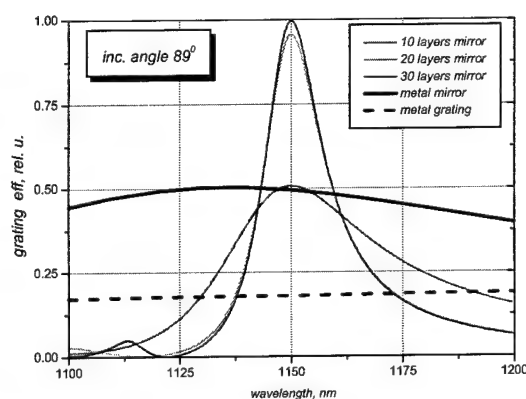


Fig. 3.7

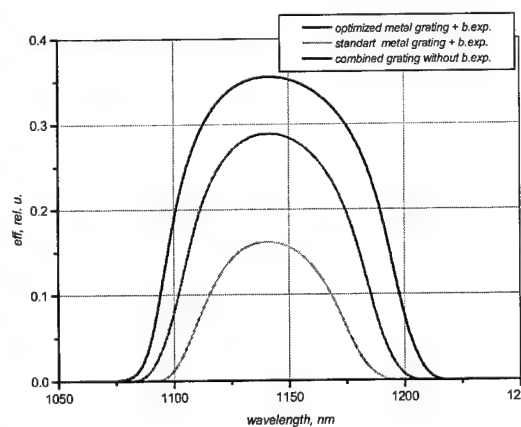


Fig. 3.8

3.3 Crystal preparation

The techniques of the active elements fabrication is very significant for the realization of the efficient LiF:F_2^- laser. One of the most important criteria of the active element quality is the proportion between the concentrations of active color centers and parasitic color centers in the crystal. Such parasitic color centers can cause both absorption and additional losses at the pump laser wavelength and the color center laser wavelength. In the case of the LiF:F_2^- laser the parasitic color centers are the F_3^-

color centers with maximum absorption at the 810 nm and aggregate color centers with absorption band in the 1150 - 1200 nm region.

The absorption spectrum of the fabricated LiF:F_2^- active crystals are shown at the Fig. 3.9. As follows from the figure, the maximum values of the F_2^- centers peak absorption

(960 nm) and the F_3^- centers absorption (800 nm) are approximately equal. Such proportion between F_2^- and F_3^- centers concentration allows to neglect the F_3^- color centers absorption at the pump laser wavelength $\lambda_{\text{pump}}=1047$ nm. The spectra measurements of 3 cm long crystals did not show any additional bands corresponding to the aggregate color centers absorption. It allows to use the value of 0.01 cm^{-1} as an upper estimation for the aggregate color centers absorption.

The active elements 4 cm long with two shape types were used in our experiments. The first type was the standard Brewster-angle-cut parallelepiped geometry. The second type was prism geometry of the active element (see Fig. 3.10-3.11). Such geometry of the active element allows use it as an intracavity beam expander.

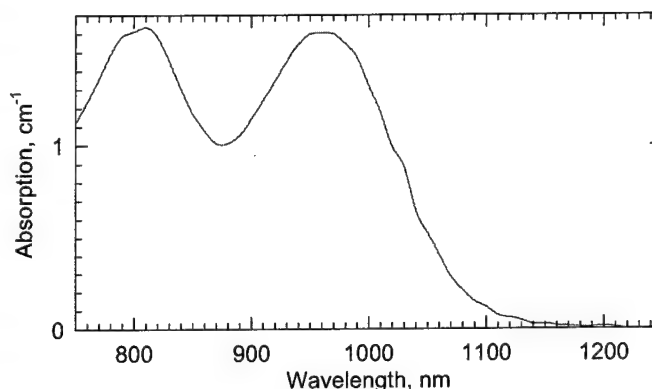


Fig. 3.9

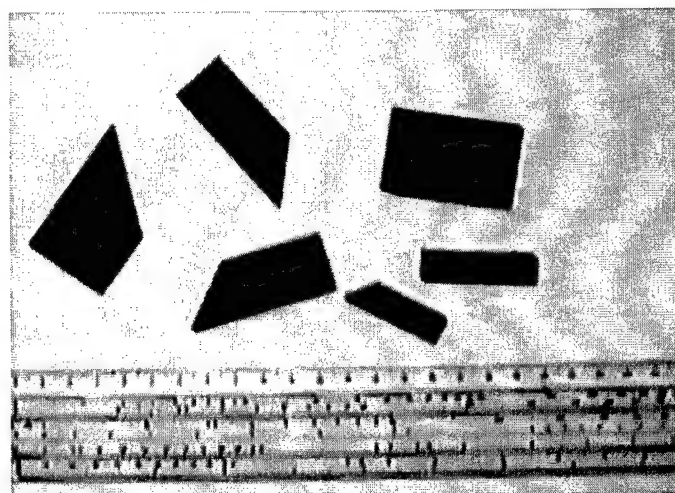


Fig. 3.10

Let's considering behavior of the beam expander magnification and transmission as a function of the prism refraction angle. The reflection from the active element surface is determined by Fresnel formula and depends on the radiation incidence angle, polarization and refraction

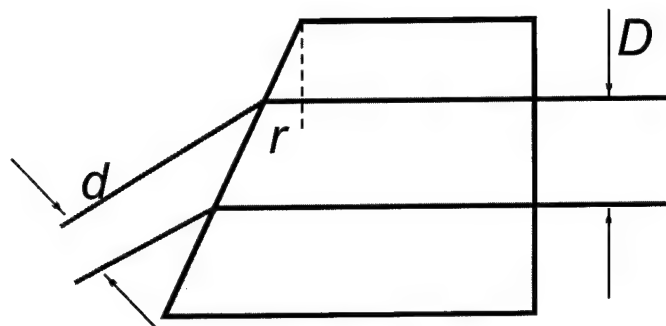


Fig. 3.11

index of the prism material ($n = 1.39$ for LiF crystal). The transmission and the magnification of the prism for the case of H polarization are determined by expressions (2.1-2.2). The theoretical behavior of the LiF prism reflection and magnification factors as a function of the prism refraction angle are shown at the Fig.3.12 (under the normal incidence of the radiation on the output face of the prism). At the normal incidence of the radiation on the prism face the reflection R of the prism is equal 3 % and magnification Γ is equal to 1. With increase of the

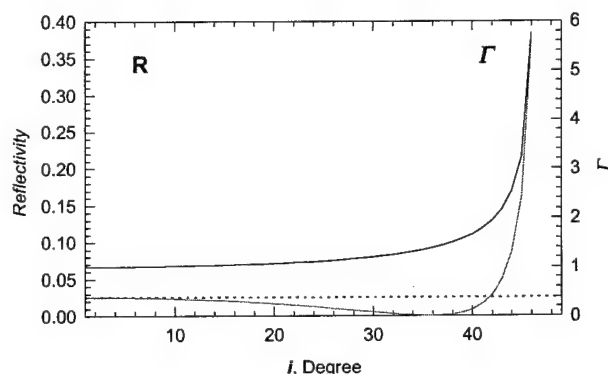


Fig. 3.12

prism angle from zero to the Brewster angle the prism reflection factor falls to zero and its magnification grows monotonously to $\Gamma = n = 1.39$. Further increase of the prism angle cause the rapid rise of the prism face reflection. For example at the prism angle $r = 42^\circ$ the face reflection becomes equal the normal incidence reflection (3%) and prism magnification grows to 1.94. The prism face reflection tends to 100 % and magnification factor to infinity when the prism angle approaches total internal reflection limit ($r = \arcsin(1/n) = 46^\circ$).

magnification grows to 1.94. The prism face reflection tends to 100 % and magnification factor to infinity when the prism angle approaches total internal reflection limit ($r = \arcsin(1/n) = 46^\circ$).

3.4 Pump laser

Our theoretical and experimental investigations have shown that small change in the pumping wavelength from 1064 to 1040 nm can result in two times increase of CC laser efficiency (Fig. 3.13) and extended tunable spectral range. The optimization of the pump lasers allowed to obtain tunable LiF:F_2^- CC laser operation with conversion efficiency over 50% with spectral linewidth of $\sim 2 \text{ cm}^{-1}$.

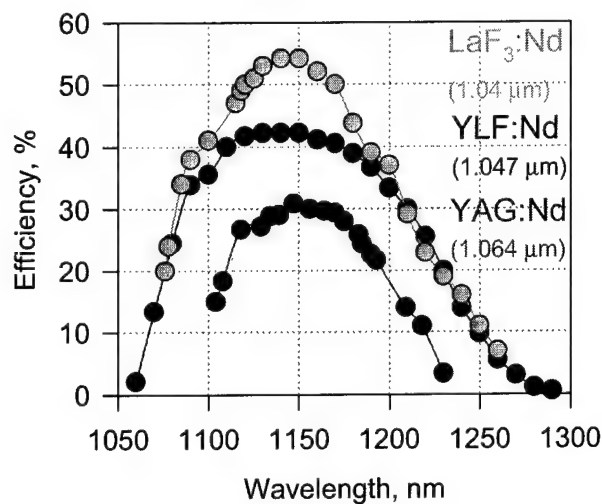


Fig. 3.13

As the pump source of the color center laser the pulsed YLF:Nd^{3+} laser with passive Q-switch was used. As the Q-switch element the LiF:F_2^- crystal with initial transmission about 16 % was used. The pump pulse frequency was 5-12 Hz, pump pulse energy was 10-30 mJ and pump pulse duration was 25 ns. The typical temporal shape of the pump pulse is shown in Fig. 3.14.

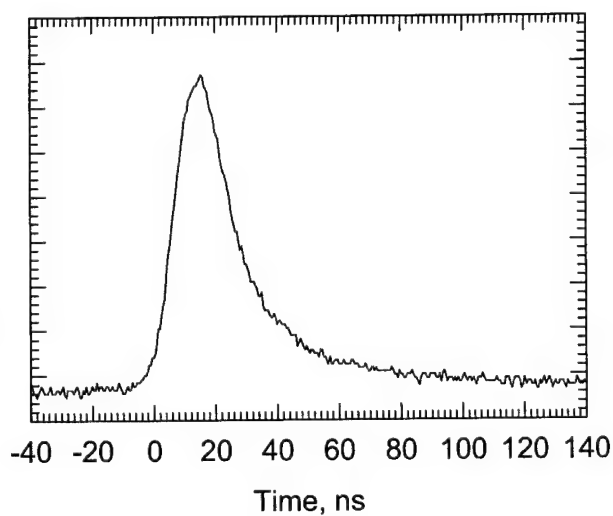


Fig. 3.14

3.5 The Measurements of the LineWidth of the Laser Oscillation

The spectral characteristics of the color center laser were measured by Fabry-Perrot interferometer (Burleigh, model RC-110). The second harmonic of the fundamental laser radiation was used for measurements. The interferometer base was varied from 2 to 150 mm. The mirrors reflection (84 %) provides the fines $FR=18$. Though the real fines of the interferometer measured using the single-frequency He-Ne laser was equal to 6. As the nonlinear element for second harmonic conversion of the fundamental laser radiation the KDP crystal was used. This nonlinear crystal has broad band synchronism ($\Delta\nu\approx 300\text{cm}^{-1}/\text{cm}$) in the LiF:F_2^- laser oscillation region. Therefore spectral shape of the LiF:F_2^- laser pulse can be measured via second harmonic radiation enough precisely. The interference pattern was registered by CCD array. The control system of the CCD linear array allows to make the snap-shots of the single laser pulse spectra.

3.6 Experimental results

The optical schemes of LiF:F_2^- CC laser utilizing diffraction gratings with 1200 grooves per mm were assembled. The pump radiation was transmitted by the entrance dichroic mirror, which has high reflection within 1.1-1.25 μm spectral region and more than 85% transmission at the pump wavelength(see Fig. 3.15).

In the experiments we used cavity schemes with grating and two mirrors or with additional grating working in autocollimation regime instead of turning mirror. At first we investigated the efficiency of the laser oscillation with respect to polarization. In this experiment plane parallel LiF:F_2^- CC crystal 27 mm long with 10% initial transmission was used as an active element. The dependence of the oscillation efficiency is shown in Fig. 3.16. One can see that the highest efficiency was obtained for radiation polarized in the grating plane. For perpendicular polarization the efficiency reduced 1.5 times. In the further experiments when not mentioned especially we used only horizontal polarization and Brewster cut LiF:F_2^- CC crystal as an active element. The dependencies of the oscillation efficiency at wavelengths of 1.15, 1.1, 1.2 μm are shown in Fig. 3.17. As one can

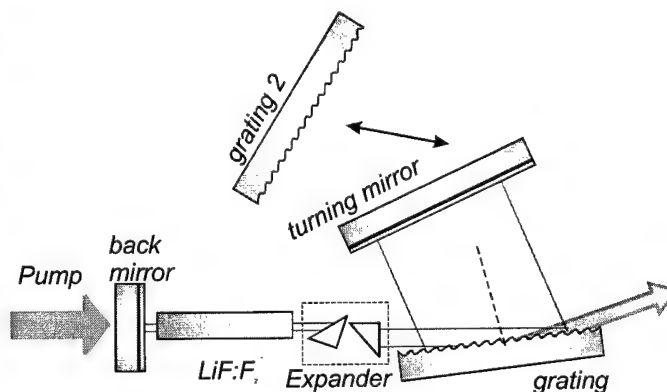


Fig. 3.15

see the efficiency in the maximum of the tuning curve ($\lambda = 1.15 \mu\text{m}$) was up to 13.5% and a little

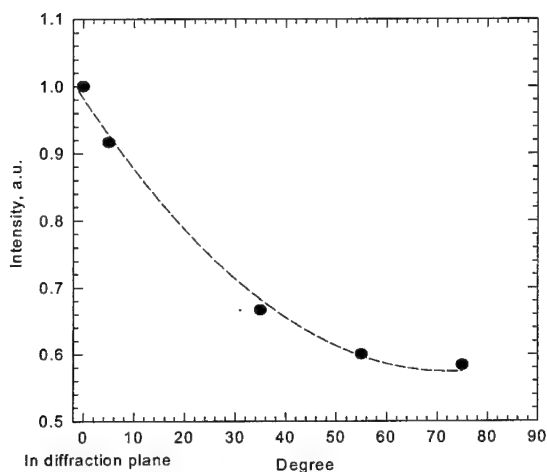


Fig. 3.16. The dependence of CC laser output on pump beam polarization.

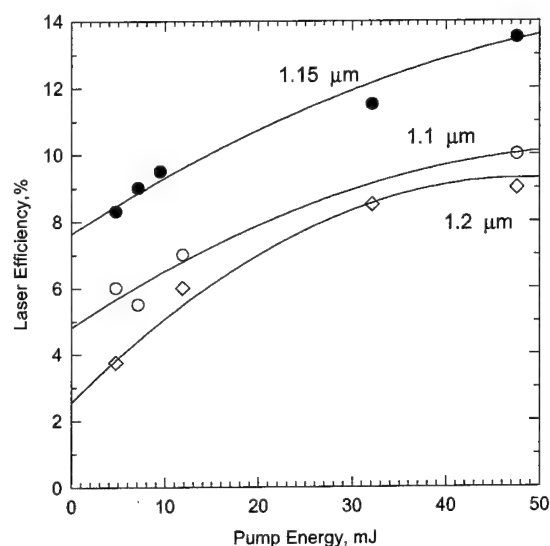


Fig. 3.17. The dependence of CC laser efficiency versus pump energy for three wavelengths 1.1, 1.15, 1.2 μm .

bit less at shorter wavelength ($\lambda = 1.1 \mu\text{m}$) $\eta=10\%$ and at longer wavelength ($\lambda = 1.2 \mu\text{m}$) $\eta=9\%$. The measured data on the output energy of the color center LiF:F_2^- laser for different incidence angles are presented in Fig. 3.18. The measured linewidths versus the incidence angle are demonstrated by the Fig. 3.19.

The linewidths were measured to be 0.05 cm^{-1} for case with turning mirror and 0.03 cm^{-1} with additional grating.

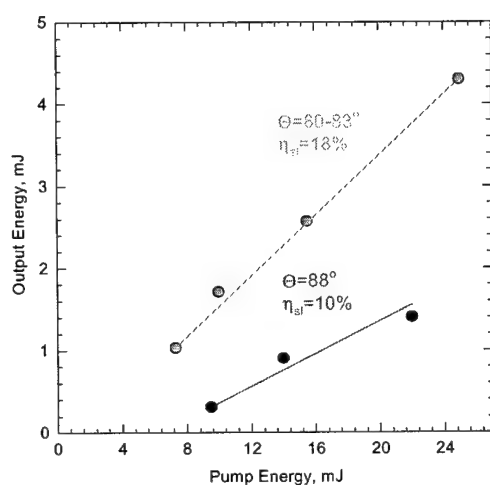


Fig. 3.18

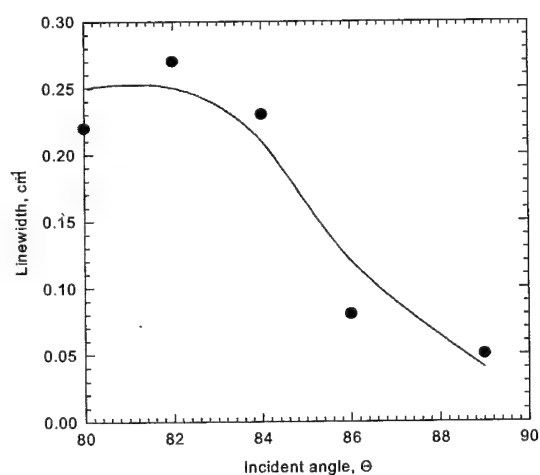


Fig. 3.19

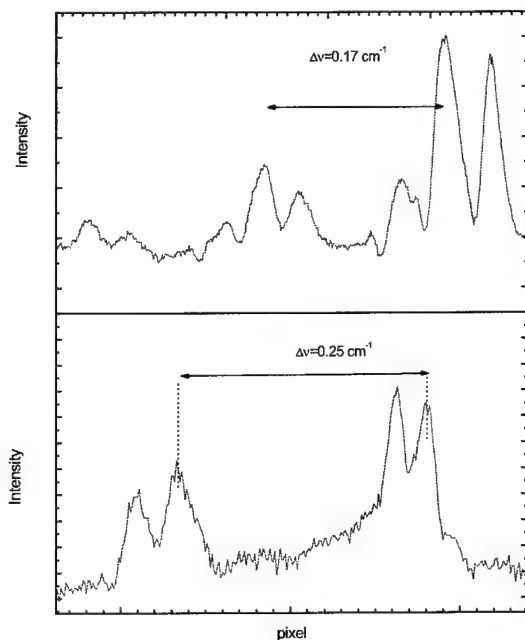


Fig. 3.20

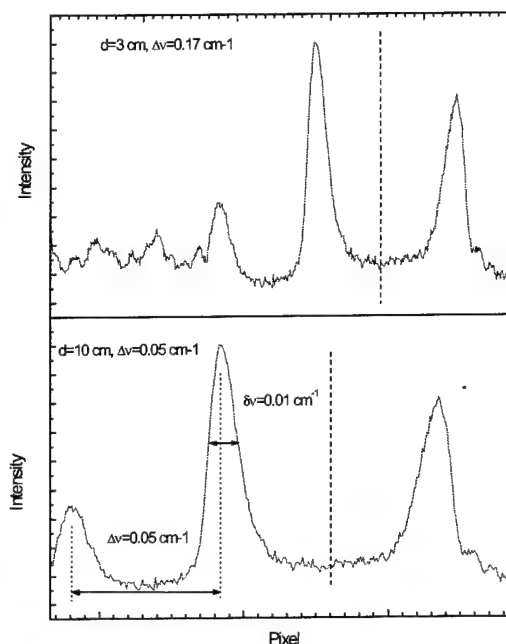


Fig. 3.21

The experimental LiF:F_2^- laser with standard Littman-Metcalf cavity equipped with 4 cm long Brewster-angle-cut parallelepiped active element and gold-coated diffraction grating was tested. The cavity optical length was equal to 13 cm (mode spacing 0.04 cm^{-1}). The pump laser radiation was focused inside the active element by 30 cm focal length lens. Between the active element and diffraction grating the prism-beam-expander was placed. The usage of the intracavity expander allowed to decrease the grating incidence angle and improve the laser efficiency without worsening the cavity dispersion. At the grating incidence angle about 85° the laser linewidth fluctuated from pulse to pulse in $0.08 - 0.12 \text{ cm}^{-1}$ limits (2 – 3 longitudinal modes lasing). The pulse to pulse variation of the central frequency of laser generation does not exceed 0.1 cm^{-1} . The interference patterns of double mode and triple mode laser pulses are shown in Fig. 3.20.

For improvement of the cavity dispersion the turning mirror was replaced by second aluminum-coated diffraction grating in Littrow mounting. For this cavity scheme with $86 - 87^\circ$ primary grating incidence angle the single-longitudinal mode operation of LiF:F_2^- laser was reached. The interference patterns obtained by 3 cm and 10 cm thick Fabri-Perout etalon are shown in Fig. 3.21. The laser line-width does not exceed the Fabri-Perout etalon resolution (0.01 cm^{-1}). The efficiency of the LiF:F_2^- laser was approximately 0.5 % at the pump pulse energy about 19 mJ.

The new optical scheme with the grazing angle was tested using the purchased grating with 1600 grooves/mm. As was discussed earlier the grating with 1600 grooves/mm has sufficiently higher dispersion within 1-1.2 μm wavelength region of interest (especially at the long wavelength edge near 1.2 μm). So substituting the 1200 grooves/mm grating should result in further decrease in narrowline laser oscillation linewidth. The following optical scheme was developed and tested (see Fig. 3.22). As grating with 1600 grooves/mm has the output into the

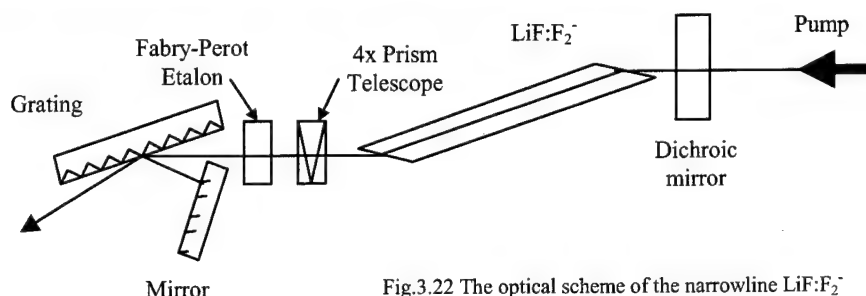


Fig.3.22 The optical scheme of the narrowline LiF:F_2^- color center laser with 1600 grooves/mm grating.

first diffraction order at 30° angle, to achieve compactness of the scheme the special small-shaped mirror was applied to form the feedback. Applied design allowed to obtain the total cavity length of only about 110 mm. The grating's grazing angle was chosen to be 82° . Additional spectra selective elements which were tested in different combinations were: specially designed and fabricated ultra compact 4x intracavity prism telescope and specially designed solid-state intracavity Fabry Perrot etalon with 60% reflectivity. These additional spectra selective elements were mounted in such a way that they could be easily inserted and removed from the cavity without its misalignment. The 40 mm long Brewster cut LiF:F_2^- active element was pumped with a YLF:Nd^{3+} laser ($\lambda=1.047 \mu\text{m}$). To increase the spectral selectivity of the narrowline LiF:F_2^- the pump radiation was tightly focused inside the active element by the lens with 300 mm focal length to form a narrow channel, playing the role of intracavity diaphragm to get TEM_{00} oscillation mode. schemes.

The results of the measurements are summarized in Table 3.2. It can be easily seen that applying of only 4x intracavity telescope resulted in the most efficient oscillation with total efficiency of about 11% and provided continuous wavelength tuning. Though the obtained linewidth in this case was also the largest and was measured to be about 0.06 cm^{-1} with internal multimode structure. It's necessary to mention here that the decrease of the total length for this type of the cavity to about 80 mm (with corresponding decrease in the number of oscillating modes) resulted in decrease of the oscillation linewidth to about $0.02\text{-}0.03 \text{ cm}^{-1}$ but the output beam's mode structure was strongly unstable. Inserting of the etalon instead of the telescope decreased the output efficiency to about 8%, but was accompanied by the decrease in the

oscillation linewidth due to small number of oscillating modes. The measured linewidth in this case was about 0.04 cm^{-1} . It's also necessary to say that the spectral stability for the scheme with intracavity etalon was higher with respect to the scheme with the intracavity telescope, though some mode beating was also observed. The combining of both intracavity telescope and Fabri Perrot etalon resulted in further drop of total laser efficiency up to about 3%. Nevertheless the linewidth was also the smallest and did not exceed 0.009 cm^{-1} . The recorded interferogram for this scheme is shown in Fig. 3.23. It's necessary to mention that the stability of this scheme was the best among the all investigated.

Table 3.2. Influence of additional spectra selective elements on total efficiency and linewidth of the narrowline LiF:F_2^- color center laser.

Spectra selective elements inserted	Total efficiency η , %	Laser linewidth $\Delta\nu$, cm^{-1}	Number of oscillating modes	Spectral stability
4x Prism Telescope	11	0.06	Multimode	Low
Fabri Perrot Etalon	8	0.04	2-3	Average
4x Prism Telescope + Fabri Perrot Etalon	3	0.009	~ 1	High

The well known advantage of the scheme with the grating placed at grazing angle is sufficiently narrower linewidth due to larger dispersion. At the same time schemes with the grating in the autocollimation scheme are less complex and more compact. To combine the advantage of the grazing scheme with the simplicity of the autocollimation one the special grating was ordered and purchased. This gold grating has

830 grooves/mm and its working angle within $1.19\text{-}1.2 \mu\text{m}$ operating range is close to 80° , which is not far from the optimal 85° incidence angle for the grazing scheme. The second diffraction

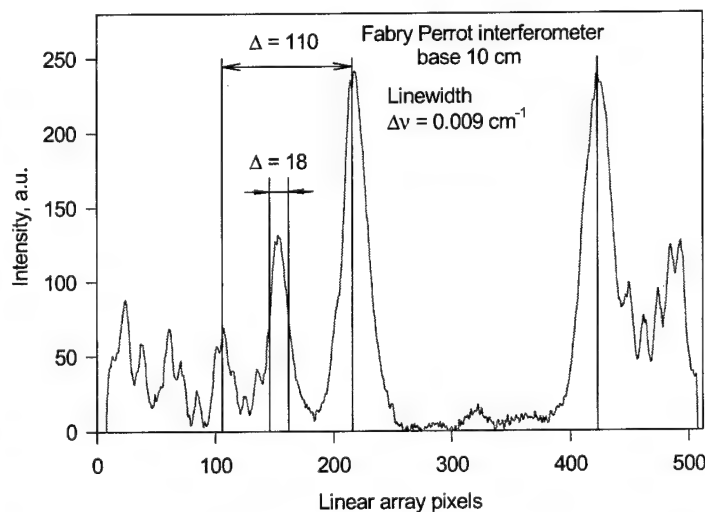


Fig. 3.23 The interferogram of the laser output measured by "Burleigh" Fabry Perrot interferometer with 10 cm base and CCD linear array.

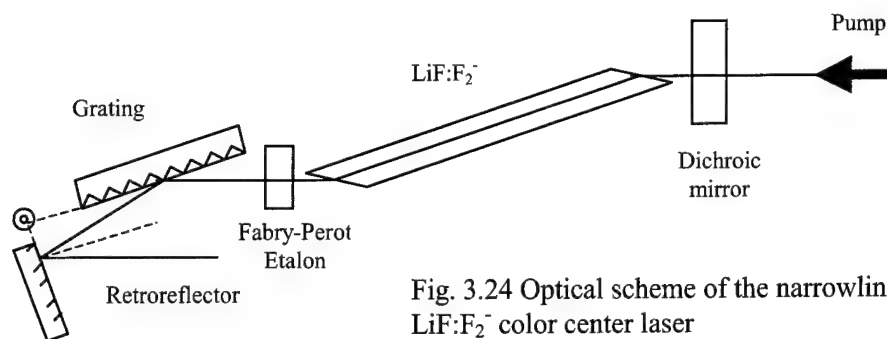


Fig. 3.24 Optical scheme of the narrowline tunable LiF:F_2^- color center laser

order of the 830 grooves/mm grating (25x25 mm size) is used to form the feedback. The zero diffraction order is used as the laser output. As was discussed previously the grating with 1600 grooves/mm has sufficiently higher angle dispersion D within 1.19-1.2 μm range as compared to diffraction gratings with 1500 and 1200 grooves/mm.

The diffraction efficiency of the purchased grating in the second diffraction order for radiation polarized parallel to the grating's grooves $E(\parallel)$ was measured to be about 80% in the maximum of the LiF:F_2^- color center laser tuning curve and steadily dropped with wavelength increasing. Within 1.19-1.2 μm range the corresponding diffraction efficiency was measured to be about 35%. The part of the incidence radiation diffracted into the first diffraction order was less than 5% in the whole wavelength range 1.07-1.2 μm . The optical scheme of the laser using this grating is shown in Fig. 3.24.

The LiF:F_2^- color center laser was pumped by the passively Q-switched YLF:Nd laser operating at 1.047 μm . The output energy of the pump laser was about 35 mJ and was naturally horizontally polarized.

As was mentioned above the diffraction efficiency (80%) at wavelengths shorter than 1.18 μm is excessively high to form the optimal feedback for LiF:F_2^- color center laser oscillations. So to test the operation at shorter wavelengths the scheme was modified. As was discussed previously the diffraction efficiency of the grating depends on the polarization of the incidence radiation. To decrease the diffraction efficiency the scheme was rebuilt for the incidence radiation polarized perpendicular to the grating's grooves $H(\perp)$ (Brewster cut active element was mounted accordingly). The polarization of pump radiation was rotated using a half wave plate.

The color center laser operated without intracavity etalon for both polarizations. The total efficiency of LiF:F_2^- color center laser for two working polarizations is shown in Fig. 3.25. As can be seen from the Fig. 3.25 the efficiency at the maximum of the tuning curve for $H(\perp)$ polarization is high enough and achieves about 20%. This indicates that the feedback formed by the grating is close to optimal. Nevertheless one can notice fast drop of the laser efficiency at the

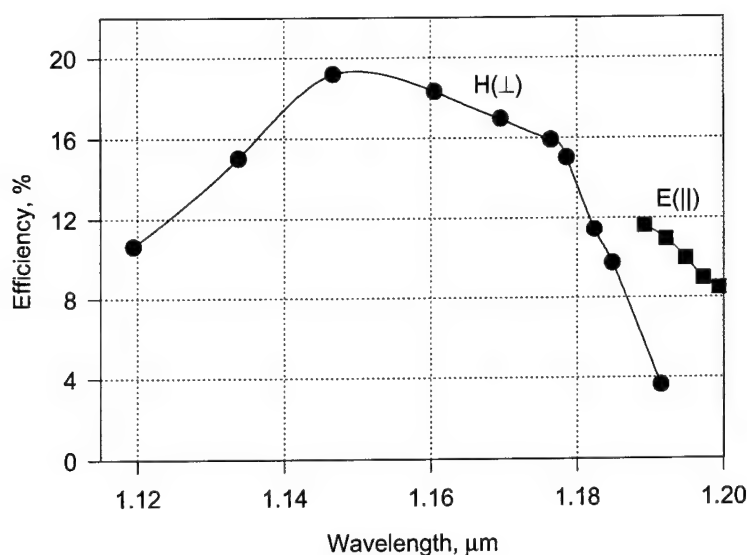


Fig. 3.25 The tuning curve of the LiF:F_2^- color center laser with 830 grooves/mm grating in autocollimation scheme with vertical (circles) and horizontal (squares) working polarization.

long wavelength wing of the tuning curve. This is due to fast drop of the grating's diffraction efficiency for longer wavelengths. At the same time we can see that the scheme with horizontal polarization $E(\parallel)$ has higher efficiencies within 1.19-1.2 mm range (about 10%) with respect to vertical one $H(\perp)$ (only few percent).

The linewidth of the laser was measured using the "Burleigh" Fabry-Perot interferometer. The scheme with horizontal working polarization $E(\parallel)$ was applied. Due to large incidence angle the illuminated aperture of the grating was about 15 mm. Without any additional selective elements inside the cavity the linewidth of the laser was measured to be 0.3 cm^{-1} which is about ten times less than that for similar scheme with 1200 grooves/mm grating in autocollimation regime. To obtain narrower linewidth additional spectral selective elements should be added to the optical scheme. Due to the limited aperture of the used grating the placement of intracavity telescope was senseless as practically all grating was illuminated even without any type of beam expander. Several Fabry-Perot etalons of different shape and transmittance were tested to evaluate their influence on the resulting linewidth. The results of the test are summarized in Table 3.3.

Table 3.3. Output energy, efficiency and linewidth of the LiF:F_2^- color center laser with different intracavity etalons.

Type of Fabri-Perrot etalon	CC laser output energy, mJ	CC laser total efficiency	CC laser linewidth, cm^{-1}
60% reflectivity, 10 mm thickness	1.2	3.4 %	0.1
85% reflectivity, 3 mm thickness	0.6	1.7 %	0.09
92% reflectivity, 3 mm thickness	0.4	1.1 %	0.08

As can be seen from the table the Fabry-Perot interferometer with 60% reflectivity ensured 3 times narrowing of the laser linewidth accompanied by approximately twice drop in laser efficiency. Further increase of the Fabry-Perot etalon reflectivity improved the output laser linewidth lead to sufficient drop in the output laser efficiency.

Because of low efficiency of the SLM color center laser the some new variants of Littman-Metcalf cavity scheme was proposed and studied. From our point of view the displacement of the active element from narrow to the wide cavity arm looks very prospective. Such modification of the cavity allows to increase significantly the

active volume of the laser and thus improve the laser output power. In the first series of the experiments with improved Littman-Metcalf cavity the narrow transverse size active element and intracavity prism beam expander was used. The scheme of the cavity is shown in Fig. 3.26. The cavity optical length was about 20 cm. At the grating incidence angles 87 and 88.5 degrees the laser linewidth 0.2 – 0.15 and 0.1 cm^{-1} respectively was reached.

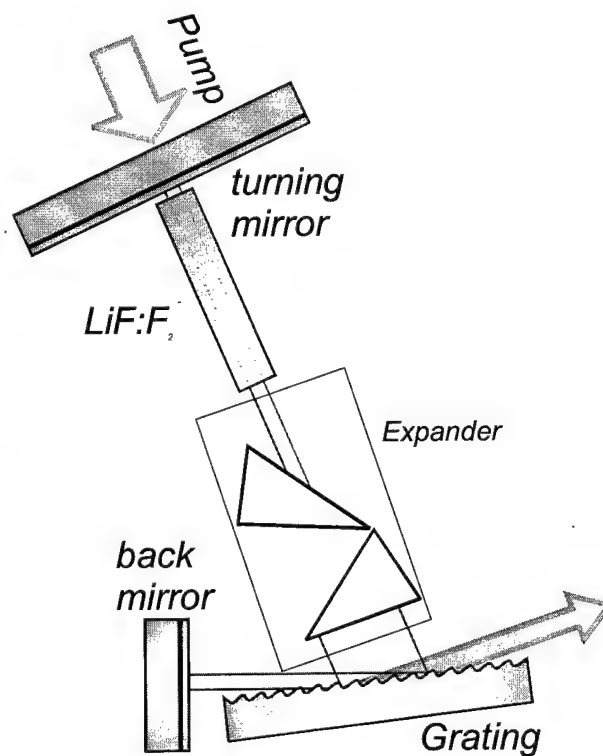


Fig. 3.26

In the second series of the experiments the wide aperture active element with prism geometry was used. Such geometry allows to incorporate the active element and intracavity beam expander and decrease the cavity length to 12 cm. Simultaneously with the intracavity beam expansion the extracavity pump beam expansion was used. The scheme of the laser cavity is shown in Fig. 3.27. At the grating incidence angle about 87 degrees the laser linewidth was equal approximately 0.15 cm^{-1} and does not changes at the variation of the pump beam size from 3 to 30 mm. For further

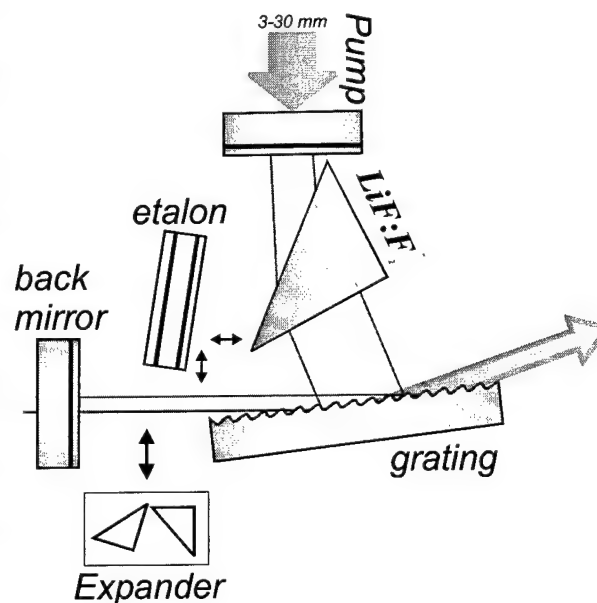


Fig. 3.27

narrowing of the laser spectra the $4\times$ prism beam expander was mounted in the narrow cavity arm. As a result the laser linewidth was decreased to 0.15 cm^{-1} . The replacement of the beam expander by 1 mm thick etalon allowed to reach the SLM laser operation. The laser efficiency was equal 0.1 % at the pump pulse energy about 40 mJ. We suppose that the fall of the laser efficiency comparatively to the scheme shown in Fig. 3.26 is caused by extra losses of the output radiation.

The cavity scheme with etalon mounted in the wide cavity arm was also tested. For this scheme the SLM operation of LiF:F_2^- laser was reached for the grating incidence angle about 85° . To find the cavity parameters which provides maximum laser efficiency the different etalons were tested. But decrease of the etalon reflectivity resulted in the laser linewidth increase. When the etalon was removed from the cavity the laser linewidth grew up to 0.32 cm^{-1} and laser efficiency was about 4.5 %.

3.7 Experimental realization of color center GIG laser with combined diffraction grating

For the experimental examination of the theoretical results the combined diffraction grating was prepared and experimental study of its characteristics was performed. Due to technological reasons the pure dielectric grating scheme was chosen. As a base of the grating the 10-layer $\text{HfO}_2/\text{SiO}_2$ mirror was used. The scheme of the experimental grating is shown in Fig. 3.28. The

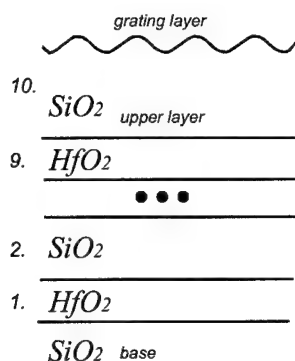


Fig. 3.28

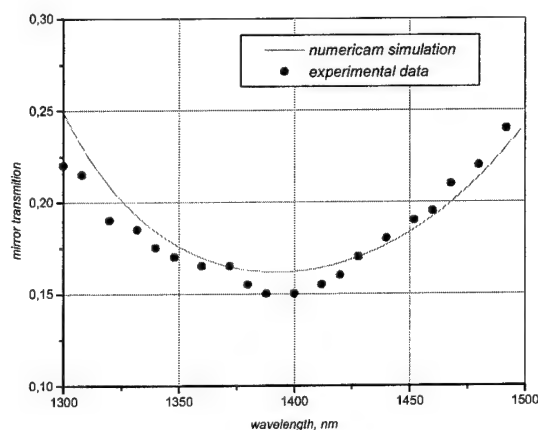


Fig. 3.29

grating depth and the mirror layers thickness were optimized to reach maximum diffraction efficiency at the radiation wavelength 1185 nm and incidence angle 89° .

The transmission curve of the grating base mirror is shown in Fig. 3.29. The theoretical transmission curve for the mirror with required parameters is plotted by solid line the results of experimental measurements are shown by circles. Thus the deviation of the grating base parameters from the theoretical requirements does not exceed 1 – 2 %.

The behavior of diffraction efficiency of the grating was formed at the top of multi-layer base is given in Fig. 3.30. By solid line and by circles are shown the results of numerical simulation and of the experimental measurements respectively. Comparison of the theoretical and experimental results allows to conclude that our estimations are confirmed with good precision.

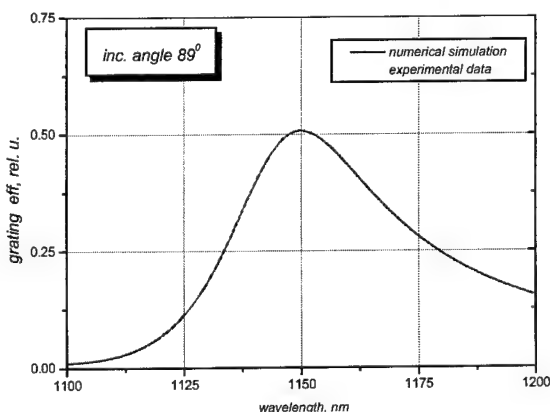


Fig. 3.30

4. Mathematical modeling of the color center laser amplifier

4.1. Interaction of the radiation with the active medium

The scheme of the $LiF:F_2^-$ color center crystal energy levels is shown in Fig. 4.1. The interaction of the radiation with such active medium can be explained by the following most important processes:

- ❖ stimulated absorption and emission at the pump laser wavelength (P1);
- ❖ stimulated absorption and emission at the color center laser wavelength (C1)
- ❖ spontaneous emission at the color center laser wavelength (C2)

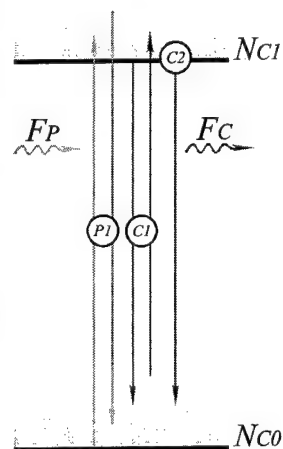


Fig. 4.1

Thus, the rate equations for energy levels populations in the $LiF:F_2^-$ color center crystal can be written as follows:

$$\begin{cases} \dot{N}_{C1} = (N_{C0}\sigma_P^{(01)} - N_{C1}\sigma_P^{(10)})F_P + (N_{C0}\sigma_C^{(01)} - N_{C1}\sigma_C^{(10)})F_C - N_{C1}/\tau_C \\ N_C = N_{C1} + N_{C0} = \text{const} \end{cases} \quad (4.1.)$$

here N_{C0} and N_{C1} are lower and upper laser levels populations [cm^{-3}]; N_C - the total concentration of the color centers in the crystal [cm^{-3}]; F_P - pump radiation photons flow intensity [$\text{sec}^{-1}\text{cm}^{-2}$]; F_C - color center laser radiation photons flow intensity [$\text{sec}^{-1}\text{cm}^{-2}$]; $\sigma_\lambda^{(01)}$ and $\sigma_\lambda^{(10)}$ - the effective cross-sections of the stimulated absorption and emission at the wavelength λ [cm^2]; τ_C - the characteristic time of the spontaneous luminescence from the upper laser level [sec].

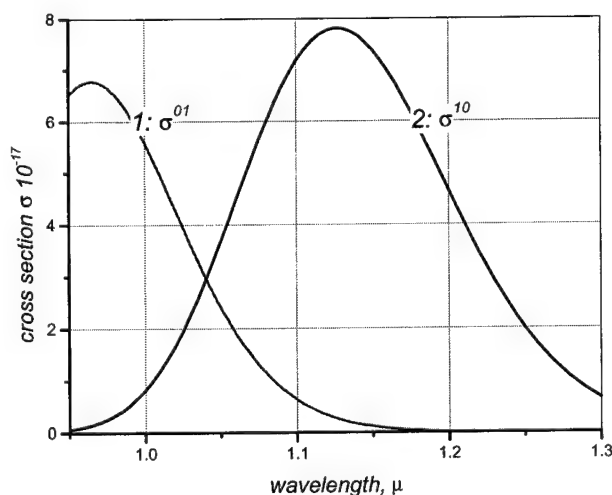


Fig. 4. 2

The behavior of the absorption and stimulated emission effective cross-sections as a function of the radiation wavelength is shown in Fig. 4.2. Typical concentration of the color centers in the active crystal is equal approximately to $3 \times 10^{16} \text{ cm}^{-3}$. The characteristic time of spontaneous luminescence decay is about 55 nsec.

4.2. Mathematical model of the color center laser amplifier

Two optical schemes of the longitudinally pumped color center laser amplifier cell were considered: the single and the double pass amplifiers (see Fig. 4.3). In the single pass amplifier (lower drawing) the pump and the probe radiation beams are collinear. In the double pass amplifier (upper drawing) the pump beam couples in the active element through the dichroic mirror M . The probe beam couples into the active element from the opposite side and passes it twice because of the reflection at the back mirror.

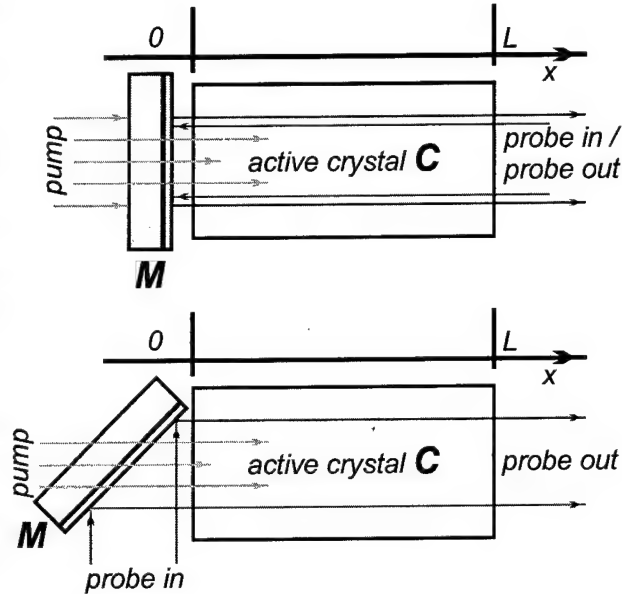


Fig. 4.3

Let's consider firstly the double pass amplifier scheme. The three types of the radiation propagate inside the active medium: the pump radiation, the probe radiation and the amplified spontaneous emission (ASE) radiation. Therefore the rate equations for this system have a form:

$$\begin{cases} \dot{N}_{CI} = (N_{C0}\sigma_P^{(0I)} - N_{CI}\sigma_P^{(I0)})F_P + (N_{C0}\sigma_C^{(0I)} - N_{CI}\sigma_C^{(I0)})F_C \\ \quad + (N_{C0}\sigma_S^{(0I)} - N_{CI}\sigma_S^{(I0)})F_S - N_{CI}/\tau_C \\ N_C = N_{CI} + N_{C0} = \text{const} \end{cases} \quad (4.2.)$$

Both the probe and the ASE radiation should be considered as pairs of separate beams which have the opposite directions. Thus we can write transfer equations for radiation in the form as follows:

$$\begin{cases}
\left(\frac{1}{c} \frac{\partial}{\partial t} + \frac{\partial}{\partial x}\right) F_P = (-N_{C0} \sigma_P^{(0l)} + N_{Cl} \sigma_P^{(l0)} - k_P) F_P \\
\left(\frac{1}{c} \frac{\partial}{\partial t} \pm \frac{\partial}{\partial x}\right) F_C^\pm = (-N_{C0} \sigma_C^{(0l)} + N_{Cl} \sigma_C^{(l0)} - k_C) F_C^\pm \\
\left(\frac{1}{c} \frac{\partial}{\partial t} \pm \frac{\partial}{\partial x}\right) F_S^\pm = (-N_{C0} \sigma_S^{(0l)} + N_{Cl} \sigma_S^{(l0)} - k_S) F_S^\pm + \omega N_{Cl} / \tau_C
\end{cases} \quad (4.3.)$$

where the upper index at the photon flows variables designates the direction of the corresponding beam; k_λ – the parasitic absorption factor at wavelength λ [cm⁻¹]; and the factor ω specifies the fraction of spontaneously emitted photons that initiates ASE process.

The equations system (4.2, 4.3) should be completed by initial and boundary conditions. These additional conditions are the pump and the probe pulses temporal shape and reflection conditions at the dichroic mirror M :

$$\begin{cases}
F_P(x=0, t) = F_P^{(0)}(t) \\
F_C^-(x=L, t) = F_C^{(in)}(t) \\
F_S^-(x=L, t) = 0 \\
F_C^+(x=0, t) = F_C^-(x=0, t) \\
F_S^+(x=0, t) = F_S^-(x=0, t)
\end{cases} \quad (4.4.)$$

The mathematical model of the single pass amplifier is quite similar to that presented above. The only difference is different boundary conditions and the absence of the negative direction probe beam:

$$\begin{cases}
\left(\frac{1}{c} \frac{\partial}{\partial t} + \frac{\partial}{\partial x}\right) F_P = (-N_{C0} \sigma_P^{(0l)} + N_{Cl} \sigma_P^{(l0)} - k_P) F_P \\
\left(\frac{1}{c} \frac{\partial}{\partial t} + \frac{\partial}{\partial x}\right) F_C^+ = (-N_{C0} \sigma_C^{(0l)} + N_{Cl} \sigma_C^{(l0)} - k_C) F_C^+ \\
\left(\frac{1}{c} \frac{\partial}{\partial t} \pm \frac{\partial}{\partial x}\right) F_S^\pm = (-N_{C0} \sigma_S^{(0l)} + N_{Cl} \sigma_S^{(l0)} - k_S) F_S^\pm + \omega N_{Cl} / \tau_C
\end{cases} \quad (4.5.)$$

$$\begin{cases}
F_P(x=0, t) = F_P^{(0)}(t) \\
F_C^+(x=0, t) = F_C^{(in)}(t) \\
F_S^+(x=0, t) = 0 \\
F_S^-(x=L, t) = 0
\end{cases} \quad (4.6.)$$

The presented mathematical model allows to determine parameters of the longitudinally pumped color center laser amplifier in the uniform beam approximation. For the numerical solution of the boundary value problems (4.2, 4.3, 4.4) and (4.2, 4.5, 4.6) the amplifier simulation software program was developed.

4.3. The amplifier cell simulation results

The basic parameters of the color center laser amplifier cell used in our calculations are presented in the table below.

VARIABLE	DESCRIPTION	VALUE	UNITS
λ_p	<i>pump laser wavelength</i>	1.06	μ
λ_c	<i>probe laser wavelength</i>	1.15	μ
λ_s	<i>ASE radiation probe laser wavelength</i>	1.15	μ
$\sigma_p^{(01)}/\sigma_p^{(10)}$	<i>effective cross-section of the stimulated emission/absorption at the pump laser wavelength</i>	1.9/4.5	$\times 10^{-17} \text{ cm}^2$
$\sigma_c^{(01)}/\sigma_c^{(10)}$	<i>effective cross-section of the stimulated emission/absorption at the probe laser wavelength</i>	0.1/7.4	$\times 10^{-17} \text{ cm}^2$
$\sigma_s^{(01)}/\sigma_s^{(10)}$	<i>effective cross-section of the stimulated emission/absorption at the ASE radiation wavelength</i>	0.1/7.4	$\times 10^{-17} \text{ cm}^2$
τ_c	<i>the characteristic time of the spontaneous decay</i>	55	nsec
N	F_2^- color centers concentration	3×10^{16}	cm^{-3}
L	<i>the active element length</i>	8	cm
	<i>pump radiation intensity</i>	0.4	$\text{J} \times \text{cm}^{-2}$
	<i>pump pulse duration</i>	20	nsec

At the first step of investigation the comparison of the single pass and double pass amplifier schemes was carried out. In Fig. 4.4 the behavior of the amplifier parameters as a function of the ratio of the probe to pump pulse energy is shown. The amplifier efficiency is shown with red curves (left vertical axis), the amplifier gain – with blue curves (right vertical axis), solid lines corresponds to the double pass

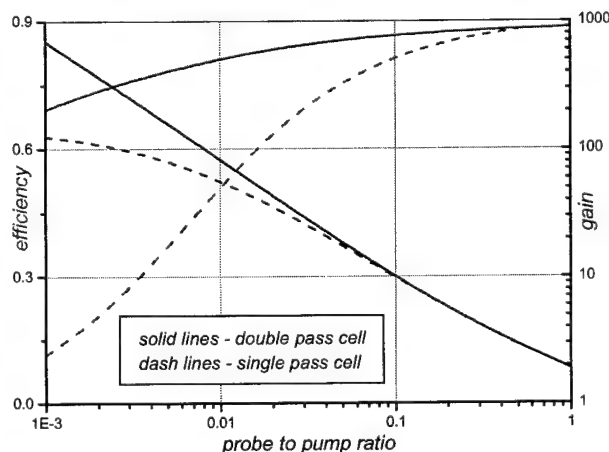


Fig. 4. 4

amplification scheme, dashed lines – the single pass scheme (see graph legend). It is easy to see from the plot, that double pass amplifier cell scheme has a significant advantage. The benefit of the double pass scheme became most obvious at the low level of the probe signal.

The disagreement of the pump and probe pulses temporal

shape is one of the most common problems of the experimental realization of master-oscillator-power-amplifier (MOPA) pulse laser systems. Usually the pulse duration could be shortened in the master oscillator so the amplifier pump pulse duration becomes slightly longer than the input probe pulse. Fig. 4.5 allows to estimate the influence of temporal disagreement on the amplifier parameters. The results of the amplifier calculations for equal pump and probe pulse durations (20 nsec) are shown by solid curves; and for probe pulse twice shorter than the pump pulse are shown with dashed curves. The Gaussian temporal shapes of the pulses were considered. It is easy to see that the pulse duration disagreement causes noticeable fall of the amplifier efficiency, but this fall is not so high that requires special efforts to equalize pulse durations.

One more factor limiting the amplifier efficiency is the parasitic absorption in the active medium. In the $LiF:F_2^-$ crystal the parasitic absorption is mostly due to F_3^- and other aggregate colloidal color centers. The exact value of the losses strongly depends on the active element fabrication technology. We carried out the amplifier simulation with the parasitic absorption factor k equaled to 0.02 cm^{-1} . This value can be used

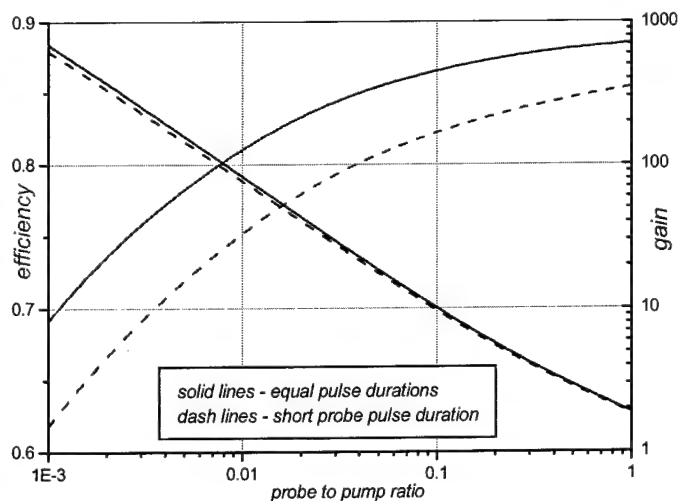


Fig. 4. 5

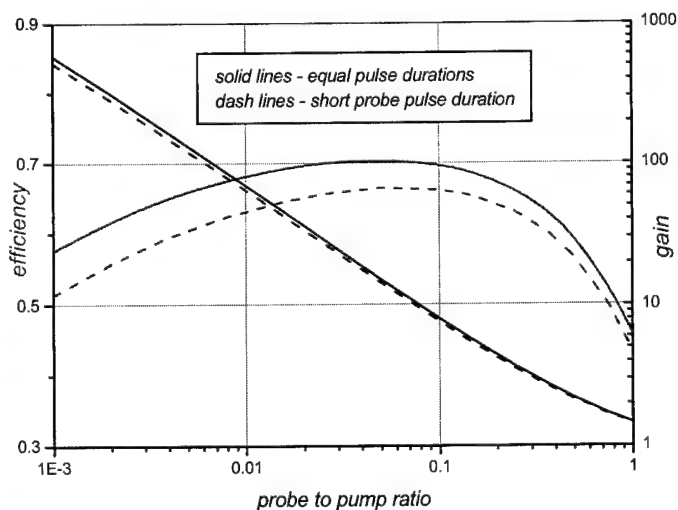


Fig. 4. 6

as a good upper estimation for parasitic absorption. The calculation results are shown in Fig. 4.6. Similar to the previous plot the results for pump and probe pulses with non-equal durations are shown by dashed lines. It is obvious that the parasitic absorption appears to be more important when the amplifier is highly saturated. At these conditions the losses due to absorption become comparable with the amplifier gain. Thus, in the contrast to the loss-less-amplifier, the optimal ratio between the pump and probe radiation intensities is appeared. These optimal conditions provide, on the one hand, the amplifier saturation, on the other hand, the gain high enough to compensate the absorption.

Next three figures illustrate the dynamics of the radiation and amplifier cell interaction with time. The vertical axis presents the radiation intensity and upper laser level population in relative units. The output pulses are shown by solid lines and the input pulses – by dashed lines (see graphs legends).

In Fig. 4.7 the interaction of the pump pulse with the amplifier cell is presented (the probe signal was absent). The pump pulse front saturates

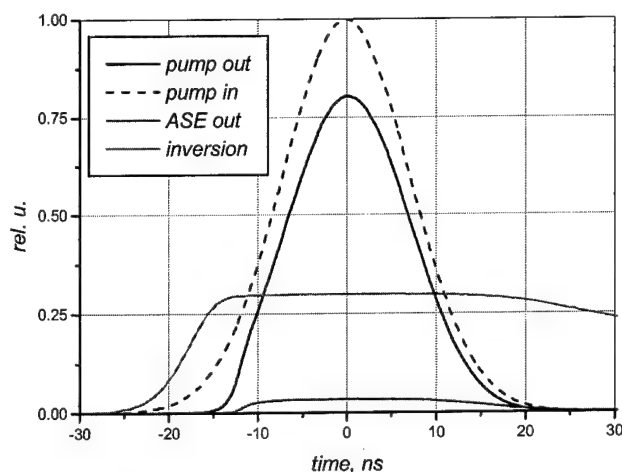


Fig. 4. 7

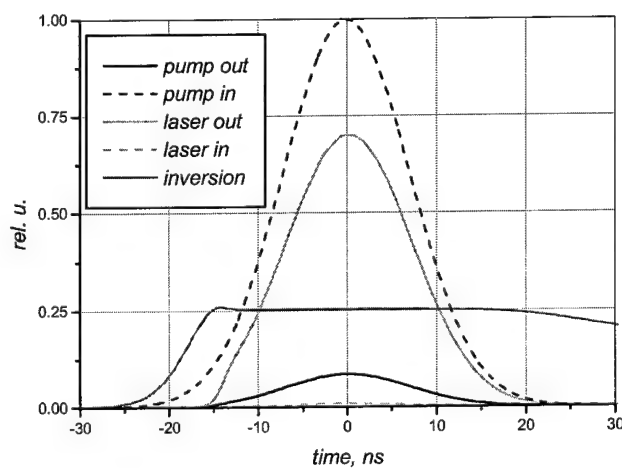


Fig. 4. 8

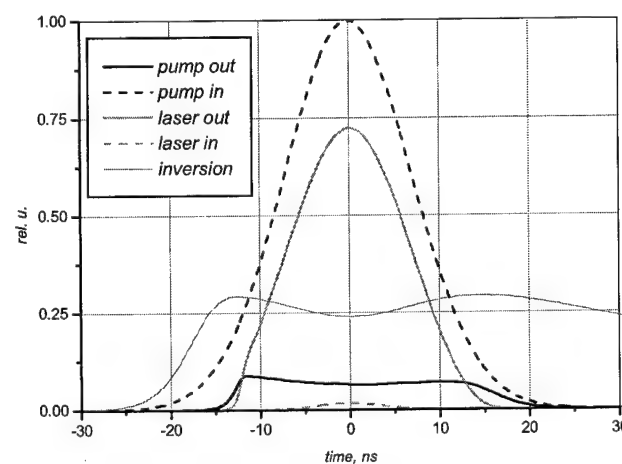


Fig. 4. 9

the active medium, then the pump pulse pass the active element without absorption. In the amplifier appears the ASE signal (red curve on a plot) but its intensity is enough low.

Fig. 4.8 shows how the amplifier works when the pump and probe pulse durations equal to each other and probe to pump energy ratio is 1/100. It is easy to see that the laser levels population and pulses temporal shape practically don't change while the radiation propagates through the amplifier. Therefore, for the amplifier analysis it is possible to use a stationary approximation.

Fig. 4.9 shows the results of the calculation when the probe pulse is two times shorter than the pump pulse and probe to pump energy ratio is 1/100. Under the conditions of pulses duration disagreement the amplifier works non-stationary and the pulses shape distortion takes place. Specifically, the output probe pulse duration tends to the pump pulse duration. It should be noticed, that in both cases even small probe signal suppresses completely the ASE pulse.

The presented numerical simulation results allow to make the following conclusions:

- ❖ The double pass color center laser amplifier scheme has an advantage over the single pass scheme since the saturation level of the double pass amplifier is approximately ten times smaller (see Fig. 4.4).
- ❖ The important feature of the $\text{LiF} : \text{F}_2^-$ color centers crystal is the minor influence of spontaneous effects. This allows to neglect the ASE process and to simplify the amplifier mathematical modeling.
- ❖ The disagreement between the pump and the probe pulse durations reduces the amplifier efficiency. However this reduction is not dramatic. For example, for the pulses with the Gaussian shapes and the probe pulse twice shorter than the pump pulse, the amplifier efficiency fall is only 10% (see Fig. 4.5).
- ❖ The parasitic losses in the active medium considerably reduce the amplifier efficiency. The absorption losses increase the saturation value of the amplifier. Therefore, for the active element with definite length and absorption there is an optimal pump energy which provides the maximum amplifier efficiency (see Fig. 4.6).

- ❖ Our calculations showed that the conformance of the pump and probe pulses temporal shapes allowed to use a stationary approximation for the amplifier numerical modeling.

The obtained numerical simulation results confirm the possibility of realization of the $LiF : F_2^-$ laser amplifier system with the gain value about 5 – 50. The important condition for the realization of such system is the good compatibility of the temporal and spatial parameters of the pump and probe radiation.

5. Development of LiF:F_2^- amplifier for tunable laser.

Development of narrow line high energy and high power color center laser requires the amplification of narrow line, short pulse laser beam from the master oscillator. This is the reason why master oscillator power amplifier scheme is investigated. The master oscillator provides the tunable radiation at the required wavelength and with narrow line width. As it was described in the previous chapter the efficiency of single frequency master oscillator could hardly be more than 5% and the output energy about $1 \div 5$ mJ. While higher output energy should be produced in the power amplifier based on color center crystals pumped either by conventional high energy $\text{Nd}^{3+}:\text{YAG}$ or $\text{Nd}^{3+}:\text{YLiF}_4$ laser system.

5.1. *The single-pass amplification in LiF:F_2^- color center crystal*

The amplification in LiF:F_2^- color center crystal was investigated in single-pass and two-pass optical schemes. The scheme of the first setup is presented in Fig. 5.1. The $\text{Nd}^{3+}:\text{YAG}$ laser with 100 mJ pulse energy and 3 Hz pps repetition rate was used as a pump source in our setup. The pump beam was split into two beams with 20 mJ and 80 mJ energies. The first one was used to pump the tunable LiF:F_2^- color center laser. It provided the probe beam for amplification experiments tunable from 1.08 to 1.27 μm with the pulse energy up to 2 mJ. The energy can be reduced by the set of neutral density filters. The experiments were proceeded mostly at 1.14 \div 1.17 μm wavelength that corresponded to the maximum power of the tunable radiation and maximum of the amplification.

The second part of the pump beam was used to pump the amplifier. Some delay between the pump and the probe beams was measured due to the temporal delay of the tunable radiation development and required beam paths inside and outside of the tunable laser unit. To compensate it the optical delay line with 140 cm length was required to synchronize the pump and the probe beams. As a result the pump and probe beams overlapped at the dichroic mirror (HR for probe beam and HT for pump) and then transmitted through LiF:F_2^- color center crystal investigated as an amplifier. After single-pass amplification the pump and the amplified beams were spectrally dispersed by the dichroic mirror and diffraction grating. The amplified radiation and the pump beam were measured simultaneously by photodiodes and digital oscilloscope Tektronix TDS-380. Due

to the fluctuation of the pump energy the intensity of the amplified beam changed from pulse to pulse.

The digital registration system allowed us to make the single pulse recordings that increased the accuracy of our measurements. The pump pulse duration was about 12 ns at 1064 nm wavelength, the duration of the probe pulse was shorter than $8 \div 10$ ns. The pulse shape was controlled by Ge avalanche photodiode and Tektronix TDS-380 digital oscilloscope with total temporal resolution of 0.5 ns. The good temporal overlapping of the pump and probe pulses was very important to get efficient amplification. The digital registration system allowed us to make the single pulse recordings that increased the accuracy of our measurements. The pump pulse duration was about 12 ns at 1064 nm wavelength, the duration of the probe pulse was shorter than $8 \div 10$ ns. The pulse shape was controlled by Ge avalanche photodiode and Tektronix TDS-380 digital oscilloscope with total temporal resolution of 0.5 ns. The good temporal overlapping of the pump and probe pulses was very important to get efficient amplification.

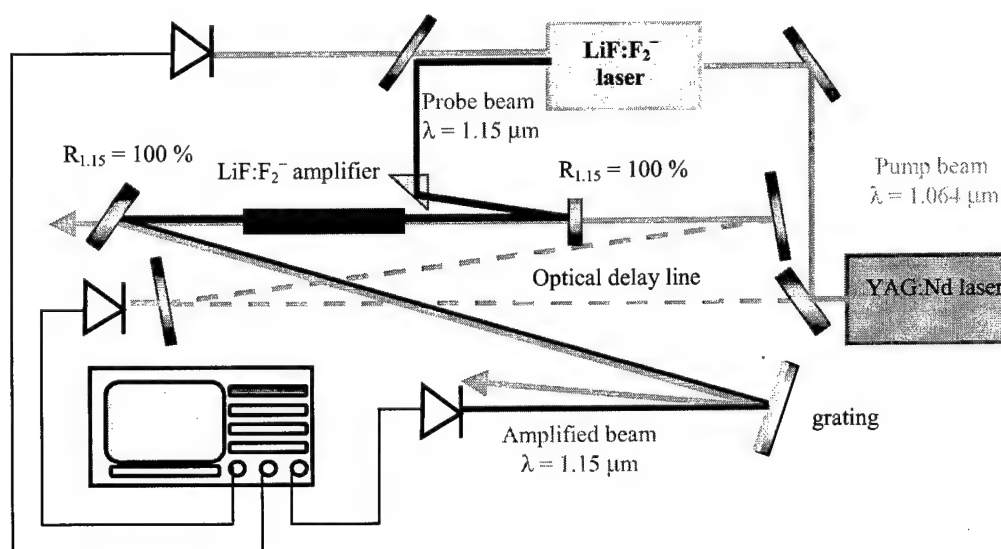


Fig. 5.1. Experimental setup for single pass amplification in LiF:F₂⁻ color center crystals

Table 5.1 presents the absorption coefficient (K_λ) of the radiation with different wavelengths. The value K_{1064} characterizes the initial transmission of the pump laser wavelength when pumped with Nd^{3+} :YAG laser. It is proportional to the concentration of F_2^- color centers in the LiF crystal. The value K_{965} presents the maximal absorption of F_2^- color centers in the LiF crystal if it is pumped in the maximum of their absorption spectra. The values $K_{1.15}$ and $K_{1.3}$ characterize active absorption and passive losses in lasing spectral range of LiF crystal. The value $K_{1.15}$ shows the sum of the parasitic losses and weak active absorption of F_2^- color centers. While $K_{1.3}$ reflects the value of only parasitic losses due the absorption by high aggregate and colloid centers. Our latest investigations of the color center crystal technology preparation showed that the efficiency of LiF:F_2^- color center laser strongly depends on the concentration of F_3^- color centers and higher aggregate centers, that have absorption at around 810 nm. Table 5.1 shows that the crystal 108 mm with higher absorption at 810 nm due to higher concentration of F_3^- color centers results in higher parasitic losses at 1300 nm wavelength also. The important parameter which characterize color center crystal is the value of the contrast which is the ratio of the $K_{1.064} / K_{1.3}$. It shows the correlation between the active and the passive losses and can be used as a figure of merit for this crystals. The best crystals should have high value of the active absorption coefficient and low passive losses.

Fig. 5.2-5.4 show the amplification dependence on the pump energy for three plane-parallel samples N1a, N2a and N3a, correspondingly. During the experiment pump and probe transmits simultaneously, that is there was no delay between the probe and pump pulses. One can see that the increase of the pump energy results in the increase of the

Table 5.1. Parameters of plane parallel LiF:F_2^- color center crystals and results of the single-pass amplification experiments with these crystals.

LiF:F ₂ ⁻ sample		Absorption, [cm ⁻¹]					Contrast K _{1.06} /K _{1.3}
№	length, [mm]	810 nm	965 nm	1064 nm	1150 nm	1300 nm	
N1a	108	1.59	1.24	0.32	0.045	0.017	19
N2a	95	1.26	1.2	0.33	0.029	0.01	~ 30
N3a	40			0.67	0.046	0.01	≥ 30

amplified beam energy as well as the amplification gain. The twice increase of the pump energy from 19 mJ to 37 mJ results in the 1.6 increase of the amplified beam for sample N3a.

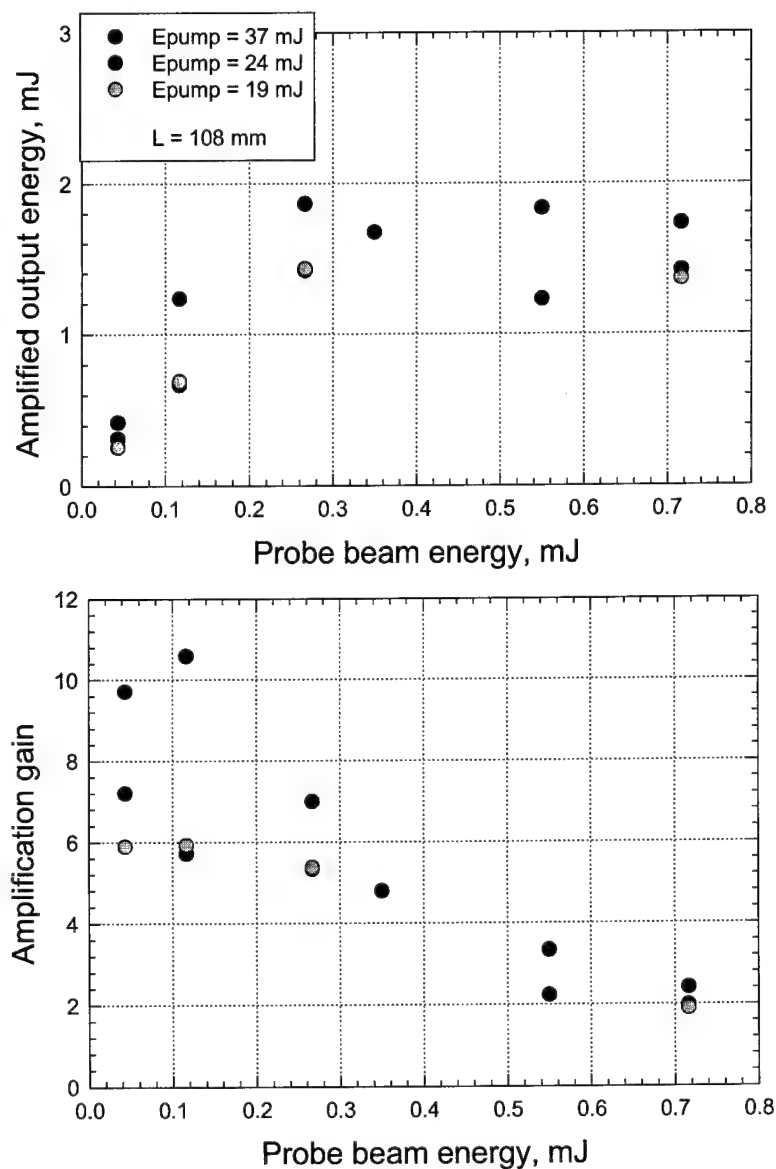


Fig. 5.2. The dependence of the amplification output and amplification gain on the probe beam energy for three pump energy values for sample N1a (108 mm long).

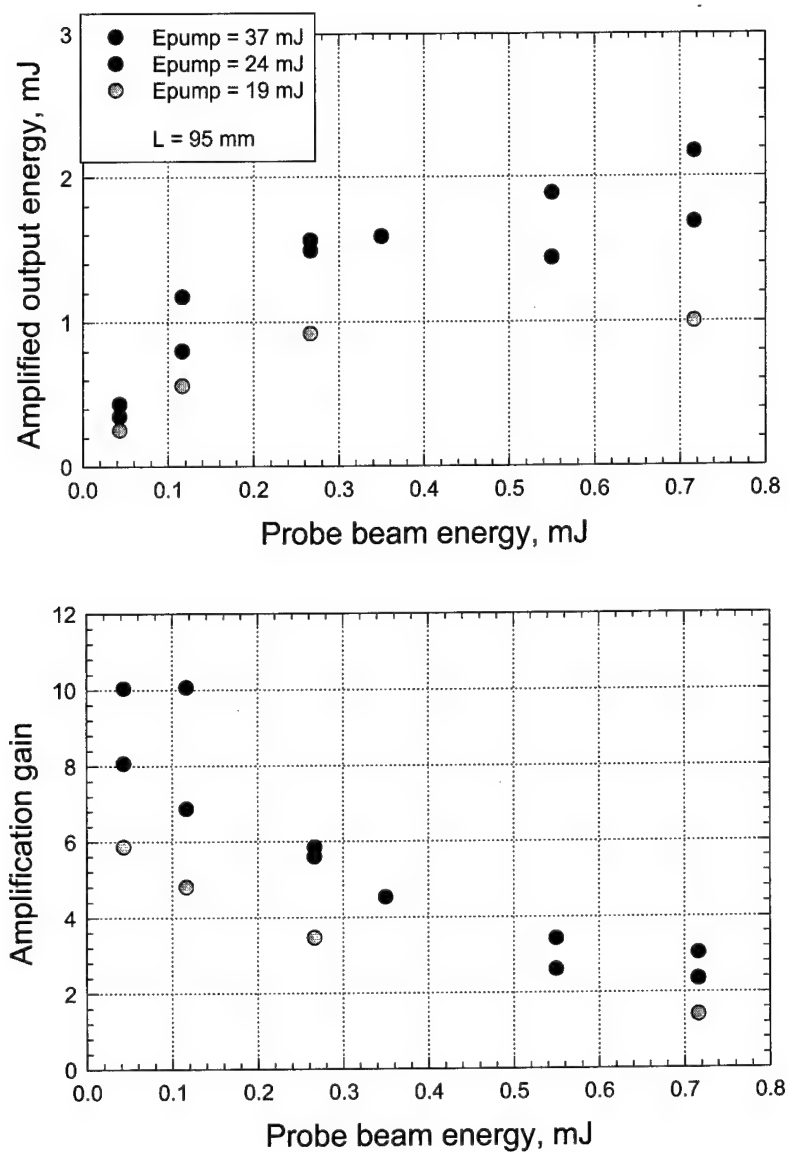


Fig. 5.3. The dependence of the amplification output and amplification gain on the probe beam energy for three pump energy values for sample N2a (95 mm long).

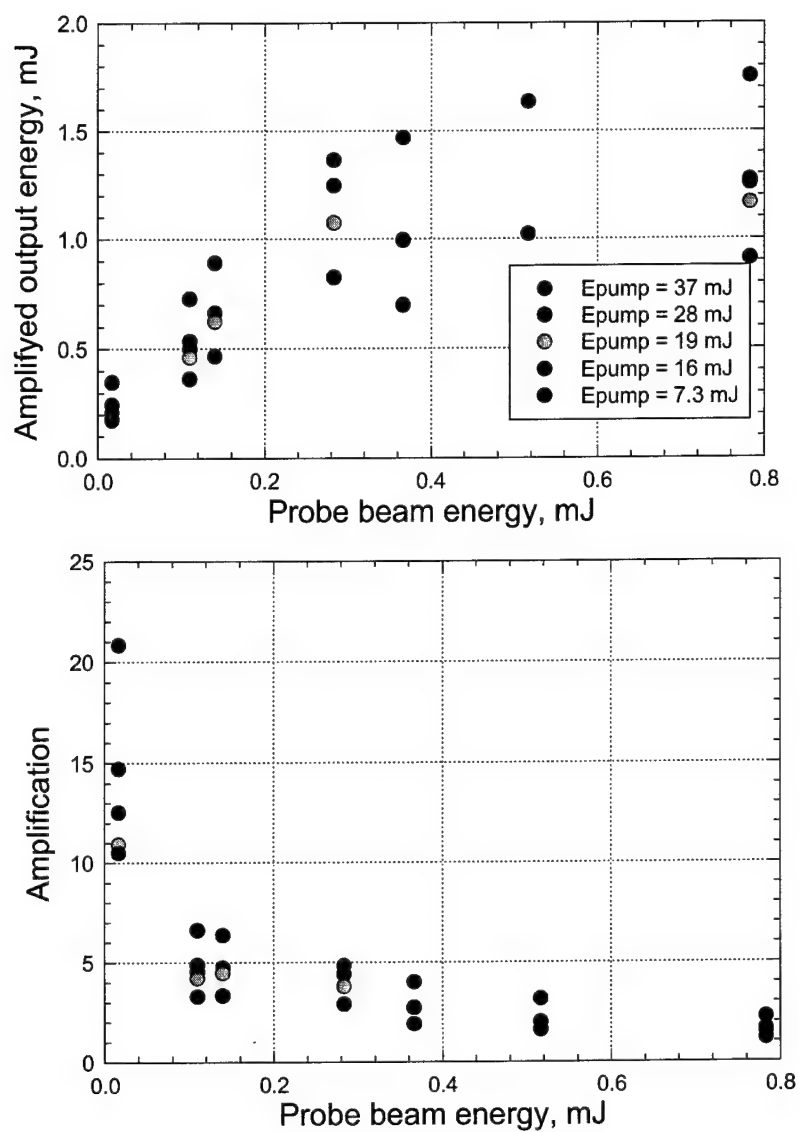


Fig. 5.4. The dependence of the amplification output and amplification gain on the probe beam energy for five pump energy values for sample N3a (40 mm long).

Fig. 5.5 shows the effect of amplified energy saturation and the amplification gain dependence in single-pass scheme with the increase of signal beam energy for these three samples without any delay between probe and pump beams. The pump energy was 37 mJ. There is no much difference between the results obtained in these samples. High amplification gain was observed at low probe energies ($G \sim 10 \div 20$) and it was strongly reduced for the high probe beam energies ($G \sim 2 \div 3$).

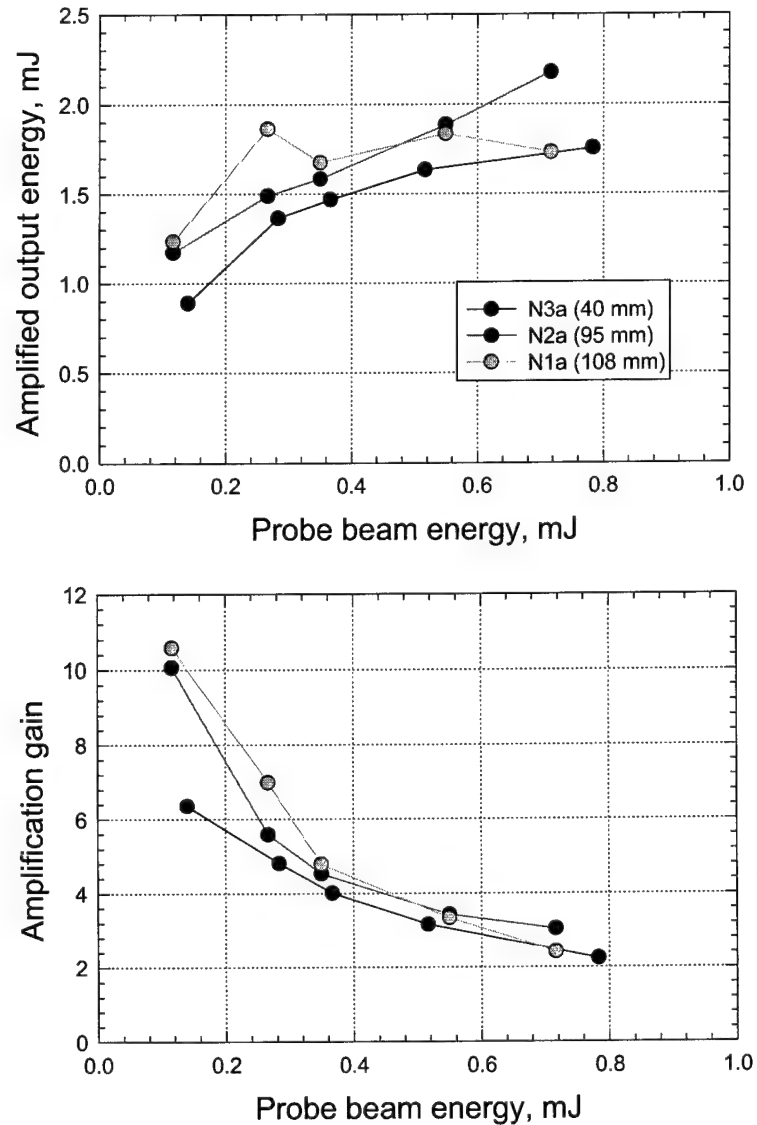


Fig. 5.5. The dependence of the amplification output and amplification gain on the probe beam energy for investigated samples without any delay between pump and probe pulses.

Similar experiments were made with these samples when the optical delay of 5 ns was introduced in the probe beam. The dependencies of the amplified beam energy and the gain G are shown in Fig. 5.6. The amplification gain for high probe energy was observed to be about $2 \div 3$. For this less effective temporal overlapping the length of the crystal that is the volume of the excited zone played an important role. So the highest values of amplification gain were obtained for the longest crystal.

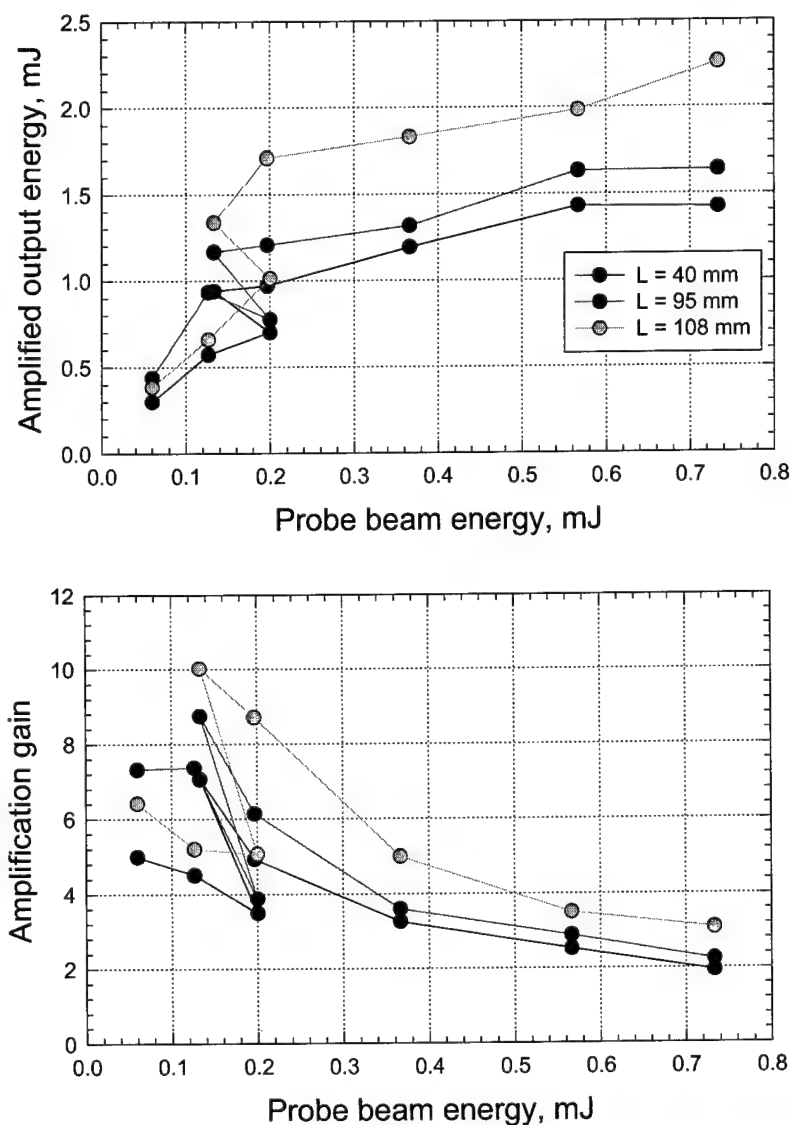


Fig. 5.6. The dependence of the amplification output and amplification gain on the probe beam energy for investigated samples with 5 ns delay between probe and pump pulses.

The best experimental results with pump pulse energy 40 mJ are presented in Fig. 5.7. It shows the effect of gain saturation and maximum output in single-pass scheme with different signal beam energy for these three samples. Table 5.2 summarizes the results on the amplification in three plane parallel samples (N1a-N3a) at the maximal pump pulse energy of 40 mJ. The results of two sets of the experiment are presented. The first one is the amplification of the lowest energy probe pulse ($E_{pr} = 0.06$ mJ) and the second is the highest energy probe pulse amplification ($E_{pr} \approx 1$ mJ). In the first set the highest values of the amplification gain in each crystal were obtained and reached values as high as $G = 9.5 \div 13$ but for low output energy $0.5 \div 0.9$ mJ. From the second set we got about 3 times less gain value ($G = 3.3 \div 4$), due to gain saturation effect but much higher output energy $3.3 \div 4$ mJ per pulse.

The highest values of low signal ($\alpha_0 = 0.563 \text{ cm}^{-1}$) and saturated gain coefficients ($\alpha_{sat} = 0.32 \text{ cm}^{-1}$) were observed in the short sample N3a (40 mm long crystal) which possessed the highest concentration of F_2^- color centers and the highest contrast and figure of merit. Among two other samples with similar absorption, optical density and length the best results were observed in the crystal N2a with higher contrast and lower passive losses. The highest overall small signal gain ($G=13$) we can find for the crystal N1a with the highest pump absorption optical density. Different situation was found for the saturated gain and output power where the highest optical density and contrast we found to be more important.

Table 5.2. Results on single-pass laser amplification experiments in plane-parallel LiF:F_2^- color center crystals.

LiF:F ₂ ⁻ sample			Amplification					
N _o	length [mm]	$D=K \cdot l$	Low probe ($E_{pr} = 0.06$ mJ)			High probe ($E_{pr} = 1$ mJ)		
			Gain, G	α_0 [cm ⁻¹]	Output energy, mJ	Gain, G	α_{sat} [cm ⁻¹]	Output energy, mJ
N1	108	3.46	13	0.237	0.7	3.3	0.111	3.3
N2	95	3.14	11	0.252	0.6	4.0	0.146	4.0
N3	40	2.68	9.5	0.563	0.5	3.6	0.320	3.6

The most interesting value is the highest possible output energy which could be obtained from the amplifier. Fig. 5.7 shows that the output energy as high as 4 mJ can be obtained with 40 mJ pump pulse that is almost 10% conversion efficiency.

As it was shown above the important factor for efficient amplification is good temporal overlapping of the pump and probe, signal pulses. The temporal delay was changed by varying the optical delay between the pump and the probe beams. Fig. 5.8 presents three temporal cases discussed above: synchronous ($\Delta t = 0$), delayed $\Delta t = 1.5$ ns and $\Delta t = 5$ ns delays between the pump and probe pulses. The pulse duration of LiF:F_2^- color center master oscillator was only slightly shorter than the pump pulse due to high amplification in color center active medium. The results on the single-pass amplification in LiF:F_2^- sample (N4) 90 mm long with Brewster cut windows for these three temporal cases are summarized in Fig. 5.8. One can see that the highest amplification was observed with small temporal delay $\Delta t = 1.5$ ns.

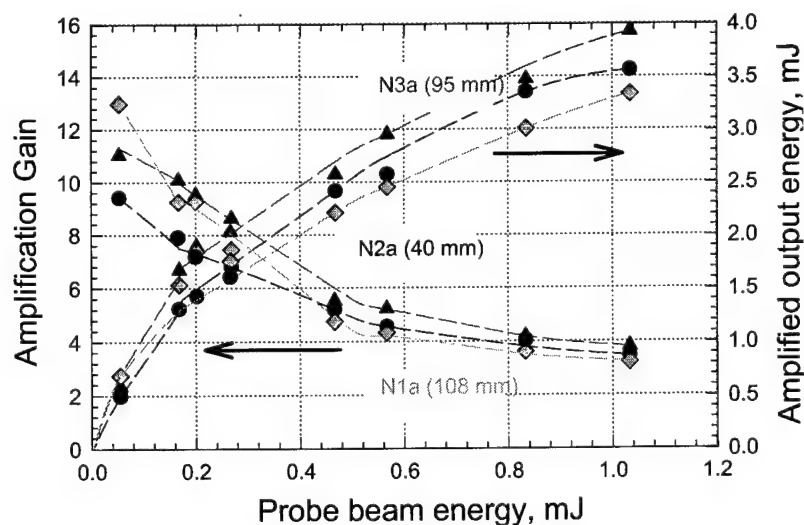


Fig. 5.7. Amplified energy and gain with respect to probe energy in single pass amplification scheme in for three LiF:F_2^- color center crystals.

This result can be explained by the fact that the beginning of the pump pulse is used for excitation of F_2^- color centers and absorption saturation in the active channel [Quant Elect. 1997]. The required time depends on the pump power density and the temporal shape of the front edge of the pulse. After this the active media is ready for efficient amplification and all probe pulse is used effectively for amplification. During the probe pulse passing through the gain channel, the F_2^- color centers stimulated emission and consequent pump absorption is observed again and again. If the probe pulse transmits too early ($\Delta t = 0$), its amplification is reduced due to low excitation of the medium at the beginning. If the probe pulse comes too late ($\Delta t = 5$ ns), the amplification is lower due to lowering of the pump power level and stationary gain. The proper delay between the pump and the probe pulses can result in high energy conversion efficiency that could be even higher than in $LiF:F_2^-$ oscillator due to low influence of the cavity and active medium passive losses.

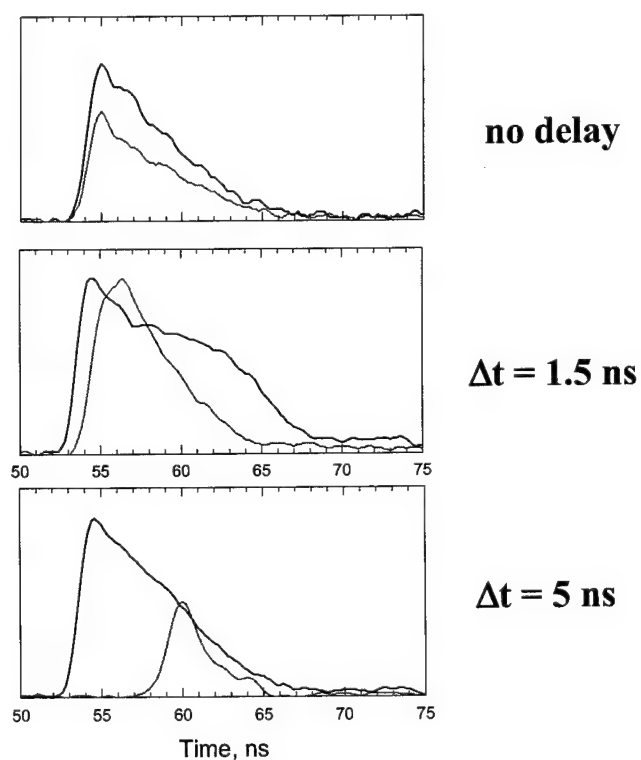


Fig. 5.8. Temporal evolution of the pump, $1.06 \mu m$ (black) and probe $1.15 \mu m$ (red) beams in the single-pass amplification experiments. The oscillograms were measured after the amplification cell.

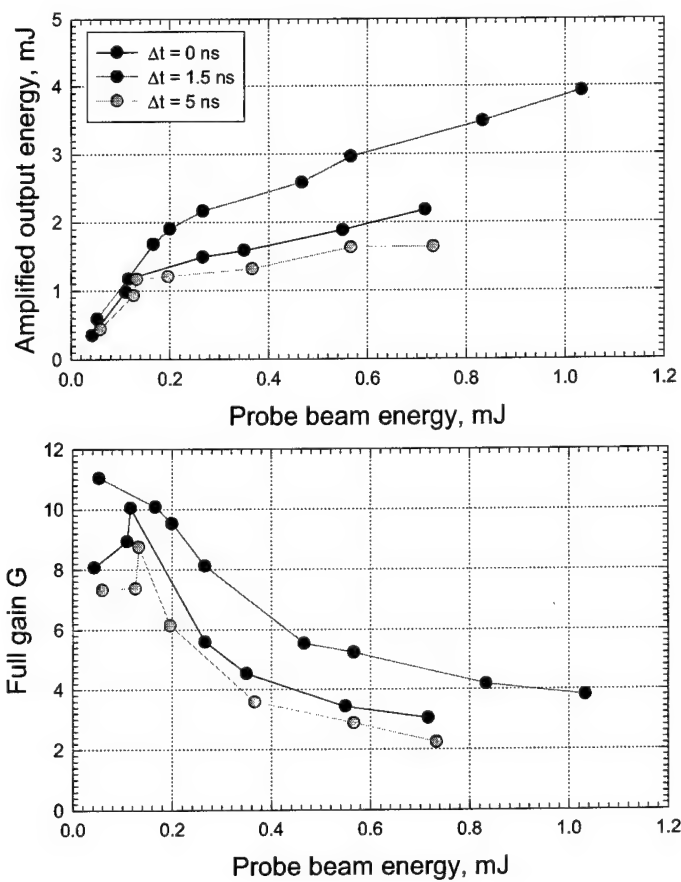


Fig. 5.9. Output energy and amplification gain versus probe beam energy for three temporal delays (0, 1.5, 5 ns) in single-pass amplification experiments.

The amplification in LiF:F_2^- color center crystal was also measured with respect to the operating wavelength. The maximum output on the oscillating wavelength of LiF:F_2^- laser was found to be at $1.14 \mu\text{m}$. Similar results were obtained for the case of amplification. Fig. 5.10 presents the results on the amplification in investigated sample for probe pulse with 1.12 , 1.15 and $1.18 \mu\text{m}$ operating wavelengths and 28 mJ pump pulse energy. One can see that for high probe energies the amplification for $1.15 \mu\text{m}$ wavelength is almost twice higher than for $1.12 \mu\text{m}$ and $1.18 \mu\text{m}$ wavelengths

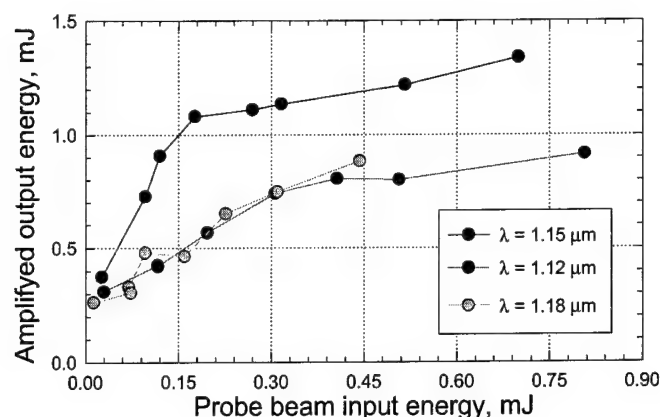


Fig. 5.10. Amplified output energy versus probe beam energy for three probe wavelengths 1.12, 1.15, 1.18 μm in single-pass amplification experiments.

5.2. Two-pass amplification in LiF:F_2^- color center crystal

The second experimental setup used in our amplification experiments was two-pass amplification scheme. Two passes increase the length of the amplifier medium that could result in the increase of the amplification gain. The optical scheme of experimental setup is shown in Fig. 5.11. The scheme was based on the same Nd^{3+} :YAG laser with 100 mJ pulse energy and 3 Hz pps repetition rate. The pump beam has one pass in the investigated sample while the probe beam has two passes. The beam intersection in the sample was at the angle of 2° that allows to have good spatial overlapping with some spatial separation. For spectral separation the dichroic mirror with high reflectivity at the probe beam wavelength and high transmission for pump beam was installed before the sample. The registration system was similar to that described in the previous section and allowed us measuring the amplification and the energy of the probe beam after the two passes. We used LiF:F_2^- sample with Brewster cut faces, N4a, 88 mm long. Fig. 5.12 shows the results on the amplified output energy and amplification gain for two pump energy values 23 and 28 mJ and three wavelengths of the probe beam 1.12, 1.15 and 1.18 μm . One can see that the maximum amplification values were obtained for the probe beam with 1.15 μm wavelength.

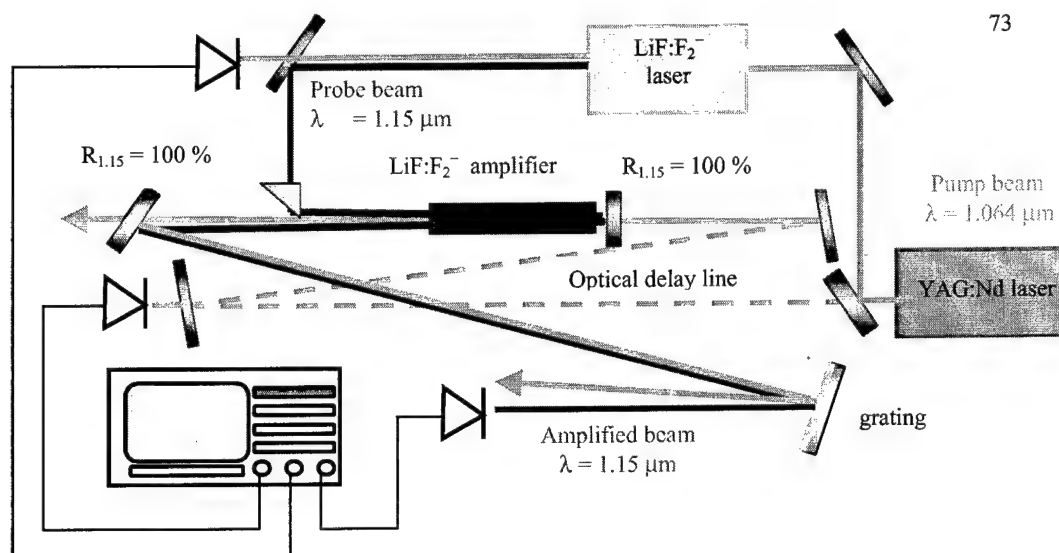


Fig. 5.11. Optical scheme of experimental setup for investigation two-pass amplification in LiF:F₂⁻ color center crystals with one-pass pumping.

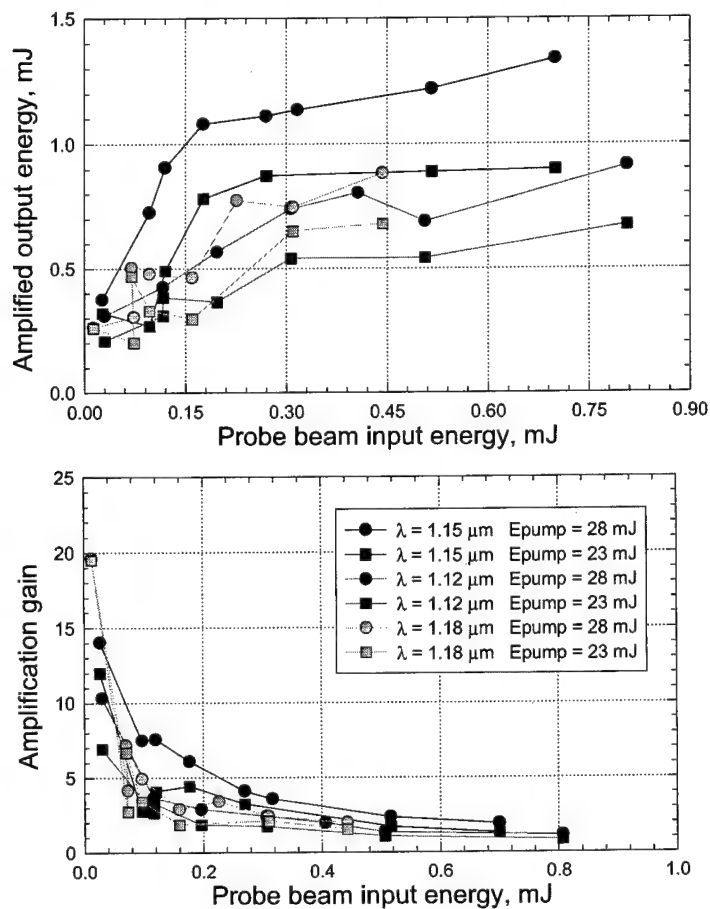


Fig. 5.12. Amplification in LiF:F₂⁻ color center crystal 88 mm long N4a with respect to the probe pulse energy for three probe wavelengths (1.12, 1.15 and 1.18 μm) and two pump energies 23 and 28 mJ in two-pass amplification and one-pass pumping scheme.

The amplified output energy and the amplification gain in this scheme reduced twice with respect to the single-pass scheme. This can be explained by the fact that the probe and pump beams had no good spatial overlapping. So the amplification region was reduced compared with single-pass scheme described above.

Another experimental setup which provides the highest amplification gain in our experiments includes two passes for both probe and pump beams. The optical scheme of experimental setup is shown in Fig. 5.13. The scheme used the same Nd^{3+} :YAG laser. The pump and probe beams passed through the sample at the angle about 1° for their spatial separation. The mirror with high reflectivity for both wavelengths was installed just behind the investigated sample to reflect the transmitted pump and amplified probe beams. The pump beam transmits in between the incident and the reflected probe beams.

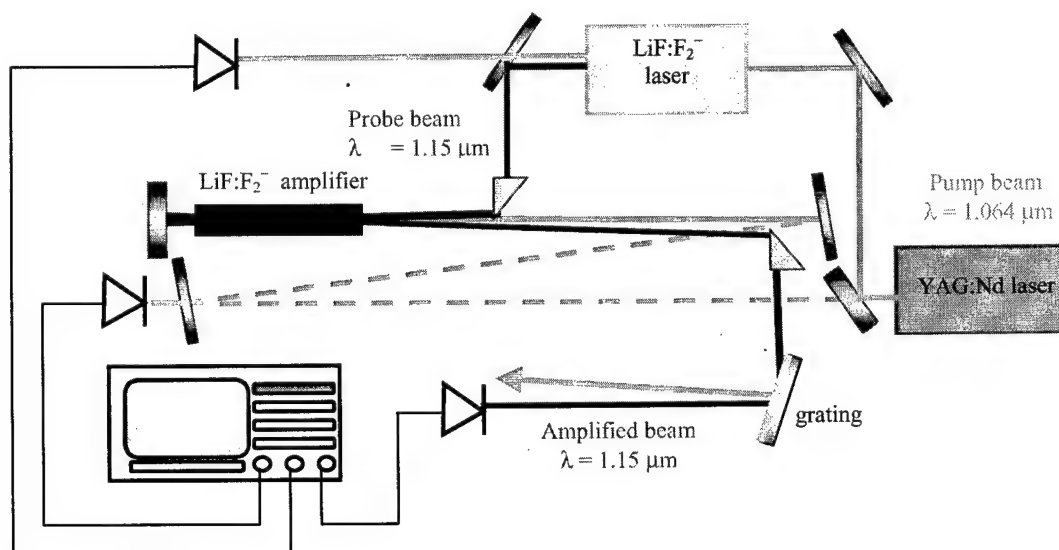


Fig. 5.13. Optical scheme of experimental setup for investigation two-pass amplification in LiF:F_2^- color center crystals with two-pass pumping.

As a result at 40 mJ pump pulse energy in the two-pass amplification cell small signal ($E_{pr} = 0.07$ mJ) was amplified to 4 mJ that corresponds to the gain as high as ~ 60 . For high energy probe beam ($E_{pr} = 2.2$ mJ) the amplification provided about 12 mJ output that gives the gain of ~ 6 (Fig. 5.14). These experiments were made with the same 88 mm long crystal with Brewster cut faces. The input pulse energy was increased up to 12 mJ that corresponds to 30% pump to amplified output energy conversion efficiency for double pass amplifier.

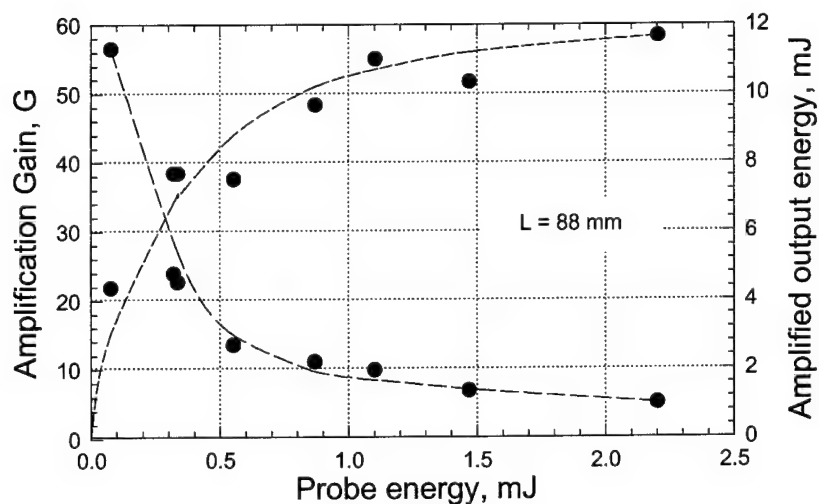


Fig. 5.14. Amplification gain and output energy of LiF:F_2^- two-pass amplifier with two-pass pumping.

The number of different LiF:F_2^- color center crystals with the same dimensions and Brewster cut faces were investigated in this double-pass amplification experiments. The samples has different concentration of active centers ($K_{1.064}$) and different passive losses. The results of the experiments and comparison with crystal parameters are presented in Fig. 5.15 and Table 5.3. The pump energy was 82 mJ. One can see that at high probe beam the amplification up to 19 mJ was obtained in the best LiF crystal (N2), which had the highest absorption ($K_{1.064}$) and rather low passive losses. The amplification output energy in other samples varied from 7 till 16 mJ for different types of crystals. The two-pass amplification gain at high probe energy was as high as 26 with 17 mJ output in the best crystal (N2) and decreased a little to 21 at the highest output 19 mJ due to gain saturation at $E_{pr}=0.9$ mJ. High quality of crystal (N2) was also proved by the highest output energy obtained for this crystal in the non-selective cavity.

Table 5.3. Active and passive characteristics of LiF:F_2^- color center crystals used in experiments on two-pass amplification: pump absorption at $1.064 \mu\text{m}$ ($K_{1.06}$) and parasitic absorption at $1.3 \mu\text{m}$ ($K_{1.3}$) measured spectroscopically and initial transmission $T_{0(\text{laser})}$ measured by Nd^{3+} :YAG laser at low power, amplification gain, and broadband laser oscillation in flat-flat Fabri-Perrot cavity.

Crystal N	$K_{1.06}$, [cm^{-1}] (spectr)	$K_{1.3}$, [cm^{-1}] (spectr)	Contrast β	Amplification output energy $E_{\text{pump}} = 82$ mJ $E_{\text{probe}} = 0.9$ mJ $E_{1.15}$ [mJ]	$T_{0(\text{laser})}$, [%]	$K_{(1.064)}$, (laser) [cm^{-1}]	Oscillation ($R_{OC} = 18\%$) $E_{\text{pump}} = 10$ mJ $E_{1.15}$ [mJ]
2	0.5	0.022	22.7	19	2.9	0.402	2.95
3	0.5	0.022	22.8	16.3	2.7	0.410	2.9
8	0.5	0.023	21.9	14.3	3.2	0.388	2.6
7	0.53	0.024	22.2	11.3	3.8	0.367	2.7
9	0.528	0.023	21.9	13	2.97	0.395	1.3
6	0.36	0.02	18.1	8	8.6	0.276	1.2
4	0.5	0.019	25.7	12.3	4.3	0.358	—
1	0.242	0.019	21.9	8.3	8.9	0.275	—
5	0.434	0.019	22.4	7	5.4	0.332	—

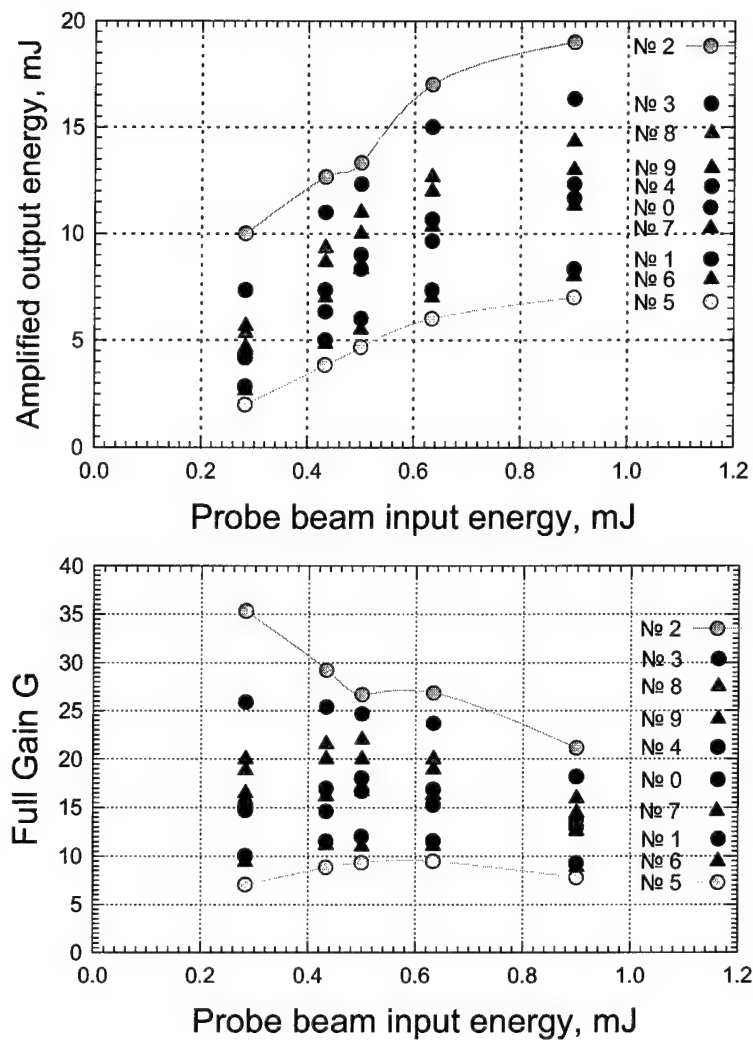


Fig. 5.15. Output energy of amplified probe beam and double-pass gain in different LiF:F_2^- color center crystals under 82 mJ pumping.

It was interesting for us to investigate the pump depletion during the amplification process. The temporal delay between the pump and the probe pulses were set to be 1.5 ns. We investigated the dependence of the pump depletion on the probe wavelength (Fig. 5.16). One can see that the pump depletion was very high for 1.15 and 1.18 μm wavelengths. In case of 1.15 μm wavelength the amplification efficiency was high due to high amplification coefficient.

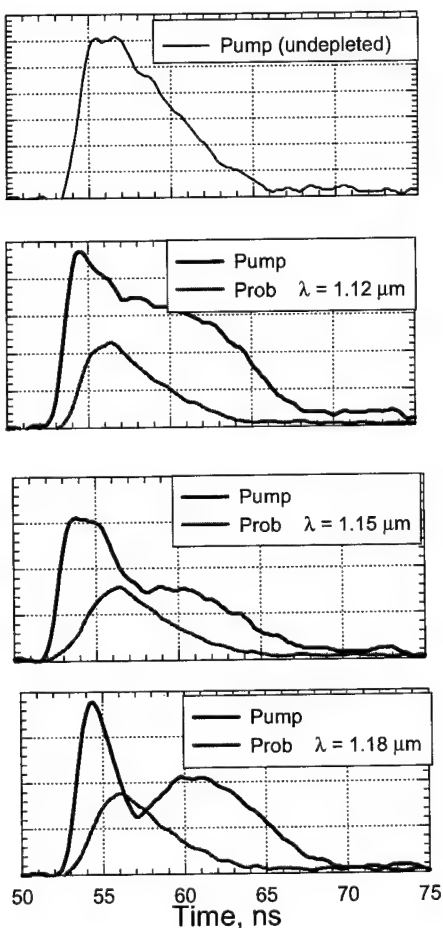


Fig. 5.16. Temporal oscillogramms of the pump and the amplified pulses in two-pass LiF:F_2^- color center amplifier.

The dependence of the amplification on the focusing conditions of the pump beam was investigated. The pump pulse energy was set to be 72 mJ. Fig. 5.17 presents the amplification of the probe beam for three cases without focusing (diameter of the pump pulse $\varnothing=3$ mm) - black points, after telescope collimator ($\varnothing=2$ mm) - red points and telescope broadening ($\varnothing=4$ mm) - green points. The collimation of the pump beam had to increase the saturation and conversion of the pump to the probe wavelength. At the same time this can reduce the intersection volume of the pump and probe beams. This is the possible reason that increase of the pump beam diameter reduced the pump intensity and the amplification gain but can improve the beams intersection. Fig. 5.17 shows that in our case the optimal configuration included no pump focusing in used experimental conditions that provided the maximal amplification ($G \sim 4$) and output to pump amplification efficiency up to 26%.

The length of the crystal is an important parameter in the amplification process. We checked this comparing the results on two-pass amplification in two crystals installed one after another (80 mm + 80 mm) with only one crystal (80 mm). The results of the experiment with the pump energy 57 mJ are presented in Fig. 5.18. The probe beam was focused by a lens with 50 cm focal length. One can see that the installation of the second LiF:F_2^- crystal allowed to increase the maximal amplified energy from 8 mJ for one crystal to 12 mJ for two crystals. Some amplification gain limitations can be due to complicity to provide good spatial overlapping of the pump and probe beams along long active medium (160 mm two crystals length) and can be further increase by special improvements.

Comparison of results presented in Figs. 5.14, 5.15 and 5.17 shows that in two-pass amplification with two-pass pumping scheme with the best LiF:F_2^- crystals (90 mm long) we can get amplifier conversion efficiency as high as 23-30% at variety of probe beam energies (0.6-5 mJ) and energy of pumping 40-80 mJ. So this quasi collinear two-pass amplification scheme shows 2-3 times better efficiency than collinear single-pass scheme (Fig. 5.7).

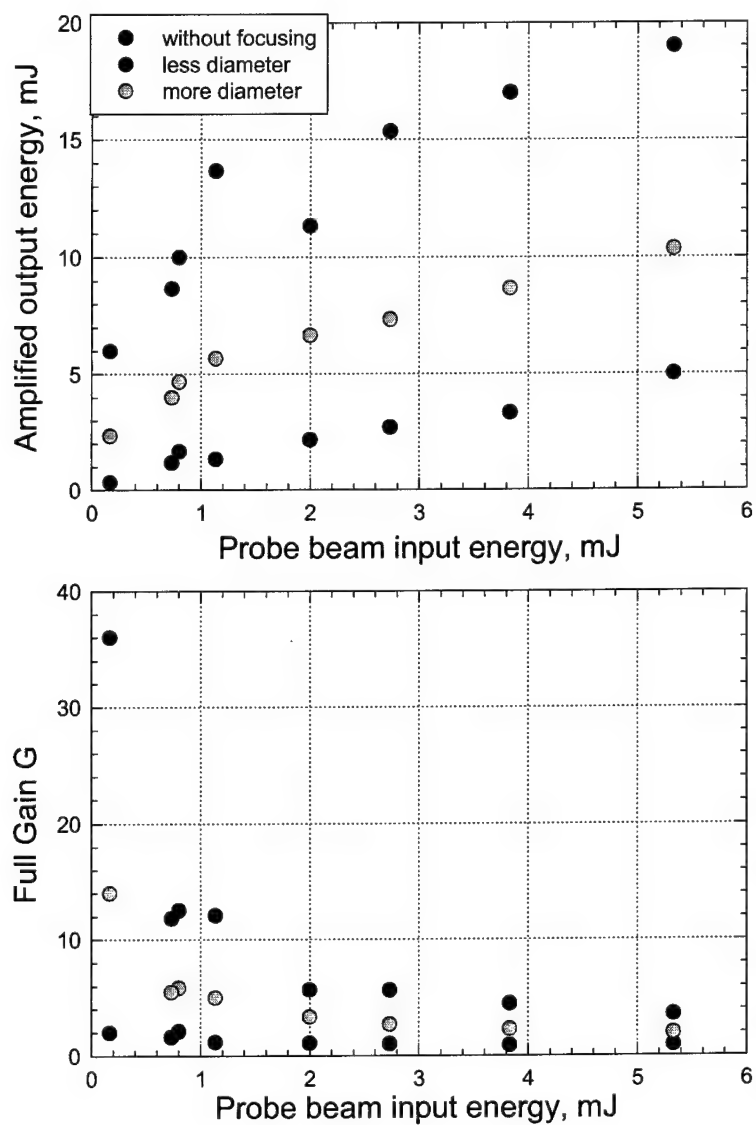


Fig. 5.17. Amplification in two-pass LiF:F₂⁻ color center amplifier for three pump beam collimating conditions: without collimating ($\varnothing=3$ mm) , with collimating ($\varnothing=2$ mm) and with broadening ($\varnothing=4$ mm) at $E_{\text{pump}}=72$ mJ.

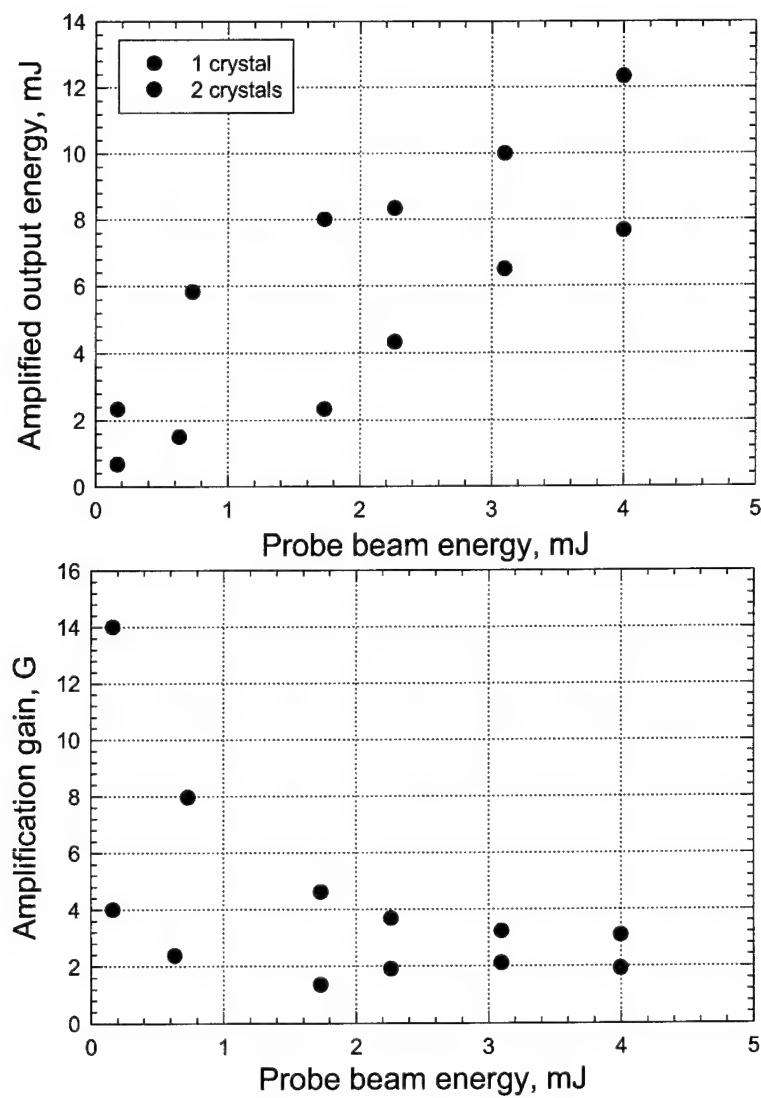


Fig. 5.18. Amplification in two-pass LiF:F_2^- color center amplifier consisting of one (black) and two (red) LiF:F_2^- color center crystal 80 mm long.

The main task of this project is to study high power narrow line color center laser system. In the further experiments we checked the dependence of amplification efficiency versus the spectral width of the probe beam. The probe beam has 3 cm^{-1} and 0.3 cm^{-1} spectral width. This was done by installing a special Fabri Perrot etalon into the color center laser. The installation of the etalon into the cavity added losses into the cavity that increased the build-up of the oscillation and reduced the output energy. It is necessary to control the temporal delay ($\Delta t = 1.5 \text{ ns}$) between the probe and pump pulses. Fig 5.20 presents the results on the amplification of the broadband and narrowband probe beams. One can see that amplification of 1 mJ probe beam was approximately the same in both cases. These results prove the quasi homogeneous feature of F_2^- color center gain profile in LiF crystals. Some difference can be due to different beam divergence and focusing conditions of color center laser with and without Fabri-Perrot etalon.

Four-pass amplifier was also tested. The experimental setup is shown in Fig. 5.21. After two-passes through the investigated sample the probe beam was reflected by additional mirror and has two more passes. The pump beam has only two passes. The temporal profile of the pump, probe and amplified pulses are shown in Fig. 5.22. The amplified output energy and amplification gain obtained in four-pass amplification experiments are shown in Fig. 5.23. During the first two passes the probe and pump pulses transmits simultaneously through the sample and provides effective amplification. During the third and fourth passes the probe beam is amplified in the tail of the pump pulse which has much lower intensity. So it has no much amplification, but even exhibit some energy losses due to parasitic absorption or amplified spontaneous emission. Due to geometrical limitations it was rather complicated to reduce the delay between the second and the third passes with this setup.

In conclusion we would like to outline that the saturated gain $G=3\div4$ can be obtained in single-pass scheme at regime close to the saturation with the amplifier output to pump efficiency about 10% which is far from the best results for color center laser. Two-pass amplifier with two-pass pumping scheme shows higher amplification gain $G=4\div20$ and much higher output to pump amplifier efficiency $20\div30\%$ that is quite close and competitive with the best color center laser results.

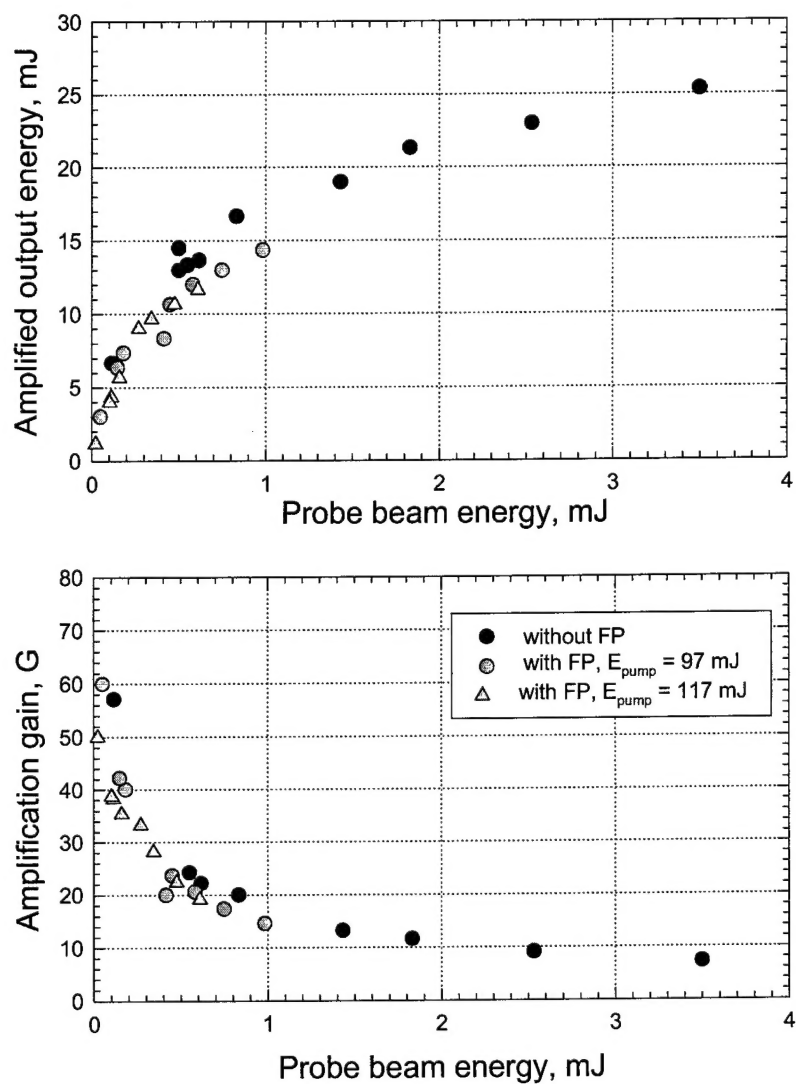


Fig. 5.19. Amplification of broadband (without FP etalon) and narrowline (with FP etalon) in two-pass color center amplifier.

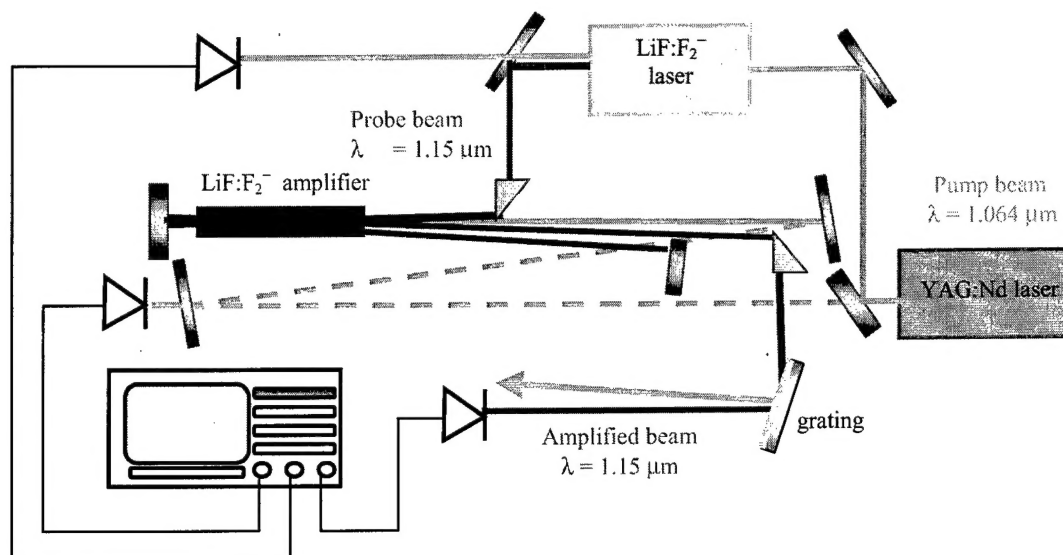


Fig. 5.20. Optical scheme of experimental setup for investigation of the amplification with four passes of the probe beam and two-pass pumping in LiF:F₂⁻ color center amplifier.

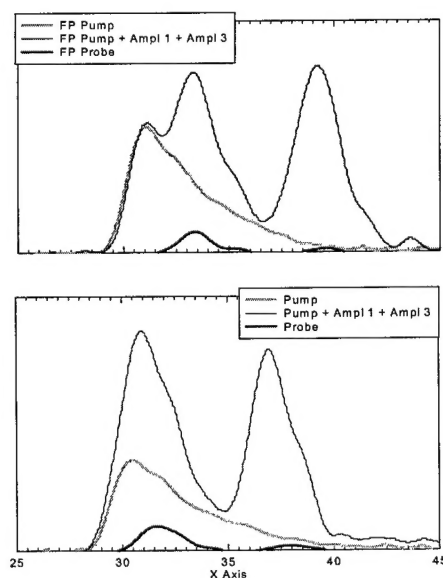


Fig. 5.21. Temporal oscillograms of the pump pulse (green), probe pulse (red) and pump plus probe pulses (blue) in four-pass amplifier.

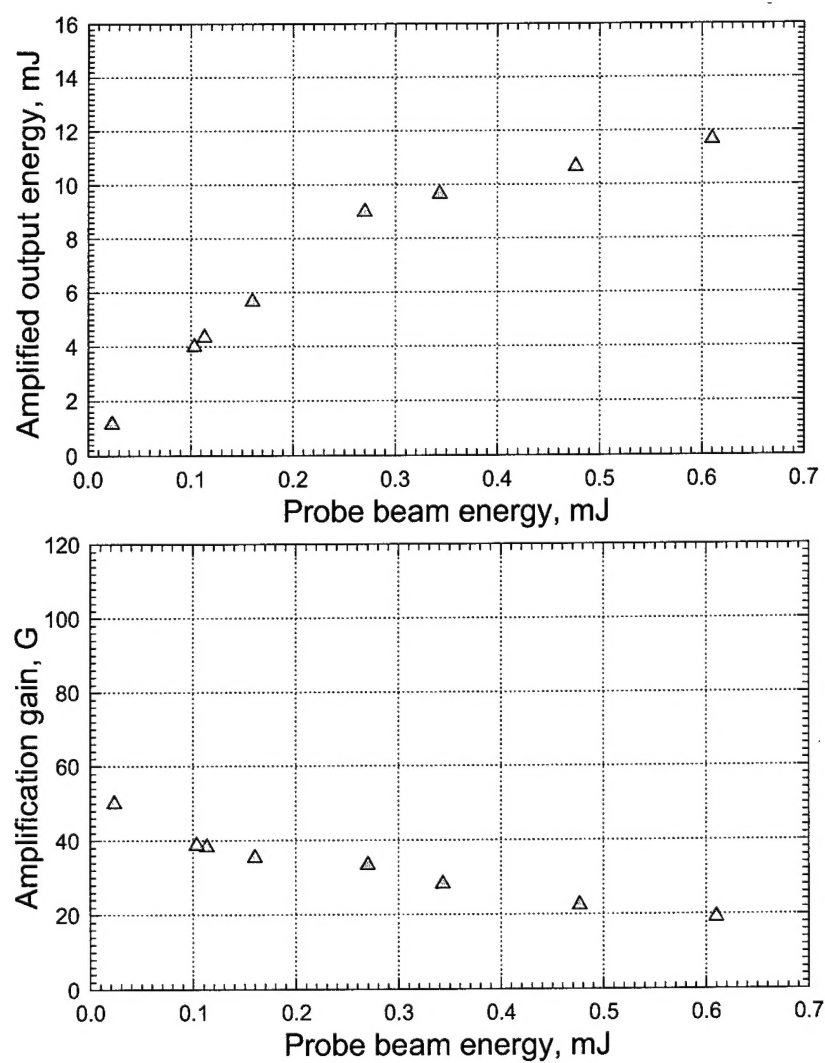


Fig. 23. Amplification output energy and amplification gain in four pass LiF:F_2^- color center amplifier with 117 mJ pump energy.